Aus der Klinik für Pädiatrie mit Schwerpunkt Neurologie

und dem Institut für Zell- und Neurobiologie

der Medizinischen Fakultät Charité – Universitätsmedizin Berlin

DISSERTATION

Identification and characterization of mechanisms underlying intellectual disability

zur Erlangung des akademischen Grades

Doctor of Philosophy (PhD)

im Rahmen des

International Graduate Program Medical Neurosciences

vorgelegt der Medizinischen Fakultät

Charité – Universitätsmedizin Berlin

von

Ethiraj Ravindran

aus: Chennai, Indien

Datum der Promotion: 02.03.2018

Table of contents

Figures and tables

Abstract

Intellectual disability (ID) has a high prevalence in individuals with neurodevelopmental disorders. Despite the high number of ID-associated genes, the genetic cause remains unclear in a considerable proportion of pedigrees and similarly the cellular and molecular mechanisms underlying the neurodevelopmental function of these genes remain poorly understood.

The main aims of my PhD project was to (i) identify 'novel' genes causing ID and characterize their pathophysiologic role in brain development, and (ii) characterize pathomechanism of known ID disorders and expand their clinical and cellular phenotype.

First, we approached the model disorder for congenital microcephaly and ID, autosomal recessive primary microcephaly (MCPH). MCPH is a clinically and genetically heterogeneous neurodevelopmental disorder with reduced brain volume at birth, ID, and lack of extracranial malformations. The hypothesis for MCPH-pathomechanism entails a premature shift from symmetric to asymmetric neuronal differentiation, resulting in progenitor pool depletion, thereby microcephaly and ID. Biallelic Cyclin-dependent kinase 5 regulatory-subunit associated protein 2 (*CDK5RAP2*) mutations cause MCPH3. Our data from *Cdk5rap2*-depleted murine embryonic stem cells revealed that in addition to premature neural differentiation, accumulating proliferating defect and increased apoptosis of differentiating- and early-postmitotic cells contribute to microcephaly. We reported for the first time the cellular phenotype of abnormal cell cycle apparatus (mitotic spindles, centrosomes), and lagging chromosomes in a MCPH2 patient with compound heterozygous WD-repeat domain 62 (*WDR62)* mutations. Reduced centrosomal CDK5RAP2 in MCPH2 patient's cells indicates converging functional role of MCPH genes.

Further, we identified a homozygous mutation in the previously not disease-linked gene Rho guanine nucleotide exchange factor 2 (*ARHGEF2*) in two patients with ID, congenital microcephaly, and mid-hindbrain malformation. We showed that the loss of ARHGEF2 causes abnormal mitotic spindles, spindle pole distance, impaired RhoA/ROCK/MLC pathway, and inhibits neurogenesis. We recapitulated the human brain phenotype in *Arhgef2*$^{-/-}$ mice and identified abnormal migration of precerebellar nuclei components as the underlying pathomechanism.

Further, we reported a biallelic mutation in zinc-finger and BTB-domain containing protein 24 (*ZBTB24*) in a patient with immunodeficiency-centromeric instability-facial anomalies syndrome 2 (ICF2) characterized by immunodeficiency, developmental delay, and facial anomalies. Initially, ICF2 was acknowledged as an isolated B-cell defect. We extended the phenotype spectrum by describing the development of combined immunodeficiency with age in ICF2 as well as putative autoimmune phenomena (hepatitis, nephritis). We showed that impaired proliferation, increased apoptosis, and abnormal mitotic spindles are likely contribute to immunological and non-immunological phenotype in ICF2.

With our studies, we demonstrated that abnormal proliferation, apoptosis, and/or migration due to defective cell cycle apparatus underlies as a common pathomechanism in ID and associated disorders.

Zusammenfassung

Eine Intelligenzminderung (ID) tritt mit einer hohen Prävalenz in Patienten mit einer neurologischen Entwicklungsstörung auf. Trotz der hohen Anzahl an ID-assoziierten Genen, bleibt die genetische Ursache sowie die zugrunde liegenden zellulären und molekularen Mechanismen in vielen Fällen noch unbekannt.

Die Hauptziele meiner Promotionsarbeit waren (i) neue Gene zu identifizieren, die zu ID führen und deren pathogene Rolle in der Gehirnentwicklung zu untersuchen und (ii) den Pathomechanismus bekannter Erkrankungen mit ID zu charakterisieren und den klinischen und zellulären Phänotyp zu erweitern.

In ersten Studien untersuchten wir die Modellerkrankung für angeborene Mikrozephalie und ID, die autosomal-rezessive primäre Mikrozephalie (MCPH). MCPH ist eine klinisch und genetisch heterogene Entwicklungsstörung des Gehirns, welche durch eine starke Verringerung des Hirnvolumens bei der Geburt, ID, sowie dem Fehlen von extrakraniellen Fehlbildungen gekennzeichnet ist. Die gegenwärtige Hypothese zur Entstehung von MCPH beschreibt eine frühzeitige Verschiebung der symmetrischen zu einer asymmetrischen neuronalen Proliferation, die zu einer Verringerung des Stammzellpools führt. Mutationen im Gen Cyclin-dependent kinase 5 regulatory-subunit associated protein 2 (*CDK5RAP2*) verursachen MCPH3. Unsere Experimente mit Cdk5rap2-herunterregulierten murinen embryonalen Stammzellen zeigten, dass neben einer vorzeitigen neuronalen Differenzierung, ebenfalls ein Proliferationsdefekt und eine erhöhte Apoptoserate von frühen postmitotischen Zellen zur Mikrozephalie beitragen. Zudem zeigt diese Studie zum ersten Mal Veränderungen im Aufbau des Zellzyklusapparates (Mitosespindel, Zentrosom) und der Chromosomenkondensierung in einem Patienten mit einer compound heterozygoten Mutation im WD-repeat domain 62 Gen (*WDR62)*.

In einer weiteren Studie wurde eine homozygote Mutation im bisher nicht krankheitsassoziierten Gen Rho guanine nucleotide exchange factor 2 (*ARHGEF2*) in zwei Patienten mit ID, kongenitaler Mikrozephalie und einer Fehlbildung des Mittel- und Hinterhirns untersucht. Wir konnten in funktionalen Studien zeigen, dass der Verlust von *ARHGEF2* zu Veränderungen in Mitosespindeln und dem Spindelpolabstand sowie einer Beeinträchtigung des RhoA/ROCK/MLC-Signalweges führt, welches zur Hemmung der Neurogenese beiträgt. Der humane Phänotyp konnte in *Arhgef2*-

knockout Mäusen rekapituliert werden und zeigte zudem eine gestörte Migration von präzerebellaren Zellen.

Weiterhin berichten wir über eine biallelische Mutation im zinc-finger and BTB-domain containing protein 24 (*ZBTB24*) in einem Patienten mit immunodeficiency-centromeric instability-facial anomalies syndrome 2 (ICF2), charakterisiert durch Immunschwäche, Entwicklungsverzögerung und Gesichtsanomalien. Bislang wurde ICF2 primär als isolierter B-Zelldefekt anerkannt. Wir erweiterten das Phänotypspektrum, indem wir zum ersten Mal die Entwicklung einer kombinierten Immunschwäche und eines vermutlichen Autoimmunphänomens (Hepatitis, Nephritis) beschrieben. Weiterhin konnten wir nachweisen, dass Veränderungen in der Zellproliferation, Apoptoserate und Veränderung in der Chromosomentrennung zu dem beschriebenen immunologischen und nicht-immunologischen Phänotyp in ICF2 beitragen.

Mit unseren Studien konnten wir nachweisen, dass eine abnormale Proliferation, Apoptose und / oder Migration aufgrund eines defekten Zellzyklusapparates als gemeinsamer Pathomechanismus bei ID und assoziierten Störungen zugrunde liegt.

Introduction

1.1 Microcephaly

Microcephaly is clinical sign defined as a significant reduction in the occipito-frontal head circumference of at least two standard deviations (SD) below the ethnically matched age- and sex-related mean. Microcephaly can be caused genetically or through environmental factors and is divided into two types: primary (congenital) microcephaly already present at birth and secondary (postnatal) microcephaly. About 2% of the general population are microcephalic, and the incidence of primary microcephaly is 1:30,000-1:250,000 live-births.(1-3) Microcephaly represents a high risk factor for developmental delay including intellectual disability (ID).

1.2 Intellectual disability (ID)

ID is characterized by significant limitations in intellectual function and adaptive behavior, and has a prevalence of 2-3% in the general population.(4) Based on its severity measured with the intelligent quotient (IQ), ID is classified into mild (IQ 50-70), moderate (IQ 35-49), and severe (IQ<34) forms.(5) Similar to microcephaly, ID can be caused by various environmental and/or genetic factors; however, in about 60% of the cases the cause remains unknown.(6) Clinically, ID is categorized into two types: syndromic and non-syndromic. In syndromic ID, patients are usually accompanied with one or more clinical features such as facial dysmorphism, whereas in non-syndromic ID, ID is the only clinical phenotype. ID can be associated with radiologically identifiable developmental disorders of the brain such as corpus callosum agenesis, gyration defects, and cerebellar hypoplasia. Thus, proper structural development of the nervous system is highly important for the cognitive function.(6)

1.3 Central nervous system development

Human brain development begins around the 3rd week of gestation with proliferation, and differentiation of neural precursor cells.(7,8) Various environmental and genetic factors contribute to pre- and post-natal developmental processes, i.e., neurogenesis, migration, dorso-ventral patterning, synaptogenesis, myelination, and apoptosis. Disturbances in the fine-tuned process of nervous system development can result in malformations and functional disabilities (Figure 1).(9)

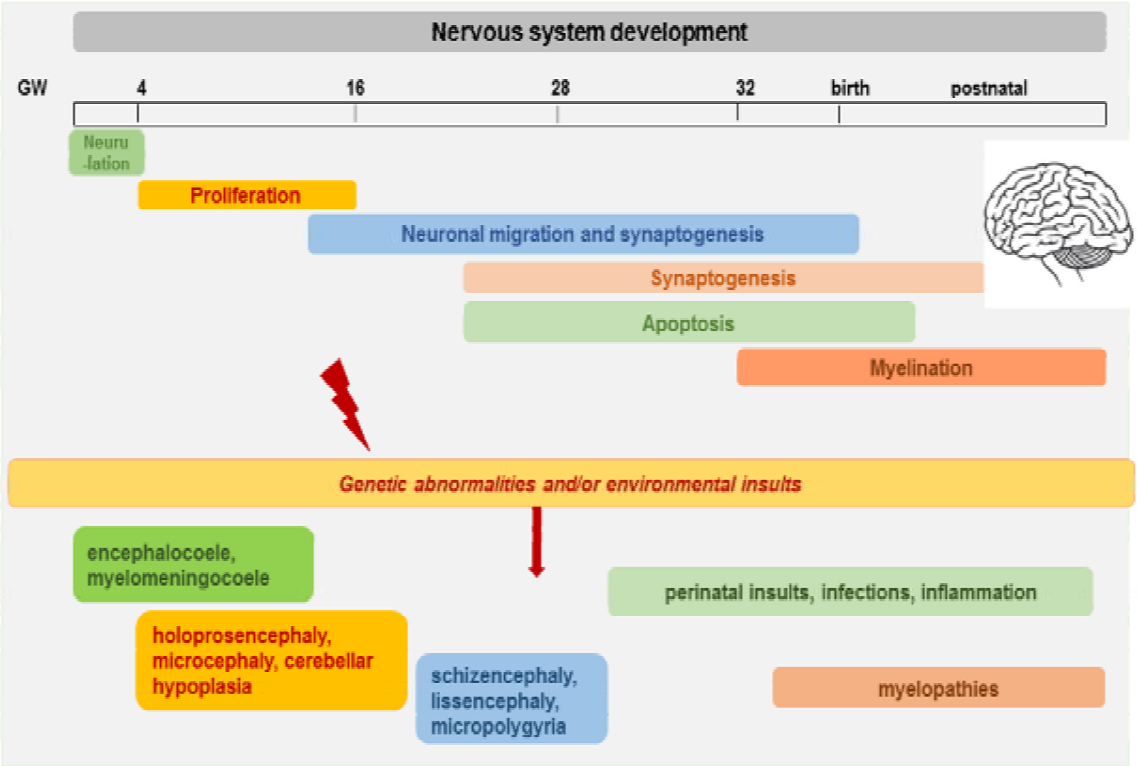

Figure 1. Nervous system development and related neurodevelopmental disorders. Processes during brain development (proliferation, migration, synaptogenesis, and myelination) are timely controlled through a multitude of genetic and environmental factors. Perturbations in these process leads to specific disorders (figure adapted and modified from (8)).

An array of spatially and temporally regulated genes lead the process of nervous system development through exertion of range of cellular functions. More than 800 genes have been linked to ID, most of which are key to nervous system development.(10) In the following, I will briefly introduce different types of ID associated with or not associated with brain malformation and microcephaly that are relevant to my thesis.

1.4 Non-syndromic ID with microcephaly

Autosomal recessive primary microcephaly (MCPH, Microcephaly Primary Hereditary) is a clinically and genetically heterogeneous rare disorder characterized by microcephaly at birth and ID. More than 300 families with MCPH have been identified with mutations in 17 different genes world-wide (see Table 1). (11-13) These 17 microcephaly genes have been reported to control brain size and function by regulating cell cycle, chromosome condensation, spindle formation, centrosome function, and apoptosis.(1,3)

MCPH models signify that the loss of MCPH-related proteins favors premature transition from symmetric to asymmetric neuronal differentiation through a shift of the cleavage plane, leading to depletion of the precursor pool and reduction of the number of neurons, ultimately causing microcephaly. (reviewed in (14) Two of the well-studied MCPH subtypes, MCPH2 and MCPH3, which were also subject of research work presented in this dissertation will be discussed in detail in the following.

Table 1. Types of MCPH and its causative genes

MCPH	Protein	Gene	OMIM
MCPH1	Microcephalin	MCPH1	251200
MCPH2	WD repeat-containing protein 62	WDR62	604317
MCPH3	CDK5 regulatory subunit-associated protein 2	CDK5RAP2	604804
MCPH4	Cancer susceptibility candidate 5	CASC5	604321
MCPH5	Abnormal spindle-like, microcephaly associated	ASPM	608716
MCPH6	Centromeric protein J	CENPJ	608393
MCPH7	SCL/TAL1 interrupting locus	STIL	612703
MCPH8	Centrosomal protein 135kDa	CEP135	614673
MCPH9	Centrosomal protein 152kDa	CEP152	614852
MCPH10	Zinc finger protein 335	ZNF335	615095
MCPH11	Polyhomeotic-like protein 1	PHC1	615414
MCPH12	Cyclin-dependant kinase 6	CDK6	616080
MCPH13	Centromeric protein A	CENPE	616051
MCPH14	C. elegans homolog of SAS6	SASS6	616402
MCPH15	Major facilitator superfamily domain-containing protein 2A	MFSD2A	616486
MCPH16	Ankyrin repeat- and LEM domain-containing protein 2	ANKLE2	616681
MCPH17	Citron kinase	CIT	617090

Biallelelic mutations in the WD repeat domain 62 gene (*WDR62)*, located on chromosome 19q13.12, cause the second most common MCPH subtype, MCPH2 (MIM*613583).(15) WDR62 contains 1523 aa with 15 WD or beta-transducin repeats.(16) While most patients with MCPH have no gross brain malformation, this certainly does not hold true for MCPH2. Patients with MCPH2 can display severe brain malformations including pachygyria, lissencephaly, schizencephaly, and corpus callosum hypoplasia. In mice, *Wdr62* is expressed in neural progenitors in the

ventricular/subventricular zone. siRNA knockdown of *Wdr62* induces early cell cycle exit, reduced cell proliferation, spindle orientation defects and decreased centrosomal integrity.(17,18) However, the effect of WDR62 dysfunction has not been studied in humans.

A more rare MCPH subtype, MCPH3, is caused by biallelic mutations in the Cyclin-dependent kinase 5 regulatory-subunit associated protein 2 gene *CDK5RAP2* (MIM*604804).(19) CDK5RAP2 is a centrosome-associated protein composed of 1893 aa, required for processes such as centrosome function, spindle checkpoint regulation and orientation. *Cdk5rap2* mutant mice have small brains with abnormal orientation and morphology of mitotic spindles in neural progenitors, premature neuronal differentiation, reduced proliferation, and early cell cycle exit.(20-22) Despite the ubiquitous expression of CDK5RAP2, the neural-specific phenotype of MCPH3 needs to be addressed.

1.5 Syndromic ID with microcephaly

Mid-hindbrain malformations can occur during embryogenesis through a disturbance of transient and localized gene expression patterns within these distinct brain structures.(23,24) One group of such proteins known to contribute to localized gene expression is Rho guanine nucleotide exchange factor (ARHGEF) family members, which play key role in regulation of cytoskeleton dynamics, cell division, and cell migration.(25) In the dissertation work a novel mid-hindbrain defect associated with mild microcephaly and ID caused by a homozygous mutation in the Rho guanine nucleotide exchange factor 2 (*ARHGEF2)* gene will be presented. ARHGEF2 catalyzes the exchange of GDP to GTP on Rho-related proteins and thereby controls the spatial and temporal activation of various Rho GTPases such a RhoA. ARHGEF2 is required for microtubule organization, spindle formation and orientation, neurogenesis, and neural tube closure.(26-30) Mutations in other *ARHGEF* family members have been reported to cause non-syndromic intellectual disability (*ARHGEF6*), epileptic encephalopathy (*ARHGEF9*), and peripheral demyelinating neuropathy (*ARHGEF10*).(31-33) However, ARHGEF2 has not been previously linked to human disease and further studies on underlying pathomechanism are crucial.

1.6 Syndromic ID without microcephaly

Disturbances in gene products for epigenetic functions such as DNA methylation, histone modifications, and chromatin remodeling can lead to ID.(34,35) Several of these epigenetic regulators play a key role in neural development by controlling the expression of various genes. For example, DNA methyltransferase 3 (DNMT3) is an epigenetic regulator controlling development through DNA methylation.(36) Loss of function mutations in *DNMT3B* cause the ID syndrome and immunodeficiency-centromeric instability-facial anomalies (ICF) syndrome. ICF is characterized by immunodeficiency, intellectual deficit, and facial dysmorphism, and based on the genetic causes, ICF is classified as ICF1, ICF2, ICF3, ICF4, and ICFX. Mutations in *DNMT3B*, the zinc-finger- and BTB-domain containing 24 gene (*ZBTB24)*, cell division cycle associated 7 (CDCA7), and helicase, lymphoid-specific (HELLS/LSH) causes ICF1, ICF2, ICF3, and ICF4, respectively.(36-38) The ICF syndrome is considered mainly as a B-cell disease secondary to the defects in the hematologic development and immunodeficiency. However, this does not explain the non-immunological phenotype of ICF patients and further studies on the putative mechanism are mandatory for therapeutic strategies.

2 Aims

A multitude of genetic causes and phenotypes of neurodevelopmental disorders, particularly ID and MCPH, have been reported; however due to its clinical heterogeneity, these disorders remain to be discerned for better diagnosis. Also, molecular mechanisms underlying the disease phenotype needs further elucidation for future therapeutical approaches. The main goal of my PhD project was to identify and characterize mechanisms leading to intellectual disability. Specifically, I aimed at the

1. identification and characterization of ‘novel’ genes causing ID and their pathophysiologic role in nervous system development.
2. identification and characterization of pathomechanism of known rare ID disorders and expansion of their clinical and cellular phenotype.

3 Materials and methods

3.1 Patients

Informed consent was obtained from parents of patients for molecular genetic analysis, publication of clinical data, radiological imaging data, and studies on lymphoblastoid cell lines (LCLs) as well as primary fibroblasts. DNA was extracted from EDTA blood samples using Illustra BACC2 DNA extraction kit (GE Healthcare, Freiburg, Germany). Our studies were approved by the local ethic committee of the Charité (approval no. EA1/212/08 and EA2/163/12).

3.2 Epstein-Barr virus-transformed lymphocyte and fibroblast culture

LCLs were established according to the protocol published by Neitzel et al. 1986.(56) Non-adherent LCLs were cultured in RPMI 1640 with L-Glutamine (Invitrogen, Darmstadt, Germany) supplemented with 20% v/v fetal bovine serum (Biochrom, Berlin, Germany) and 1% v/v penicillin-streptomycin (Sigma-Aldrich, Taufkirchen, Germany). Fibroblasts culture were established according to a standard protocol and cultured in DMEM with 4.5 g/l D-glucose and pyruvate (Invitrogen, Darmstadt, Germany) supplemented with 15% fetal bovine serum and 1% penicillin-streptomycin.

3.3 Genetic analysis

For whole exome sequencing (WES), genomic DNA was isolated from blood samples using standard methods. Five micrograms of genomic DNA were enriched using the Agilent Human All Exon V3 kit (Agilent Technologies, Santa Clara, CA, USA) following the manufacturer's protocol. Whole-exome libraries were sequenced on an Illumina HiSeq 2000 system for 1x101 cycles following the manufacturer's instructions (Illumina), and the identified mutation was confirmed by Sanger sequencing.

3.4 RNA extraction and quantitative real time-polymerase chain reaction (qRT-PCR).

Total RNA extraction was performed using the TRizol reagent (Sigma-Aldrich, Taufkirchen, Germany). cDNA was synthesized using the ThermoScriptR RT-PCR System (Invitrogen, Karlsruhe, Germany), with a combination of oligo(dT)20 and random hexamer primers. Primers were designed using the Primer3 online software (www.primer3.ut.ee). Quantitative PCR experiments were performed using Maxima

SYBR Green/ROX qPCR Master Mix (Thermo Scientific, Braunschweig, Germany) according to the manufacturer's protocol and analyzed using the –ddCT method.

3.5 Protein extraction and Western blot

Protein from cell pellets was isolated by homogenization in radioimmunoprecipitation assay (RIPA) buffer containing 1 mM phenylmethylsulfonyl fluoride (PMSF; Sigma-Aldrich, Taufkirchen, Germany) and 1 protease inhibitor cocktail tablet per 10 ml RIPA buffer (Complete Mini; Roche Diagnostics, Mannheim, Germany), with 15 min incubation on ice, successive ultrasonication for 10 sec and centrifugation for 20 min at 16,000 g and 4 °C. Protein concentrations were determined according to the instructions of the manufacturer using the bicinchoninic acid-based, BCA Protein Assay Kit (Pierce Biotechnology, Rockford, IL, USA). Protein extracts (30-50 µg) were denaturated in Laemmli buffer at 95 °C for 5 min, separated electrophoretically by sodium dodecyl sulphate polyacrylamide gel electrophoresis (SDS-PAGE) and transferred onto nitrocellulose membrane (Bio-Rad, Munich, Germany) using a Bio-Rad wet transfer system (Bio-Rad, Munich, Germany). The membranes were incubated in blocking buffer (Tris-buffered saline with Tween 1x with 5% bovine serum albumin (Sigma-Aldrich, Taufkirchen, Germany) for 1 hour followed by overnight incubation with respective primary antibody at 4 °C, and subsequently with the corresponding secondary antibodies. The blots were developed using a technique based on a chemiluminescent reaction. The gel pictures were obtained using photographic films (Amersham Hyperfilm enhanced chemiluminescence (GE Healthcare, Little Chalfont, UK)).

3.6 RhoA pull-down assay

Activated RhoA was assessed using the Rho activation assay kit (Cytoskeleton, Denver, USA) according to the manufacturer's protocol.

3.7 Immunocytology and Immunohistology

The cells were plated on poly-L-lysine (Sigma- Aldrich; Taufkirchen, Germany) coated coverslips, cultured for 60 min in standard conditions, and fixed in 4% paraformaldehyde (PFA) at 37 °C for immunocytology. For immunohistology, brains were isolated and embedded in paraffin using standard protocol. Paraffin-embedded brain sections of 10 µm were deparaffinized and stained with Hematoxylin and Eosin

(H&E) or Gallyas or 3, 3'-Diaminobenzidine (DAB) staining following standard protocols. For staining, coverslips/brain sections were blocked in staining buffer (10% donkey normal serum/3% BSA, 0.2% gelatin, 0.25% Triton X-100 in PBS 1x) for 30 min at room temperature (RT), followed by overnight incubation with primary antibodies and corresponding secondary antibodies for 2 hours at RT. Nuclei were labelled with 4',6-diamidino-2-phenylindole (DAPI, 1:1,000, Sigma-Aldrich, Taufkirchen, Germany). Imaging was done using a fluorescence Olympus BX51 microscope with the software Magnafire 2.1B (Olympus, Hamburg, Germany), Olympus BX60 Axiovision microscope or Zeiss Spinning Disc microscopy system CXU-S1 with ZEN 2012 software and all images were processed using Adobe Photoshop, and ImageJ.

3.8 Quantification of cell viability, apoptosis, and proliferation

Fibroblasts were plated at a density of 10^3 cells per well in 96-well plates for experiments performed to quantify cell viability, proliferation, and apoptosis. Cell viability, proliferation rate and apoptosis of fibroblasts were measured using fluorimetric CellTiter-Blue Cell Viability assay (Promega, Madison, WI), 5-bromo-2-deoxyuridine (BrdU) Cell Proliferation ELISA (Roche, Mannheim, Germany), ApoONE Homogeneous Caspase 3/7 Assay (Promega, Madison, WI) according to the manufacturer's instructions, respectively. All measurements were taken using the Synergy 2 Multi-Mode Microplate Reader (BioTek Instruments, Winooski, VT, USA) and the Gen5TM software version 1.02.8 (BioTek Instruments, Winooski, VT, USA).

3.9 Statistical analysis and graphical representation

The statistical analysis for all the collected data was performed using the GraphPad Prism software, version 6.0.

4 Results

4.1 Clinical and cellular phenotype of MCPH2 patient with *WDR62* mutation.

We identified a compound heterozygous mutation in the *WDR62* gene of German descent with congenital microcephaly and ID: missense mutation c.1313G>A (p.R438H) and frameshift mutation c.2864-2867delACAG (p.D955Afs*112) (Figure 2). Cranial MRI analysis showed further abnormalities such as small frontal lobes, dysgenesis of corpus callosum, simplified hippocampal gyration, and cerebellar hypoplasia. Such abnormalities have been reported in association with MCPH2. The patient had severe intellectual delay and moderate delay in motor development. Despite more than 27 families being reported with *WDR62* mutation, we described for the first time the cellular phenotype of a patient with MCPH2.

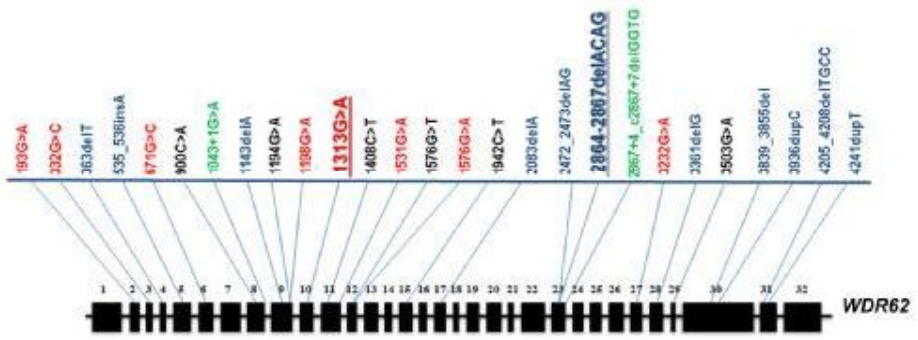

Figure 2. Known *WDR62* mutations causing MCPH2. Mutations types are color-coded (missense in red, frameshift in blue, nonsense in black, and splice site mutations in green). Two heterozygous mutations in the *WDR62* gene (bold letters) of our index patient and other reported mutations.

Since MCPH2 is associated with small brain volume and abnormal cell proliferation, we analyzed the effect of identified *WDR62* mutation on centrosomal integrity and the spindle apparatus in patient LCLs. In control LCLs, WDR62 is localised to centrosomal γ-tubulin throughout mitosis with reduced intensity during interphase and end of mitotic phases. In patient LCLs, WDR62 level was strongly reduced, and γ-tubulin-stained centrosomes were more dispersed and broad compared to those in controls (Figure 3A, C). Additionally, CDK5RAP2 levels were significantly reduced in patient cells. Analysis of the spindle apparatus revealed an increase in abnormal spindles (broad and unfocused microtubules poles) and spindle pole distance in patient LCLs compared to the normal bipolar appearance of mitotic spindles in controls (Figure

3B, C). Our findings support partially that the identified mutation accounts for the phenotype observed in our index patient.

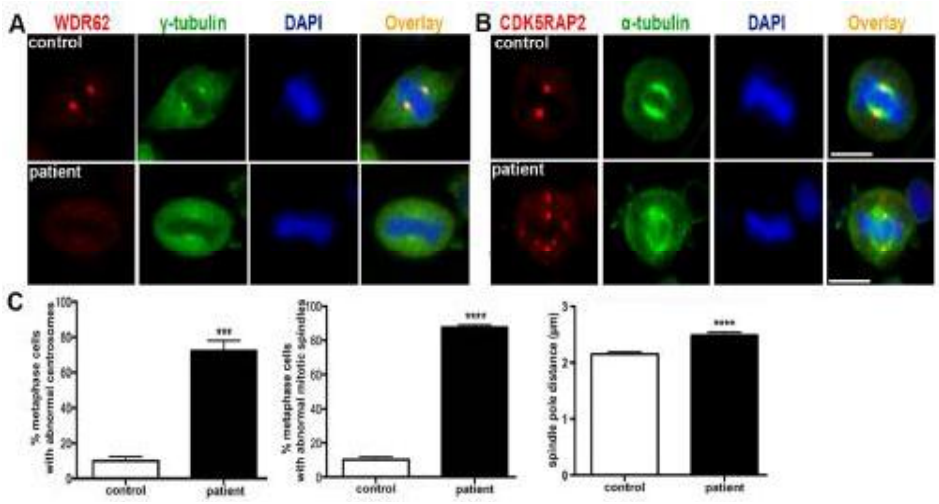

Figure 3. Effect of identified *WDR62* mutation in patient LCLs. (A) Dispersed centrosomal γ-tubulin protein (green) and reduced WDR62 (red) in WDR62 patient LCLs. **(B)** Abnormal mitotic spindles (green) and dispersed CDK5RAP2 (red) in metaphase of patient cells. **(C)** Quantification of abnormal centrosomes, disrupted spindle morphology, and increased spindle pole distance (***p < 0.001, ****p < 0.0001, Student's t-test).

4.2 CDK5RAP2 loss affects neural, but not non-neural differentiation process

To study the stem cell defect in MCPH3, we downregulated *Cdkrap2* in mESC through lentiviral infection. shRNAi downregulation of *Cdk5rap2* in undifferentiated mESC reduces the growth rate of cell culture, as a cause of reduction in proliferation (Figure 4A, B). Upon neural induction in mESC, the control cells undergone a rapid proliferation and increase of cell clusters, whereas the *Cdk5rap2*-downregulated clones showed a significant reduction in the proliferation rate and cell survival with less cell cluster numbers. In concomitant with reduced proliferation, the knockdown of *Cdk5rap2* caused an increase in apoptosis upon neural differentiation (Figure 4C, D). In order to substantiate the concept of premature neurogenesis as a cause of MCPH in our *Cdk5rap2*-shRNAi downregulated mESC model, we quantified the number of Oct4 (stem cell marker) and NeuN (mature neuronal marker) upon differentiation. Increased number of NeuN positive cells were detected in knockdown condition compared to controls, as a sign of premature neurogenesis (data not shown). These results indicate that in addition to premature differentiation, accumulating proliferation defect and

apoptosis of early differentiating cells might contribute to the microcephalic phenotype in MCPH3.

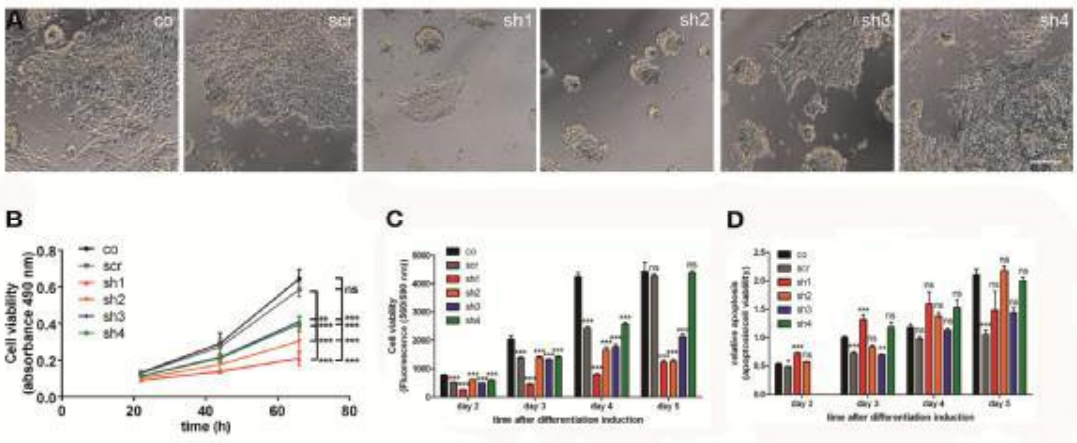

Figure 4. Defective proliferation and cell viability in *Cdk5rap2*-shRNA downregulated mESC. (A) Representative DIC pictures of control and *Cdk5rap2* downregulated mESC cultures at DIV3 (Scale bar 100 µm). **(B)** Reduced cell viability of *Cdk5rap2*-shRNAi-undifferentiated mESC**. (C)** Reduced cell viability, and **(D)** Relative apoptosis of mESC upon neural differentiation (*p<0.05, **p<0.01, ***p < 0.001, ns-non-significant, One-way ANOVA).

To address the neural-specific role of Cdk5rap2, we studied the effect of loss of Cdk5rap2 in differentiation of mESC into cardiac lineage. Interestingly, the cardiac differentiation was not affected in *Cdk5rap2* shRNAi downregulated mESCs as in control mESC (Figure 5A-B).

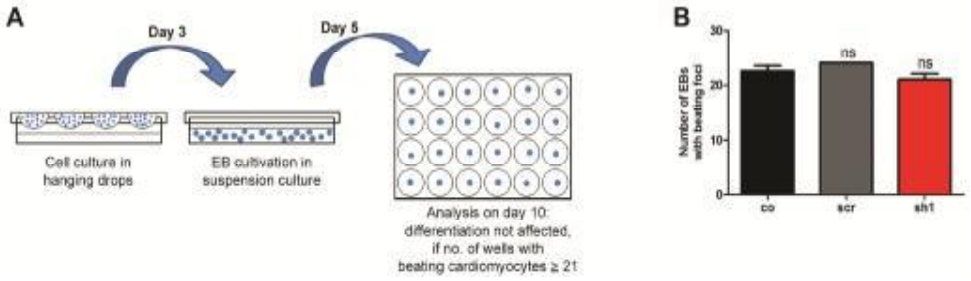

Figure 5. Non-neural differentiation of mESC into cardiomyocytes not affected in *Cdk5rap2*-downregulated mESC. (A) Diagrammatic representation of mESC culture differentiation into cardiomyocytes and its evaluation **(B)** Cardiac differentiation of mESC was not affected in the *Cdk5rap2*-shRNAi downregulated clones (ns, not significant; One-way ANOVA)**.**

4.3 Novel mid-hindbrain malformation with mild microcephaly and ID caused by biallelic *ARHGEF2* mutation

We report for the first time a novel mid-hindbrain defect associated with microcephaly and ID due to homozygous mutation in the *ARHGEF2*. The two affected children of consanguineous Kurdish-Turkish descent were reported with congenital microcephaly, moderate ID and various other clinical symptoms such as facial dysmorphism, nystagmus, and strabismus. Cranial MRI revealed microcephaly along with elongated midbrain, hypoplasia of the pons, ventral and dorsal longitudinal clefts (grooves) in pons and medulla, and inferior vermis hypoplasia**.** We identified a homozygous deletion of the base pair G at the intron-exon boundary (GG straddling the intron 12-exon 12 boundary) causing a deletion of G from the cDNA and ultimately a frameshift mutation (c.1461delG, NM_004723.3) (Figure 6A). The identified mutation in *ARHGEF2* leads to significant reduction of its protein and mRNA level in the LCLs of patients compared to control and heterozygous parents, due to partial nonsense-mediated decay (Figure 6B, C).

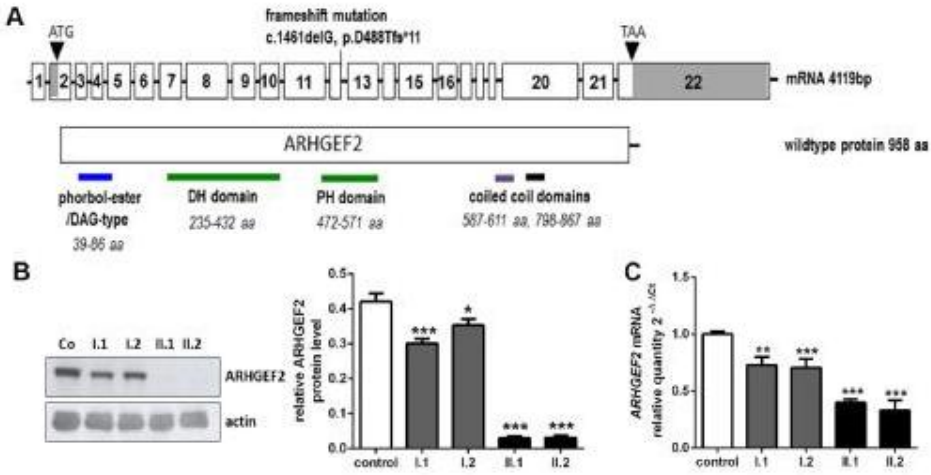

Figure 6. Novel *ARHGEF2* mutation and its effect on protein and mRNA level. (A) Homozygous mutation in the exon 12 (c.1461delG) of the *ARHGEF2* gene. **(B)** Significant reduction of ARHGEF2 protein and **(C)** its mRNA level in patient LCLs (*p<0.05, **p<0.01, ***p < 0.001, One-way ANOVA).

To address the disease-causative effect of identified *ARHGEF2* mutation, we studied the effect of the mutation on stem cell proliferation, and differentiation using *in vivo* and *in vitro* models. In the experimental setup, the E13 murine cortical precursor cells were transfected with the EGFP reporter plasmid and the *Arhgef2* shRNA construct, with or without wildtype (wt) or mutant human *ARHGEF2* (mut) constructs.

After three days, the cells were stained for βIII-tubulin (neuron marker), Ki67 (proliferation marker), EGFP, and quantified. The knockdown of ARHGEF2 resulted in significant decrease of βIII-tubulin positive neurons and increased Ki67-positive precursor cells in the system. The rescue experiment with wildtype human *ARHGEF2* rescued the phenotype, but mutant human *ARHGEF2* could not (Figure 7A). For *in vivo* experiments, the E13.5 mouse cortices were electroporated with *Arhgef2* shRNA, with either wildtype or mutant *ARHGEF2* constructs, and the brains were immunostained for EGFP (transfected cells) and Satb2 (neurons). As shown in Fig. 2B, there is an increased percentage of EGFP-positive cells in the cortical plate in wildtype-*ARHGEF2* electroporated brain compared to mutant *ARHGEF2* condition. In addition, the mutant *ARHGEF2* electroporated brain represented a significant decrease in the proportion of EGFP/Satb2-positive neurons compared to the wildtype *ARHGEF2* and control condition (Figure 7B). Also, analysis of spindle plane orientation in the electroporated brain sections revealed that the knockdown of *Arhgef2* favors symmetric proliferation, which is rescued by the wildtype, but not by mutant *ARHGEF2* (data not shown).

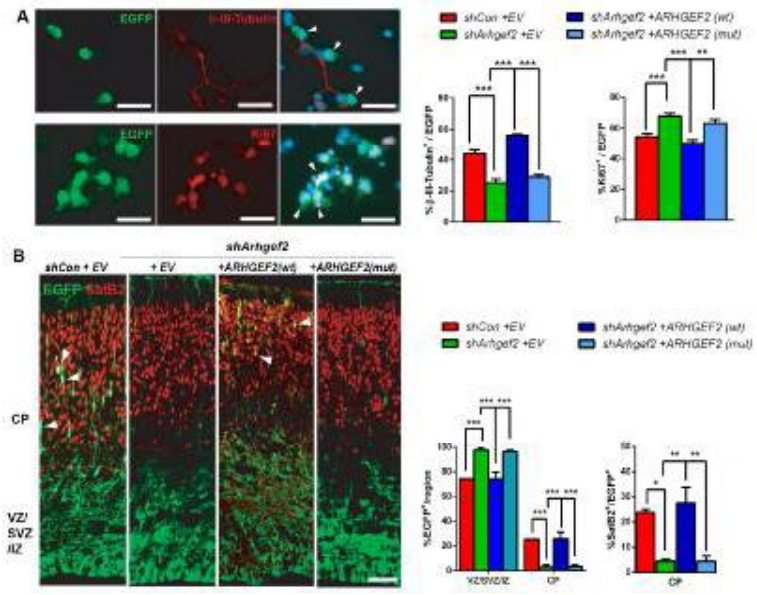

Figure 7: Wildtype, not mutant *ARHGEF2* rescues *Arhgef2*-knockdown function. (A) *ARHGEF2* downregulation inhibits neurogenesis and maintains murine neural precursor cells (NPCs) in cycling phase. This phenotype can be rescued through upregulation of wild-type (wt) but not mutant (mut) *ARHGEF2*; Representative fluoromicrographs of EGFP-transfected NPCs stained for neuronal (βIII-tubulin) and progenitor (Ki67) markers (Immunofluorescence, scale bar 25 μm) and its quantification across various experimental conditions. **(B)** *In utero* electroporation of mouse embryonic cortices with *Arhgef2* shRNA, with empty vector (EV) or wildtype or mutant *ARHGEF2* constructs and analyzed for its

effect on neurogenesis. Representative fluoromicrographs of electroporated brain sections with EGFP-transfected cells and Satb2-positive neurons (Immunofluorescence, scale bar 50 µm) and its quantification across various experimental conditions (*p<0.05, **p<0.01, ***p<0.001, One-way ANOVA).

The effect of *ARHGEF2* mutation on cell cycle apparatus was assessed on patient LCLs. Our analysis revealed abnormal mitotic spindles, reduced spindle pole distance, and cell size in patient cells compared to controls. Additionally, we detected a significant reduction of active RhoA and MLC in patient LCLs, indicative of impaired RhoA-MLC pathway, crucial for cytoskeletal dynamics, neurogenesis and migration (data not shown).

To further substantiate the role of ARHGEF2 in brain development, we analyzed the phenotype of *Arhgef2* deficient mice. In the adult *Arhgef2* mutant mice, we reported a significant reduction in volume of the total brain size, the cerebellum, and the brainstem, as well as the absence of pontine nuclei (Figure 8A-C, n=3-4, Student's *t-test*). We concluded that the loss of Arhgef2 in mice recapitulate the brain malformations observed in the index patients.

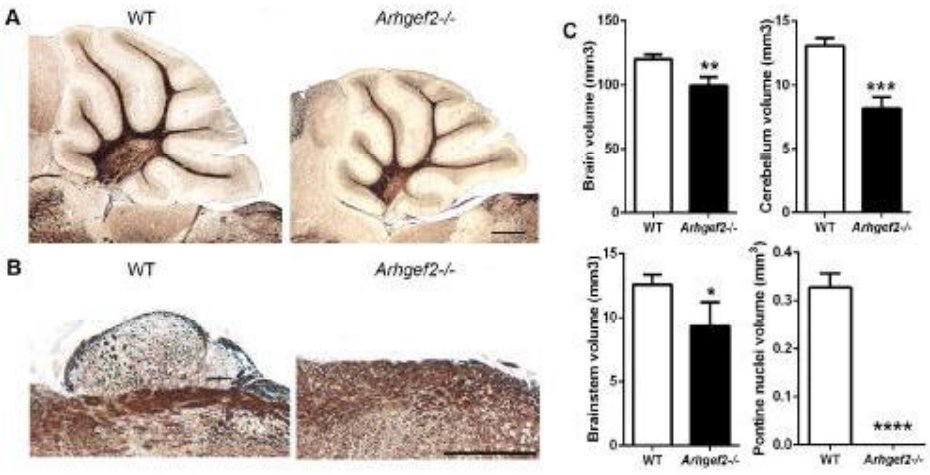

Figure 8. Microencephaly, cerebellar hypotrophy, and lack of pontine nuclei in *Arhgef2-/-* mutant mice. (A, B) Reduced cerebellar size and lack of pontine nuclei in adult *Arhgef2* mutant mice compared to wild type (Gallyas staining, DIC images, scale bar 500 µm). **(C)** Quantification showing significant volume reduction of whole brain, cerebellum, brain stem, and pontine nuclei in mutant compared to wildtype brains (*p<0.05, **p<0.01, ***p<0.001, ****p<0.0001, Student's t-test).

Further analysis of *Arhgef2* mutant mice brain revealed no difference in the cortical layer distribution and midbrain structures. Despite reduced cerebellar size, the mutant mice had normal cerebellar Molecular layer thickness and Purkinje cell size as in

controls. Thus, we hypothesized that the reduced cerebellar size might be due to defective precerebellar nuclei formation, in turn its projection to the cerebellum. To confirm our hypothesis, we stained the brain sections with precerebellar nuclei marker, Mbh2. The analysis revealed that the *Arhgef2* mutant mice specifically lack pontine gray nuclei (PGN), and reticulotegmental nuclei (RTN), with massive reduction of lateral reticular nuclei (LRN), and abnormally enlarged external cuneate nuclei (ECN), whereas the other nuclei such as inferior olive (IO), and solitary tract nuclei (NTS) remains intact (Figure 9A-D). Our findings reveal that the loss of Arhgef2 impinge the formation of precerebellar nuclei from dA1-derived progenitors, probably due to impaired anterior and posterior extramural migratory streams (AES and PES) in the developing hindbrain.

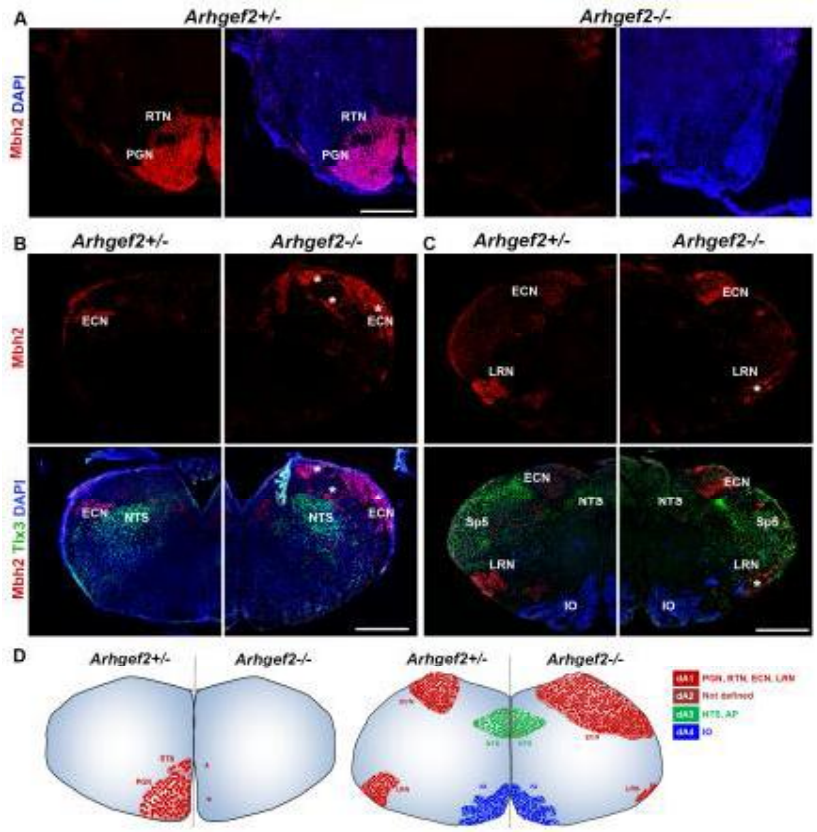

Figure 9. Loss of Arhgef2 affects dA1-derived precerebellar nuclei formation. Representative fluorescence micrographs of coronal hindbrain sections of *Arhgef2-/-* and *Arhgef2+/-* mice, stained with precerebellar neuronal marker Mbh2 (red), Tlx3 (green), and DAPI (scale bar 300 µm). **(A)** *Arhgef2-/-* mutant mice lack PGN and RTN. **(B, C)** In the medulla of *Arhgef2-/-* mice, the ECN is abnormally enlarged and distributed (indicated by stars), and LRN is severely reduced in size when compared to *Arhgef2+/-* mice, whereas the IO and NTS are unaffected. **(D)** Pictogram representing the abnormal

formation of dA1-derived precerebellar nuclei (red) and normal formation of dA3 (green) and dA4 (blue) nuclei in the *Arhgef2-/-* mice brain compared to the control condition.

4.4 Syndromic ID caused by biallelic *ZBTB24* mutation

We identified the homozygous missense mutation c.1222 T >G in the *ZBTB24* (NM_014797) of the index patient of non-consanguineous German descent (Figure 10A). Biallelic mutations in *ZBTB24* have been associated previously with immunodeficiency-centromeric instability-facial anomalies syndrome type 2 (ICF2), a disease characterized by immunodeficiency, developmental delay, and facial anomalies. Initially, ICF2 was primarily recognized as a B-cell defect. The index patient showed multiple facial anomalies, clubbing of fingers and toes, stagnant growth and intellectual disability. Cranial MRI analysis revealed normal brain morphology apart from pineal cyst. Immunological analysis over the period of years affirmed that our ICF2 patient had developed combined immunodeficiency (B/T-cell defect), which has not been reported before in ICF2. Additionally, our index patient has defective neutrophil differentiation, granulomatous nephritis and hepatosplenomegaly as signs of autoimmune disease.

As ICF is proclaimed to be an immune disorder, the non-immunological phenotype of the syndrome has never been addressed. For the first time, we analyzed patient fibroblasts and found that the identified mutation causes significant reduction of cell viability, proliferation, and increased apoptosis (Figure 10B-D). At cellular level, abnormal mitotic spindles with reduced centrosomal CDK5RAP2 were observed in patient LCLs (Figure 10E). Thus, our findings contribute as a putative mechanism underlying the variable phenotype in ICF.

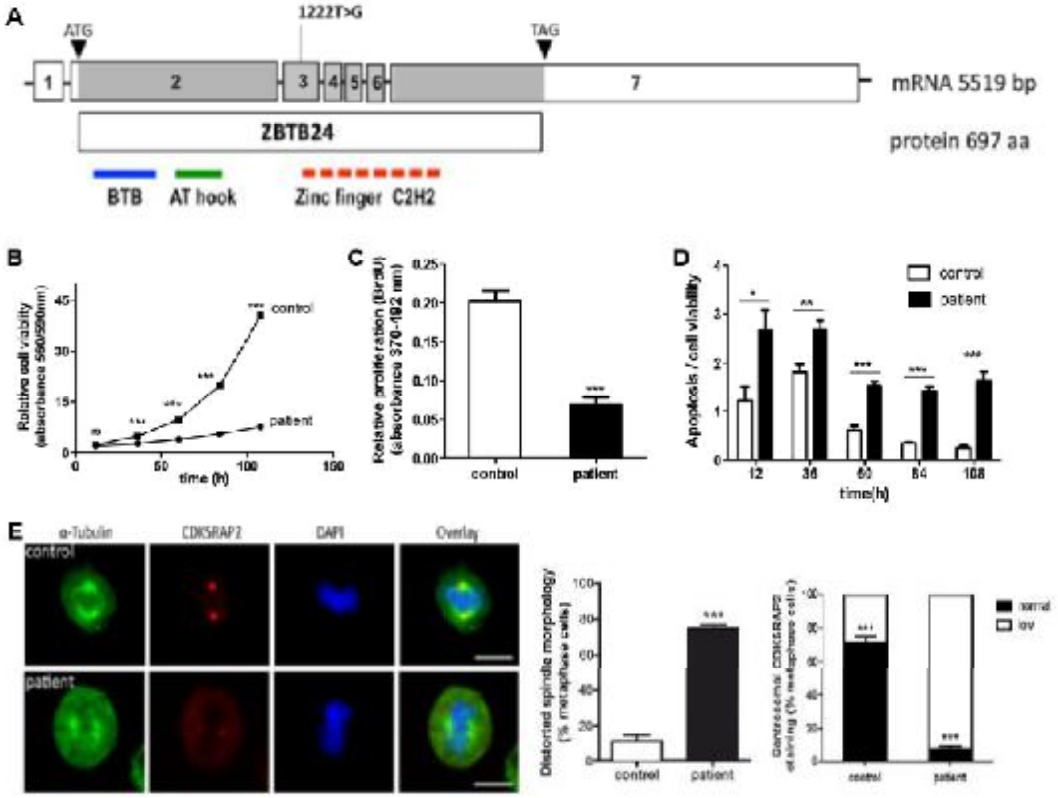

Figure 10. Homozygous mutation in *ZBTB24* leads to defective cell cycle apparatus. (A) Homozygous *ZBTB24* mutation (c.1222T>G). **(B)** Reduced cell viability, (C) reduced proliferation, and (D) increased apoptosis of patient fibroblasts **(E)** Abnormal mitotic spindles (green) and reduced centrosomal CDK5RAP2 level (red) in patient LCLs and its quantification (*p<0.05, **p<0.01, ***p < 0.001, Student's t-test).

5 Discussion

Various studies have proposed a model for MCPH suggesting that a premature shift from symmetric to asymmetric cell divisions in the developing neocortex leads to premature neurogenesis and subsequent depletion of the progenitor cell pool, culminating in microcephaly. The proposed model is primarily based on the underlying mechanism that the loss of microcephaly genes causes mitotic spindle instability, improper cleavage plane orientation, lack of centrosomal integrity, and/or dysregulation of DNA repair mechanism.(14,16,39) In my PhD project, I focussed on identifying the novel genes causing ID and microcephaly and characterize mechanisms underlying known and novel disease phenotypes.

In our study on MCPH2, we report two heterozygous *WDR2* mutation in our index patient with primary microcephaly, and intellectual disability. Even though, MCPH is defined as severe primary microcephaly with normal architecture of the brain, recently, more reports are consistent in reporting MCPH2 with additional brain malformations, as in our index patient.(15,17) As reported on various cells,(16,18) we showed the intracellular localization of WDR62 on centrosomes across cell cycle, with low levels during anaphase and telophase in human LCLs. We have shown for the first time that the loss of WDR62 in MCPH2 patients causes abnormal mitotic spindles, increased spindle pole distance, and lagging chromosomes. In addition, our index patient LCLs displayed an improper centrosomal localization of γ-tubulin and CDK5RAP2, indicating an abnormal centrosomal integrity. It is interesting to note the convergence of MCPH3 gene, *CDK5RAP2*, at the centrosomal phenotype in MCPH2. Our findings on human LCLs, along with the previous reports on *WDR62* downregulation in both *in vivo* and *in vitro*,(18) emphasize the significance of relationship between proper centrosome attachment to mitotic spindle, spindle pole length determination, and chromosome segregation. After our publication on cellular phenotypes in MCPH2 patient, it has been shown that WDR62 regulates mitotic progression of NPCs through AuroraA and its depletion leads to mitotic delay and cell death, thereby causing microcephaly in MCPH2.(40)

In MCPH3, caused by biallelic mutation in *CDK5RAP2*, the underlying mechanisms include dysregulated function of CDK5RAP2 in centrosome and mitotic spindle function, as well as in DNA repair mechanism.(22) We have already reported

defective mitotic spindles, abnormal centrosomal integrity, and lagging chromosomes in the LCLs of MCPH3 patients.(21) In addition to the existing literature on *Hertwig's anemia* mice, our results from the downregulation of *Cdk5rap2* in mESC reveals defective proliferation, and increased apoptosis in undifferentiated as well as neurally differentiating mESCs. Also, the increased proportion of NeuN-positive neurons in *Cdk5rap2*-downregulated mESC upon neural induction supports the popular model of premature neuronal differentiation in MCPH. Conversely, differentiation of *Cdk5rap2*-knockdown mESC into cardiomyocytes was not affected, which explains the lack of non-neurological phenotype in MCPH3 patients.(21) Taken together, in addition to premature neuronal differentiation, accumulating proliferating defect of differentiating cells and increased cell death of differentiating and early postmitotic cells contribute to microcephaly in MCPH3. Recently, our group had shown that the germ cell depletion in *Hertwig's anemia* mice as a cause of mitotic delay, prolonged cell cycle, and increased apoptosis.(41)

Along with the widening spectrum of ID, we report for the first time a homozygous mutation in *ARHGEF2* causing ID associated with mild primary (congenital) microcephaly, and novel mid-hindbrain malformation. As we have reported for other microcephaly-related genes above, the loss of ARHGEF2 resulted in distorted mitotic spindle morphology, reduced spindle pole distance, reduced cell size, and impaired RhoA/ROCK/MLC pathway in the patient LCLs. Our results further reinforce the significant function of ARHGEF2 in microtubule localization, formation, stability, and migration.(26-28,30) Several studies have also proven the role of ARHGEF2 in nervous system development, particularly by favoring neurogenesis through cleavage plane orientation.(29) Evidently, our rescue experiments with wildtype/mutant ARHGEF2 in the mouse brain proves that the loss of ARHGEF2 inhibits neurogenesis by favoring more of symmetric divisions in the ventricular zone. In contrast to existing model for microcephaly, we propose that the loss of ARHGEF2 inhibits neurogenesis by increasing symmetric proliferation through improper cleavage plane orientation, and thereby reduced post-mitotic cells in the brain resulting in microcephaly.

We also highlight the role of ARHGEF2 in brain development across species by mimicking the human phenotype in *Arhgef2* mutant mice. As in our index patients, *Arhgef2* mutant mice displayed significant reduction of whole brain volume and

hypotrophy of pons and cerebellum. Our *in situ* hybridization data along with previous reports,(29) shows a clear correspondence between regions expressing high levels of *Arhgef2* and pathologically affected brain regions. In-depth analysis revealed normal cortical and midbrain structures in *Arhgef2* mutant mice. We show that the loss of Arhgef2 specifically impairs the migration of dA1 progenitors, culminating in the improper formation of precerebellar neurons, thereby reduced cerebellar projections and reduced cerebellar size in the *Arhgef2* mutant mice. Our results along with the previous evidence on role of RhoA/ROCK pathway in precerebellar neuron migration,(42) further strongly augments the role of Arhgef2 in AES and PES neuronal migratory stream through Planar Cell Polarity pathway (PCP). In addition to the role of ARHGEF2 in mitotic spindles stability and neurogenesis, our findings revealed the specific role in the molecular control of neuronal migration in the hindbrain, and as a possible underlying pathomechanism in this novel disease.

Finally, we report our index patient of German descent with ICF2 syndrome characterized by combined immunodeficiency, due to homozygous missense mutation in *ZBTB24*. Our patient has syndromic ID with normal architecture of the brain. The higher prevalence of ID in ICF2 might be due to higher expression of ZBTB24 in the caudate nucleus, an important region involved in learning and memory.(43) We report for the first time a defective cell survival with reduced proliferation, increased apoptosis and abnormal mitotic spindles in immune and non-immune cells, explaining the putative mechanism of immunological and non-immunological phenotype of ICF2. The mechanism underlying the reduced levels of CDK5RAP2 and also abnormal mitotic spindles, might contribute to the neurological phenotype in ICF2, as described for MCPH3.(22) Recent report has shown a functional convergence between ICF-related genes (*Dnmt3b* and *Hells*, *Zbtb24* and *Cdca7*), suggesting a putative common mechanism underlying the ICF syndrome.

ID and MCPH, being widely heterogeneous, we described the common pathomechanism underlying the known MCPH/novel disease described above: abnormal proliferation, apoptosis, and/or migration due to defective mitotic spindles and centrosomal integrity. Recent findings on microcephaly caused by ZIKV have shown that deregulated proliferation and apoptosis of neural precursor cells underlines the disease phenotype.(44)

6 References

1. Kaindl AM, Passemard S, Kumar P, Kraemer N, Issa L, Zwirner A, Gerard B, Verloes A, Mani S, Gressens P. Many roads lead to primary autosomal recessive microcephaly. Prog Neurobiol 2010;90:363-83.
2. Woods CG. Human microcephaly. Curr Opin Neurobiol 2004;14:112-7.
3. Woods CG, Bond J, Enard W. Autosomal recessive primary microcephaly (MCPH): a review of clinical, molecular, and evolutionary findings. Am J Hum Genet 2005;76:717-28.
4. Ellison JW, Rosenfeld JA, Shaffer LG. Genetic basis of intellectual disability. Annu Rev Med 2013;64:441-50.
5. Ropers HH, Hamel BC. X-linked mental retardation. Nat Rev Genet 2005;6:46-57.
6. Chiurazzi P, Pirozzi F. Advances in understanding - genetic basis of intellectual disability. F1000Res 2016;5.
7. Stiles J, Jernigan TL. The basics of brain development. Neuropsychol Rev 2010;20:327-48.
8. Tau GZ, Peterson BS. Normal development of brain circuits. Neuropsychopharmacology 2010;35:147-68.
9. Rice D, Barone S, Jr. Critical periods of vulnerability for the developing nervous system: evidence from humans and animal models. Environ Health Perspect 2000;108 Suppl 3:511-33.
10. Gilbert SL, Dobyns WB, Lahn BT. Genetic links between brain development and brain evolution. Nat Rev Genet 2005;6:581-90.
11. Kaindl AM. Autosomal recessive primary microcephalies (MCPH). Eur J Paediatr Neurol 2014;18:547-8.
12. Faheem M, Naseer MI, Rasool M, Chaudhary AG, Kumosani TA, Ilyas AM, Pushparaj P, Ahmed F, Algahtani HA, Al-Qahtani MH, Saleh Jamal H. Molecular genetics of human primary microcephaly: an overview. BMC Med Genomics 2015;8 Suppl 1:S4.
13. Li H, Bielas SL, Zaki MS, Ismail S, Farfara D, Um K, Rosti RO, Scott EC, Tu S, Chi NC, Gabriel S, Erson-Omay EZ, Ercan-Sencicek AG, Yasuno K, Caglayan AO, Kaymakcalan H, Ekici B, Bilguvar K, Gunel M, Gleeson JG. Biallelic Mutations in Citron

Kinase Link Mitotic Cytokinesis to Human Primary Microcephaly. Am J Hum Genet 2016;99:501-10.

14. Sun T, Hevner RF. Growth and folding of the mammalian cerebral cortex: from molecules to malformations. Nat Rev Neurosci 2014;15:217-32.

15. Bilguvar K, Ozturk AK, Louvi A, Kwan KY, Choi M, Tatli B, Yalnizoglu D, Tuysuz B, Caglayan AO, Gokben S, Kaymakcalan H, Barak T, Bakircioglu M, Yasuno K, Ho W, Sanders S, Zhu Y, Yilmaz S, Dincer A, Johnson MH, Bronen RA, Kocer N, Per H, Mane S, Pamir MN, Yalcinkaya C, Kumandas S, Topcu M, Ozmen M, Sestan N, Lifton RP, State MW, Gunel M. Whole-exome sequencing identifies recessive WDR62 mutations in severe brain malformations. Nature 2010;467:207-10.

16. Nicholas AK, Khurshid M, Desir J, Carvalho OP, Cox JJ, Thornton G, Kausar R, Ansar M, Ahmad W, Verloes A, Passemard S, Misson JP, Lindsay S, Gergely F, Dobyns WB, Roberts E, Abramowicz M, Woods CG. WDR62 is associated with the spindle pole and is mutated in human microcephaly. Nat Genet 2010;42:1010-4.

17. Yu TW, Mochida GH, Tischfield DJ, Sgaier SK, Flores-Sarnat L, Sergi CM, Topcu M, McDonald MT, Barry BJ, Felie JM, Sunu C, Dobyns WB, Folkerth RD, Barkovich AJ, Walsh CA. Mutations in WDR62, encoding a centrosome-associated protein, cause microcephaly with simplified gyri and abnormal cortical architecture. Nat Genet 2010;42:1015-20.

18. Bogoyevitch MA, Yeap YY, Qu Z, Ngoei KR, Yip YY, Zhao TT, Heng JI, Ng DC. WD40-repeat protein 62 is a JNK-phosphorylated spindle pole protein required for spindle maintenance and timely mitotic progression. J Cell Sci 2012;125:5096-109.

19. Moynihan L, Jackson AP, Roberts E, Karbani G, Lewis I, Corry P, Turner G, Mueller RF, Lench NJ, Woods CG. A third novel locus for primary autosomal recessive microcephaly maps to chromosome 9q34. Am J Hum Genet 2000;66:724-7.

20. Bond J, Roberts E, Springell K, Lizarraga SB, Scott S, Higgins J, Hampshire DJ, Morrison EE, Leal GF, Silva EO, Costa SM, Baralle D, Raponi M, Karbani G, Rashid Y, Jafri H, Bennett C, Corry P, Walsh CA, Woods CG. A centrosomal mechanism involving CDK5RAP2 and CENPJ controls brain size. Nat Genet 2005;37:353-5.

21. Issa L, Mueller K, Seufert K, Kraemer N, Rosenkotter H, Ninnemann O, Buob M, Kaindl AM, Morris-Rosendahl DJ. Clinical and cellular features in patients with primary autosomal recessive microcephaly and a novel CDK5RAP2 mutation. Orphanet J Rare Dis 2013;8:59.

22. Kraemer N, Issa L, Hauck SC, Mani S, Ninnemann O, Kaindl AM. What's the hype about CDK5RAP2? Cell Mol Life Sci 2011;68:1719-36.
23. Kiecker C, Lumsden A. The role of organizers in patterning the nervous system. Annu Rev Neurosci 2012;35:347-67.
24. Barkovich AJ, Millen KJ, Dobyns WB. A developmental and genetic classification for midbrain-hindbrain malformations. Brain 2009;132:3199-230.
25. Hodge RG, Ridley AJ. Regulating Rho GTPases and their regulators. Nat Rev Mol Cell Biol 2016;17:496-510.
26. Birkenfeld J, Nalbant P, Yoon SH, Bokoch GM. Cellular functions of GEF-H1, a microtubule-regulated Rho-GEF: is altered GEF-H1 activity a crucial determinant of disease pathogenesis? Trends Cell Biol 2008;18:210-9.
27. Bakal CJ, Finan D, LaRose J, Wells CD, Gish G, Kulkarni S, DeSepulveda P, Wilde A, Rottapel R. The Rho GTP exchange factor Lfc promotes spindle assembly in early mitosis. Proc Natl Acad Sci U S A 2005;102:9529-34.
28. Krendel M, Zenke FT, Bokoch GM. Nucleotide exchange factor GEF-H1 mediates cross-talk between microtubules and the actin cytoskeleton. Nat Cell Biol 2002;4:294-301.
29. Gauthier-Fisher A, Lin DC, Greeve M, Kaplan DR, Rottapel R, Miller FD. Lfc and Tctex-1 regulate the genesis of neurons from cortical precursor cells. Nat Neurosci 2009;12:735-44.
30. Itoh K, Ossipova O, Sokol SY. GEF-H1 functions in apical constriction and cell intercalations and is essential for vertebrate neural tube closure. J Cell Sci 2014;127:2542-53.
31. Kutsche K, Yntema H, Brandt A, Jantke I, Nothwang HG, Orth U, Boavida MG, David D, Chelly J, Fryns JP, Moraine C, Ropers HH, Hamel BC, van Bokhoven H, Gal A. Mutations in ARHGEF6, encoding a guanine nucleotide exchange factor for Rho GTPases, in patients with X-linked mental retardation. Nat Genet 2000;26:247-50.
32. Marco EJ, Abidi FE, Bristow J, Dean WB, Cotter P, Jeremy RJ, Schwartz CE, Sherr EH. ARHGEF9 disruption in a female patient is associated with X linked mental retardation and sensory hyperarousal. J Med Genet 2008;45:100-5.
33. Ekenstedt KJ, Becker D, Minor KM, Shelton GD, Patterson EE, Bley T, Oevermann A, Bilzer T, Leeb T, Drogemuller C, Mickelson JR. An ARHGEF10 deletion

is highly associated with a juvenile-onset inherited polyneuropathy in Leonberger and Saint Bernard dogs. PLoS Genet 2014;10:e1004635.

34. Zahir FR, Brown CJ. Epigenetic impacts on neurodevelopment: pathophysiological mechanisms and genetic modes of action. Pediatr Res 2011;69:92R-100R.

35. Kramer JM, van Bokhoven H. Genetic and epigenetic defects in mental retardation. Int J Biochem Cell Biol 2009;41:96-107.

36. Hansen RS, Wijmenga C, Luo P, Stanek AM, Canfield TK, Weemaes CM, Gartler SM. The DNMT3B DNA methyltransferase gene is mutated in the ICF immunodeficiency syndrome. Proc Natl Acad Sci U S A 1999;96:14412-7.

37. de Greef JC, Wang J, Balog J, den Dunnen JT, Frants RR, Straasheijm KR, Aytekin C, van der Burg M, Duprez L, Ferster A, Gennery AR, Gimelli G, Reisli I, Schuetz C, Schulz A, Smeets DF, Sznajer Y, Wijmenga C, van Eggermond MC, van Ostaijen-Ten Dam MM, Lankester AC, van Tol MJ, van den Elsen PJ, Weemaes CM, van der Maarel SM. Mutations in ZBTB24 are associated with immunodeficiency, centromeric instability, and facial anomalies syndrome type 2. Am J Hum Genet 2011;88:796-804.

38. Thijssen PE, Ito Y, Grillo G, Wang J, Velasco G, Nitta H, Unoki M, Yoshihara M, Suyama M, Sun Y, Lemmers RJ, de Greef JC, Gennery A, Picco P, Kloeckener-Gruissem B, Gungor T, Reisli I, Picard C, Kebaili K, Roquelaure B, Iwai T, Kondo I, Kubota T, van Ostaijen-Ten Dam MM, van Tol MJ, Weemaes C, Francastel C, van der Maarel SM, Sasaki H. Corrigendum: Mutations in CDCA7 and HELLS cause immunodeficiency-centromeric instability-facial anomalies syndrome. Nat Commun 2016;7:12003.

39. Fish JL, Kosodo Y, Enard W, Paabo S, Huttner WB. Aspm specifically maintains symmetric proliferative divisions of neuroepithelial cells. Proc Natl Acad Sci U S A 2006;103:10438-43.

40. Chen JF, Zhang Y, Wilde J, Hansen KC, Lai F, Niswander L. Microcephaly disease gene Wdr62 regulates mitotic progression of embryonic neural stem cells and brain size. Nat Commun 2014;5:3885.

41. Zaqout S, Bessa P, Kramer N, Stoltenburg-Didinger G, Kaindl AM. CDK5RAP2 Is Required to Maintain the Germ Cell Pool during Embryonic Development. Stem Cell Reports 2017;8:198-204.

42. Causeret F, Hidalgo-Sanchez M, Fort P, Backer S, Popoff MR, Gauthier-Rouviere C, Bloch-Gallego E. Distinct roles of Rac1/Cdc42 and Rho/Rock for axon outgrowth and nucleokinesis of precerebellar neurons toward netrin 1. Development 2004;131:2841-52.

43. Weemaes CM, van Tol MJ, Wang J, van Ostaijen-ten Dam MM, van Eggermond MC, Thijssen PE, Aytekin C, Brunetti-Pierri N, van der Burg M, Graham Davies E, Ferster A, Furthner D, Gimelli G, Gennery A, Kloeckener-Gruissem B, Meyn S, Powell C, Reisli I, Schuetz C, Schulz A, Shugar A, van den Elsen PJ, van der Maarel SM. Heterogeneous clinical presentation in ICF syndrome: correlation with underlying gene defects. Eur J Hum Genet 2013;21:1219-25.

44. Tang H, Hammack C, Ogden SC, Wen Z, Qian X, Li Y, Yao B, Shin J, Zhang F, Lee EM, Christian KM, Didier RA, Jin P, Song H, Ming GL. Zika Virus Infects Human Cortical Neural Progenitors and Attenuates Their Growth. Cell Stem Cell 2016;18:587-90.

7 Affidavit and detailed statement of originality

I, Ethiraj Ravindran, certify under penalty of perjury by my own signature that I have submitted the thesis on the topic “Identification and characterization of mechanisms underlying intellectual disability”. I wrote this thesis independently and without assistance from third parties, I used no other aids than the listed sources and resources.

All points based literally or in spirit on publications or presentations of other authors are, as such, in proper citations (see "uniform requirements for manuscripts (URM)" the ICMJE www.icmje.org) indicated. The sections on methodology (in particular practical work, laboratory requirements, statistical processing) and results (in particular images, graphics and tables) correspond to the URM (s.o) and are answered by me. My contributions in the selected publications for this dissertation correspond to those that are specified in the following joint declaration with the responsible person and supervisor. All publications resulting from this thesis and which I am author of correspond to the URM (see above) and I am solely responsible.

The importance of this affidavit and the criminal consequences of a false affidavit (section 156,161 of the Criminal Code) are known to me and I understand the rights and responsibilities stated therein.

_____

Date Signature

8 Declaration of any eventual publications

Ethiraj Ravindran had the following share in the following publications:

Publication 1:

Heba Gamal Farag, Sebastian Froehler, Konrad Oexle, **Ethiraj Ravindran**, Detlev Schindler, Timo Staab, Angela Huebner, Nadine Kraemer, Wei Chen, Angela M Kaindl. Abnormal centrosome and spindle morphology in a patient with autosomal recessive primary microcephaly type 2 due to compound heterozygous WDR62 gene mutation. Orphanet Journal of Rare Diseases 2013; 8: 178. (Impact factor = 3.290)

Contribution: Ethiraj Ravindran maintained control and patient's LCLs in culture, performed immunostaining, Western blot, and limited contribution in analysis.

Publication 2:

Horst von Bernuth, **Ethiraj Ravindran**, Hang Du, Sebastian Fröhler, Karoline Strehl, Nadine Krämer, Lina Issa-Jahns, Borko Amulic, Olaf Ninnemann, Mei-Sheng Xiao, Katharina Eirich, Uwe Kölsch, Kathrin Hauptmann, Rainer John, Detlev Schindler, Volker Wahn, Wei Chen, Angela M. Kaindl. Combined immunodeficiency develops with age in Immunodeficiency centromeric instability-facial anomalies syndrome 2 (ICF2). Orphanet Journal of Rare Diseases 2014; 9:116. (Impact factor = 3.290)

Contribution: Ethiraj Ravindran performed cell viability, proliferation, and apoptosis assay in cultured fibroblasts. He performed immunocytology, Western blot, and analysis of cell cycle apparatus in LCLs and HEK cells. He also contributed in preparation of figures, data interpretation, and revised the manuscript.

Publication 3:

Nadine Kraemer, **Ethiraj Ravindran**, Sami Zaqout, Gerda Neubert, Detlev Schindler, Olaf Ninnemann, Ralph Gräf, Andrea EM Seiler & Angela M Kaindl. Loss of CDK5RAP2 affects neural but not non-neural mESC differentiation into cardiomyocytes. Cell Cycle 2015; 14:2044-57. (Impact factor = 3.952)

Contribution: Ethiraj Ravindran contributed in the analysis of mitotic spindle morphology,

centrosome integrity, and centrosomal protein level through Western blot.

Publication 4:

Nadine Kraemer, Lina Issa-Jahns, Gerda Neubert, **Ethiraj Ravindran**, Shyamala Mani, Olaf Ninnemann, Angela M. Kaindl. Novel Alternative Splice Variants of Mouse Cdk5rap2. PlosOne 2015; 10.1371. (Impact factor = 4.411)

Contribution: Ethiraj Ravindran performed Western blot to assess the level of Cdk5rap2 in the mutant mice samples.

Publication 5:

Ethiraj Ravindran, Hao Hu, Scott A. Yuzwa, Luis R. Hernandez-Miranda, Nadine Kraemer, Olaf Ninnemann, Luciana Musante, Eugen Boltshauser, Detlev Schindler, Angela Hübner, Hans-Christian Reinecker, Hans-Hilger Ropers, Carmen Birchmeier, Freda D. Miller, Thomas F. Wienker, Christoph Hübner, Angela M. Kaindl. Homozygous *ARHGEF2* mutation causes intellectual disability and midbrain-hindbrain malformation. PLos Genetics 2017; 10.1371. (Impact factor = 6.661)

Contribution: Ethiraj Ravindran maintained control and patient LCLs in culture and performed Sanger sequencing, immunostaining, qPCR, Western blot for several proteins. Analysis of spindle morphology, cell size, spindle pole distance, spindle plane orientation was performed. He performed immunohistological analysis on the mutant mice brain samples. He also contributed in analysis and interpretation of data, preparation of figures, drafting and revising the manuscript.

Signature, date and stamp of the supervising University teacher

_____

Signature of the doctoral candidate

_____

Farag et al. Orphanet Journal of Rare Diseases 2013, 8:178
http://www.ojrd.com/content/8/1/178

ORPHANET JOURNAL OF RARE DISEASES

RESEARCH Open Access

Abnormal centrosome and spindle morphology in a patient with autosomal recessive primary microcephaly type 2 due to compound heterozygous *WDR62* gene mutation

Heba Gamal Farag[1,2†], Sebastian Froehler[3†], Konrad Oexle[4], Ethiraj Ravindran[1,2], Detlev Schindler[5], Timo Staab[5], Angela Huebner[6], Nadine Kraemer[1,2], Wei Chen[3*] and Angela M Kaindl[1,2*]

Abstract

Background: Autosomal recessive primary microcephaly (MCPH) is a rare neurodevelopmental disease with severe microcephaly at birth due to a pronounced reduction in brain volume and intellectual disability. Biallelic mutations in the WD repeat-containing protein 62 gene *WDR62* are the genetic cause of MCPH2. However, the exact underlying pathomechanism of MCPH2 remains to be clarified.

Methods/results: We characterized the clinical, radiological, and cellular features that add to the human MCPH2 phenotype. Exome sequencing followed by Sanger sequencing in a German family with two affected daughters with primary microcephaly revealed in the index patient the compound heterozygous mutations c.1313G>A (p.R438H) / c.2864-2867delACAG (p.D955Afs*112) of *WDR62*, the second of which is novel. Radiological examination displayed small frontal lobes, corpus callosum hypoplasia, simplified hippocampal gyration, and cerebellar hypoplasia. We investigated the cellular phenotype in patient-derived lymphoblastoid cells and compared it with that of healthy female controls. WDR62 expression in the patient's immortalized lymphocytes was deranged, and mitotic spindle defects as well as abnormal centrosomal protein localization were apparent.

Conclusion: We propose that a disruption of centrosome integrity and/or spindle organization may play an important role in the development of microcephaly in MCPH2.

Keywords: Microcephaly, *WDR62* mutation, Cell division, Intellectual disability

Introduction

Autosomal recessive primary microcephaly (MCPH) is a rare neurodevelopmental disorder that results in severe microcephaly at birth with reduction in brain volume, simplified neocortical gyration, and intellectual disability [1-3]. Biallelic mutations in the WD repeat-containing protein 62 gene *WDR62* cause MCPH2 (MIM#604317), the second most common MCPH subtype [4]. So far, 25 mutations of the *WDR62* gene have been reported in 27 families or individual patients worldwide, most of them predicted to produce truncated proteins [4-12] (Figure 1, Table 1). Despite the classic MCPH definition of an isolated microcephaly at birth without severe architectonical abnormalities of the brain, patients with *WDR62* mut.ations can display a wide spectrum of cortical malformations including cortical thickening, polymicrogyria, simplified gyral pattern, pachygyria, schizencephaly, heterotopias, and corpus callosum abnormalities. Some patients also have evidence of lissencephaly, cerebellar hypoplasia, and hippocampal dysmorphy [4,7,12] (Table 1).

WDR62 is essential for mitotic spindle stabilization during mitosis and, as demonstrated in HeLa cells, it accumulates at the centrosome or the nucleus in a cell-cycle-dependent manner (from late prophase until

* Correspondence: wei.chen@mdc-berlin.de; angela.kaindl@charite.de
†Equal contributors
[3]Berlin Institute for Medical Systems Biology, Max Delbrück Center for Molecular Medicine, Robert-Rössle-Str. 10, Berlin 13092, Germany
[1]Institute of Cell Biology and Neurobiology, Charité University Medicine Berlin, Campus Virchow-Klinikum, Augustenburger Platz 1, Berlin 13353, Germany
Full list of author information is available at the end of the article

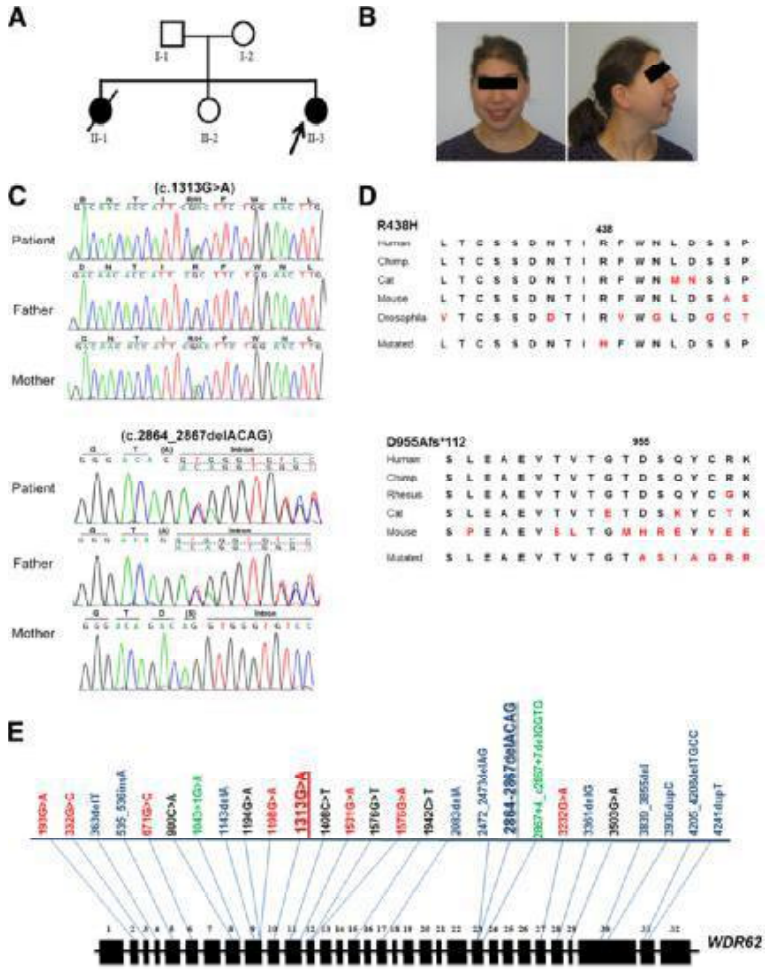

Figure 1 Phenotype and genotype of index patient. (A) Pedigree. **(B)** Facial phenotype of the patient. Note the sloping forehead, the convex facial profile, the full lips, and the small chin. The appearance of low-set and posteriorly rotated ears on the lateral picture is partly due to reclination of the head. See Additional file 1: Figure S1 for photo of sibling II:1.**(C)** Representative electropherogram traces confirm the heterozygous frameshift mutation c.2864-2867delACAG in the index patient and her father and the heterozygous missense mutation c.1313G>A in the index patient and her mother (NM_001083961.1 transcript reference sequence).**(D)** Sequence alignment of corresponding WDR62 protein regions depict the highly conserved amino acids affected by the maternally inherited missense mutation (p.R438H) and the position of the paternally inherited frameshift mutation (p.D955Afs*112): Human (Homo sapiens) UniProt O43379, Chimpanzee (Pan troglodytes) GenBank JAA38944.1, Rhesus monkey (Macaca mulatta) GenBank AFH29290.1, Cat (Felis catus) GenBank XP_003998018.1, Mouse (Mus musculus) GenBank NP_666298.3, Fruit fly (Drosophila melanogaster) Fly Base ID FBgn0031374. **(E)** Known *WDR62* gene mutations according to HGMD Professional 2012.4 and the present paper. Mutations types are color-coded, i.e. missense in red, frameshift in blue, nonsense in black, and splice site mutations in green. The positions of the mutations detected in the index patient are emphasized through bold letters (c.1313G>A also present in the index patient has been previously reported [4]).

metaphase-anaphase transition) [13]. It is enriched in proliferating precursors of the neuroepithelium in the developing murine brain [4,7] but at the same time it is also present in the cortical plate, a region where (postmitotic) neurons reside [12]. WDR62 knockdown in cortical progenitors by siRNA reduced their proliferative capacity, caused spindle orientation defects, decreased the integrity of centrosomes and displaced them from spindle poles, and delayed mitotic progression [13]. Despite considerable interest in MCPH as a model disorder for isolated and congenital microcephaly, the exact underlying pathomechanism remains to be established. Here, we report compound

Table 1 MCPH2 phenotypes and genotypes

Exon/Intron	Mutation	Alteration	Ethnicity	No. of patients	Mc* at birth	Mc* at follow up	Neurological phenotype					
							Intellectual disability	Speech delay	Motor delay	Epilepsy	Spasticity	Behavioral abnormalities[§]
Ex2	c.193G>A	p.V65M	Arab	7	yes	−5.3 to −9.8 SD	+ [a,b]	+	+	-	+	-
Ex3	c.332G>C	p.R111T	Pakistani	6[#]		−7 to −11 SD		+	-	+	-	-
Ex4	c.363delT	p.D112fs	Mexican	3[#]	−5 SD	10 m: -5.4 SD		+	+	+	-	-
Ex5	c.535_536insA	p.M179fs	Indian	2[#]		−4 to −9 SD	+ [a,c]	+	+	+	-	-
Ex6	c.671G>C	p.W224S		3[#]		2y: -3.5 SD	+ [c]	-	+	+	-	+
Ex8	c.900C>A	p.C300*	Indian	2[#]		−8 to −9 SD	+ [a]	+	+	+	-	-
In8	c.1043 + 1G>A	p.S348fs	Turkish	1	−2.6 SD	2 m: -4.0SD 5 m: -5.3SD		-	-	-	-	-
Ex9	c.1143delA	p.H381fs	Pakistani	2[#]		−6 to −7 SD		+	+	+	-	-
Ex9	c.1194G>A	p.W398*	Pakistani	4[#]		−6 to −8 SD						
Ex9	c.1198G>A	p.E400K	Hispanic	2[#]		9 m: -4 SD		+	+	+	-	+
Ex10	c.1313G>A	p.R438H	Pakistani	6	yes	−5 to −14 SD	+ [a,b]	+	-	-	-	-
Ex10/23	c.1313G>A / c.2864-2867delACAG	p.R438H / p.D955fs	German	1	- 2.3 SD		+ [a]	+	+	+	-	-
Ex11	c.1408C>T	p.Q470*		1	yes		+ [c]	-	-	+	-	-
Ex11	c.1531G>A	p.D511N	Pakistani	5	yes		+ [a,b]	+	-	-	-	-
Ex12	c.1576G>T	p.E526*		1		9 m: -4 SD	+ [b]	-	+	+	-	-
Ex12	c.1576G>A	p.E526K		1		3.5 y: -4 SD	+ [c]	+	-	-	-	-
Ex15	c.1942C>T	p.Q648*	Pakistani	2[#]	yes		+	-	-	-	-	-
Ex17/23	c.2083delA/c.2472_2473delAG	p.S696fs / p.Q918fs		2[#]	yes	8 y: -5 SD	+	+	+	+	+	-
In23	c.2867 + 4_c.2867 + 7delGGTG	p.S956fs	Turkish	1		1 y: -8.5SD		-	+	-	-	-
Ex27	c.3232G>A	p.A1078T	Pakistani	5	yes		+ [a,b]	+	-	-	-	-
Ex28	c.3361delG	p.A1121fs	Pakistani	2[#]		−10 to −11 SD						
Ex29	c.3503G>A	p.W1168*	Pakistani	3[#]		−9 to −11 SD		-	-	+	-	+
Ex30	c.3839_3855del	p.G1280fs	Turkish	1		3 m: - 3.5SD		+	+	+	-	-
Ex30	c.3936dupC	p.V1314fs	Caucasian Turkish Pakistani	5	−2.8 SD	−4 to −5 SD		+	+	-	-	-
Ex31	c.4205_4208delTGCC	p.V1402fs	Turkish	2[#]		−5 to - 6 SD	+ [c]	+	+	-	-	-
Ex31	c.4241dupT	p.L1414fs	Pakistani	9	yes		+ [a,b]	+		-	-	-

Table 1 MCPH2 phenotypes and genotypes *(Continued)*

Exon/Intron	Neuroradiological phenotype							Further phenotypes	Reference
	Simplified gyration	Cortical thickening	Corpus callosum abnormalities	Pachygyria	Polymicrogyria	Schizencephaly	Heterotopia		
Ex2	+	-	+	-	+	+	-	disproportionate sized face and ears compared to the skull	[4,12]
Ex3									[11]
Ex4	+	-	+	-	-	-	-		[12]
Ex5	-	+	-	+	-	-	-	low set and prominent ears	[6]
Ex6	-	+	+	+	-	-	-	micrognathia	[7]
Ex8	-	-	-	+	+	-	+		[6]
In8	-	-	+	-	-	-	+		[12]
Ex9	-	-	+	-	-	+	-		[9]
Ex9									[11]
Ex9	-	-	-	+	-	-	-		[5]
Ex10	+	-	-	-	-	-	-	disproportionate sized face and ears compared to the skull	[4,8]
Ex10/23	+	-	+	-	-	-	-	bilateral pes planus and hallux valgus	this study
Ex11	-	+	+	+	-	-	-	genu varum, cryptorchidism, arachnodactly	[7]
Ex11								disproportionate sized face and ears compared to the skull	[4,8]
Ex12	-	+	+	+	-	-	-		[7]
Ex12	-	+	+	+	-	-	-	prognathism	[7]
Ex15	+	-	-	-	-	-	-		[8]
Ex17/23	-	-	-	-	+	-	-		[10]
In23	-	-	+	-	-		+		[12]
Ex27								disproportionate sized face and ears compared to the skull	[4]
Ex28									[11]
Ex29									[11]
Ex30	-	-	+	-	-	-	-		[12]
Ex30	+	+	+	-	+	-	-	broad nasal bridge, widely set eyes	[4,8,12]
Ex31	-	+	+	+	-	-	-	micrognathia, bulbous nose	[7]
Ex31								disproportionate sized face and ears compared to the skull	[4]

Patients belong to one family.
* OFC in SDS, age in years (y) or months (m).
§ Behavioral abnormalities reported were hyperactivity and aggression.
a Mild, b Moderate, c Severe.

heterozygous mutations (one being novel) of the *WDR62* gene in a female MCPH2 patient of German descent and describe her clinical and cellular phenotype. We thereby provide evidence that the MCPH2 phenotype, at least partly, is due to centrosome/spindle organization defects.

Human subjects and methods

Patients

Informed consent was obtained from the parents of the index patient for the publication of clinical and radiological data, cytogenetic and molecular genetic analyses, and lymphoblastoid cell line (LCL) studies. DNA was extracted from EDTA blood samples using standard techniques [14]. Approval to conduct the present study was obtained from the local ethics committee of the Charité (approval no. EA1/212/08). The index patient is a 24-year-old microcephalic patient of German descent with typical facial features of MCPH including sloping forehead and severe intellectual delay. She also had astatic seizures, which could be controlled by antiepileptic treatment. Cranial imaging studies revealed small frontal lobes, hypoplasia of the corpus callosum, simplified hippocampal gyration, widened lateral sulci, and cerebellar hypoplasia with an enlarged cisterna magna. Her blood count was normal, and there was no evidence of any malignant disease. The detailed phenotype is delineated below.

Karyogram and array-CGH analysis

Standard karyotyping revealed a normal result (46,XX). Array-CGH was performed on the NimbleGen Whole Genome Tiling 135 k CGX-12 platform and revealed a 1.66 Mb duplication of the short arm of chromosome 2, arr[hg19] 2p12(82,018,317-83,674,828) × 3, that was inherited from the healthy mother and comprised a pseudogene (LOC1720) only.

Exome sequencing

All three family members (parents, index patient) were subjected to exome sequencing. Genomic DNA was isolated from blood samples using standard methods. Five micrograms of genomic DNA were enriched using the Agilent Human All Exon V3 kit (Agilent Technologies, Santa Clara, CA, USA) following the manufacturer's protocol. Whole-exome libraries were sequenced on an Illumina HiSeq 2000 system for 1 × 101 cycles following the manufacturer's instructions (Illumina, San Diego, CA, USA). All raw sequencing reads were mapped onto UCSC hg19 [15] using Burrows-Wheeler Aligner (BWA) 0.5.9-r169 [16] and converted to BAM file format using SAMtools 0.1.18 [17]. Initial mappings were post-processed using the Genome Analysis Toolkit (GATK) 1.6 [18] following their 'best practices V3′ (http://www.broadinstitute.org/gatk/guide/best-practices). In brief, reads were realigned around sites of known insertion-deletion polymorphisms (INDELs). Then, likely polymerase chain reaction PCR duplicates were detected using Picard 1.48 [17]. Finally, raw base quality scores were empirically recalibrated. Single nucleotide polymorphisms (SNPs) and INDELs were identified using the UnifiedGenotyper from GATK. Variants were classified as novel or known variants according to the SNP database (dbSNP) 135 [19]. Functional consequences of each variant were annotated using snpEff 2.0.5d20 [20] for UCSC hg19 RefSeq genes and ENSEMBL 65 human gene models [15,21]. The potential deleterious effect was evaluated using Polymorphism Phenotyping v2 (PolyPhen 2, [22]), sorting intolerant from tolerant (SIFT, [23]), PhyloP [24], MutationTaster [25], Genomic Evolutionary Rate Profiling (GERP++, [26]), Likelihood Ratio Test (LRT, [27]), and the OMIM database (http://www.ncbi.nlm.nih.gov/omim/), if available. Variants were filtered for the two most likely inheritance patterns, autosomal-dominant and autosomal-recessive (either compound heterozygous or homozygous).

Sanger sequencing

The compound heterozygous mutations identified through exome sequencing were verified through Sanger sequencing using the primers: F1 5′-gtca tagtgctgtcattgagtcatc-3′, R1 5′ gagccaactggcaaagaatc-3′, F2 5′-gtgccacacctcttcctcatc-3′, and R2 5′-cacctggaaccagggaacta-3′. The reference sequence NM_001083961 of *WDR62* was used.

Establishment of Ebstein-Barr virus-transformed lymphocytes and culture

Ebstein-Barr virus-transformed lymphocytes (LCLs) were established according to the protocol published by H. Neitzel 1986 [28]. LCLs were cultured in RPMI 1640 with L-Glutamine (Invitrogen, Darmstadt, Germany) supplemented with 20% v/v fetal bovine serum (Invitrogen) and 1% v/v penicillin-streptomycin (Sigma-Aldrich, Taufkirchen, Germany) [29]. For this study, we used LCLs from the patient and from two controls.

Immunocytology

For fixation, cells were cultured on poly-L-lysine (Sigma-Aldrich) coated coverslips for 30 min at standard conditions and subsequently incubated in paraformaldehyde (PFA) 4% for 10 min. Coverslips were rinsed with phosphate buffered saline (PBS 1x) and further incubated at room temperature in staining buffer (0.2% gelatin, 0.25% Triton X-100 in PBS 1x) for 20 min. Blocking was achieved by incubation in 10% donkey normal serum (DNS) in staining buffer for 30 min. Coverslips were incubated overnight at 4°C with primary antibodies in the staining buffer containing 10% DNS followed by an incubation with the corresponding secondary antibodies for 2 h at RT. Nuclei were labeled with 4′,6-diamidino-2-phenylindole (DAPI, 1:1,000, Sigma-Aldrich). Fluorescently labeled

cells were analyzed and imaged by a fluorescent Olympus BX51 microscope with the software Magnafire 2.1B (version 2001; Olympus, Hamburg, Germany), and all images were processed using Adobe Photoshop. This procedure has been previously described [29].

The anti-WDR62 antibody (rabbit polyclonal anti-WDR62, Bethyl laboratories, A301-560A, 1:500) utilized in this study recognizes amino acids between residue 900 and 950 of human WD repeat domain 62 (accession no. NP_775907.4, GeneID 284403, UniProt ID: O43379). Further primary antibodies were as follows: mouse anti-γ-tubulin (T6557, Sigma-Aldrich, 1:500), mouse anti- α-tubulin (T9026, Sigma-Aldrich; 1:1,500), and rabbit anti-CDK5RAP2 (HPA035820, Sigma-Aldrich, 1:200). The immunoreaction specificity was analyzed in control specimen incubated only in the secondary antibodies.

Protein extraction procedure and Western blot

Protein extracts for Western blots were isolated from LCLs by homogenization in radio-immunoprecipitation assay (RIPA) buffer containing 1 mM phenylmethylsulfonyl fluoride (PMSF; Sigma-Aldrich) and 1 protease inhibitor cocktail tablet per 10 ml RIPA buffer (Complete Mini; Roche Diagnostics, Mannheim, Germany), 15 min incubation on ice, followed by ultrasonication and centrifugation at 4°C for 10 min at 3,000 g and for 20 min at 16,000 g. Protein concentrations were determined using a bicinchoninic acid (BCA) based assay, according to the instructions of the manufacturer (BCA Protein Assay Kit; Pierce Biotechnology, Rockford, IL, USA). Protein extracts (30 μg per sample) were denaturated in Laemmli sample loading buffer at 95°C for 5 min, separated by sodium dodecyl sulphate polyacrylamide gel electrophoresis (SDS-PAGE), and electrophoretically transferred onto nitrocellulose membrane (Bio-Rad, Munich, Germany) using Bio-Rad wet transfer system (Bio-Rad, Munich, Germany). This procedure has been previously described [29].

The membranes were incubated for 1 h at room temperature in blocking buffer Tris-Buffered Saline Tween-20 (TBS-T) 1× with 5% bovine serum albumin (BSA), rinsed three times with TBS-T (1×) for 8 min each at RT on a shaker, and then incubated overnight at 4°C with rabbit anti-WDR62 (1:500, A301-560A, Bethyl laboratories) or mouse anti-actin (1:10,000, MAB1501, Millipore) antibodies in blocking solution. After incubation with the corresponding secondary antibodies donkey anti-rabbit (1:2,000; Amersham Biosciences, Freiburg, Germany) and goat anti-mouse (1:10,000; Dako, Hamburg, Germany) the immunoreactive proteins were visualized using a technique based on a chemiluminescent reaction. The gel pictures were obtained using photographic films (Amersham Hyperfilm ECL, GE Healthcare, UK). Western blot experiments were run in triplicate.

Cell cycle analysis

Cell cycle analysis was performed using the 5-bromo-2′-deoxyuridine (BrdU)-Hoechst 33258 method [30]. The principle of that assay is based on the incorporation of the halogenated base analog during DNA replication. The assay makes use of the fact that BrdU-substituted chromatin quenches the fluorescence of the dye Hoechst 33258. This method differentiates not only between cycling and noncycling cells in a given culture but also recognizes the distribution of the cycling cells in as many as four consecutive cycles. For flow cytometry mononuclear cells were Ficoll-isolated from heparinized blood samples. Cultures were set up in RPMI 1640 medium with GlutaMAX (Gibco Life Technologies), supplemented with 15% fetal bovine serum (FBS, PAN Biotech). Duplicate cultures were either left untreated, or irradiated with 1.5 Gy from a linear accelerator or continuously exposed to 10 ng/ml mitomycin C (Medac). To all of the cultures BrdU (Sigma-Aldrich) was added at a final concentration of 10^{-4} M [31]. Lymphocyte growth activation was induced by phytohaemagglutinin (PHA HA16, Remel Europe, Dartford, UK). The cells were harvested after 72 h. Following staining with Hoechst 33258 (1.2 μg/ml; Molecular Probes) for a minimum of 15 min in buffer containing 154 mM sodium chloride (NaCl), 0.1 M TRIS pH 7.4, 1 mM calcium chloride ($CaCl_2$), 0.5 mM magnesium chloride ($MgCl_2$), 0.2% BSA, and 0.1% nonyl phenoxypolyethoxylethanol (NP40) in distilled water in the dark, ethidium bromide (EB, 1.5 μg/ml, Molecular Probes) was added for another minimum of 15 min. Bivariate flow histograms were recorded on a triple-laser equipped LSRII flow cytometer (Becton Dickinson) using UV excitation of Hoechst 33258 and 488-nm excitation of EB. The resulting cell cycle distributions reflecting cellular DNA content were quantified using the MPLUS AV software package (Phoenix Flow Systems, San Diego, CA, USA).

Analysis of chromosome condensation

Whole-blood cultures were prepared using RPMI 1640 medium with GlutaMAX (Gibco Life Technologies) supplemented with 15% fetal bovine serum (FBS, PAN Biotech). Lymphocytes were stimulated with PHA (Remel Europe). The cultures were terminated after 72 h following addition of 8 μl/ml Colcemid solution (10 μg/ml; PAA) for the final 45 min. Metaphase preparations were made by hypotonic incubation of the cell pellets (0.075 M KCl for 10 min at 37°C) and fixation of the nuclei in ice-cold methanol/concentrated acetic acid 3:1. Slides were stained with 5% Giemsa solution for 5 min without applying banding techniques. A total 1,000 nuclei per sample were scored by visual counts, and the proportion of metaphases and of nuclei

with prophase-like morphology (prophase-like cells, PLCs, defined as nucleus-shaped structures with condensed chromosomes) were determined.

Results

Phenotype of the patient with MCPH2

The index patient is the third child of non-consanguineous healthy parents of German descent (Figure 1A). Microcephaly was diagnosed by ultrasound in the 30th week of gestation. Pregnancy and delivery were uneventful. Birth weight, length, and head circumference at term were 3600 g (0.6 SDS, 50-75th centile), 55 cm (1.6 SDS, 95th centile), and 31 cm (–2.3 SDS; 1 cm below 3rd centile), respectively. The head circumference of her parents was normal. Postnatal cranial ultrasound revealed small frontal lobes, hypoplasia of the corpus callosum, simplified hippocampal gyration, widened lateral sulci, and cerebellar hypoplasia with an enlarged cisterna magna. Further imaging studies were refused by the parents. These findings are in line with cortical malformations previously associated with *WDR62* mutations, and are expected to have impact on cognitive, language, motor, and behavioral functions of the patient. Language development of the girl was severely delayed (first words at the age of 4 years) while the delay in motor development (unaided walking at the age of 2 years) was moderate [32]. At the age of 16 years, the patient developed astatic seizures that were controlled by carbamazepine treatment. At the age of 24 years, the patient was distinctively microcephalic (50 cm, 3 cm below 3rd centile, -3.3 SDS) while her body length of 164 cm (25th-50th centile) and weight of 54 kg (25th-50th centile) were normal. She could phrase sentences of up to three to four words and recognized letters but was not able to perform any abstract intellectual task such as reading, writing or simple calculation. She also had difficulties in performing complex motor tasks such as riding a bicycle. Neurological examination did not reveal any further abnormality. Spatial orientation, vision and hearing were normal. Facial features included convex facial profile, sloping forehead, marginally low-set and posteriorly rotated ears, small chin, and full lips. In spite of the small cranium, palpebral fissures were horizontal. On physical examination bilateral pes planus and hallux valgus were found. Blood count was normal, and there was no evidence of any malignancy or further organ malformation/malfunction (Table 1). Results of genetic analyses (karyogram and array-CGH) were normal.

The patient's sister who was born earlier also had microcephaly and intellectual disability (Additional file 1: Figure S1). She died of a Wilms tumor at the age of 5 years (head circumference at birth 31 cm, -2.3 SDS, 1 cm below 3rd centile; head circumference at 2 years-of-age 41 cm, -4.4 SDS, 5 cm below 3rd centile). A left-sided spastic hemiparesis had been noticed. Brain computed tomography at one month of age had revealed a plump right ventricle, wide arachnoidal spaces, and parieto-occipital hypodensity. In the second year of life, an electroencephalogram (EEG) had revealed signal depression on the right hemisphere and epileptic activity on the left hemisphere. Results of genetic analyses (Karyogram and array-CGH) had been normal.

Novel *WDR62* mutation

Both parents and the index patient were subjected to whole exome sequencing. In total, we obtained 92–100 million single-end 101 bp reads per sample, of which 97.6 - 98.0% could be mapped onto the human genome. After removing duplicated reads, which were possibly derived from PCR artifacts, 29–31 million unique reads were mapped to the targeted protein coding regions, resulting in an average of 59.0 - 62.8× coverage within the targeted coding region. Using the Genome Analysis Toolkit (GATK) we detected 19,381 - 19,656 SNPs and INDELs in the exome of each family member, of which 98.3 - 98.4% were known variants deposited in dbSNP 135. Given the pedigree, we searched for autosomal-dominant, autosomal-recessive homozygous, compound heterozygous, and de novo mutations.

Through this exome sequencing approach, we identified two compound heterozygous mutations of the *WDR62* gene in the index patient: (i) a missense mutation (c.1313G>A) in exon 10 that was inherited from the mother and resulted in a substitution of arginine by histidine (R438H); (ii) a frameshift mutation with deletion of 4 nucleotides (c.2864-2867delACAG) in exon 23 that was inherited from the father and resulted in a stop codon of the new reading frame 112 aa downstream of the deletion (D955Afs*112). Both mutations were confirmed by Sanger sequencing (Figure 1C). The *WDR62* gene encodes for a WD-repeat containing protein and has been associated with autosomal recessive primary microcephaly 2 (MCPH2, MIM*613583), matching the phenotype of the patient. c.1313G>A has been described previously in seven homozygous MCPH2 patients and is predicted to be deleterious [4], while c.2864-2867delACAG is a novel mutation and could result in nonsense-mediated decay. Indeed, WDR62 protein levels were reduced or below detection level in EBV-transformed lymphocytes of the index patient, when assessed via western blot and immunocytology, respectively (Figure 2). A survey of the types and locations of reported *WDR62* mutations is schematically depicted in (Figure 1E). Independent of the two mutations, the patient also carried a 1.66 Mb duplication at 2p12 (chr2: 82.0-83.7 Mb, hg 19). The duplication comprising the pseudogene LOC1720 was inherited from her healthy mother and thus was not considered as disease-causing.

Cellular phenotype of the patient with *WDR62* gene mutations

We assessed the phenotypic consequences of the biallelic WDR62 mutation in mutant lymphoblastoid cells (LCLs) of

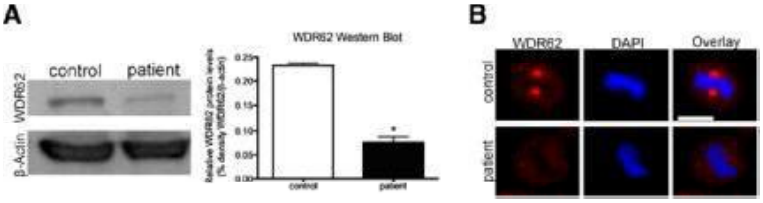

Figure 2 Representation of WDR62 protein in immortalized lymphocytes. (A) Protein extracts were analyzed with an anti-WDR62 antibody that recognizes amino acids 900–950. Beta-actin was used as a control for equal protein loading. Signals were visualized with enhanced chemiluminescence. WDR62 protein levels in immortalized lymphocytes from the patient were significantly lower than in control cells (n = 3, p 0.0104, Student's t-test). **(B)** Centrosomal WDR62 levels were below detection levels when assessed through immunocytology in patient cells using the same antibody.

the MCPH2 patient. Cell cycle analysis of LCLs revealed normal results when compared to control specimen, and the patient's LCLs did not prove sensitive to ionizing radiation or mitomycin C exposure (data not shown). After colcemid arrest of otherwise untreated cultures, a vast majority of mitotic cells in the patient's LCLs showed typical metaphase morphology (Figure 3A) in contrast to MCPH1 cells whose characteristic feature is an increased number of nuclei with prophase-like chromosome (PLC) morphology (Figure 3B). Quantitative analysis revealed a regular PLC rate of the MCPH2 LCLs, comparable to normal controls and opposed to the increased rates in MCPH1 LCLs (Table 2).

We determined the subcellular distribution of WDR62 in LCLs of patient and controls by immunocytology. In control cells, WDR62 localized to the centrosomes throughout the mitotic progression with reduced signal intensities in anaphase and telophase (Figure 4A). Centrosomal WDR62 signals were relatively reduced during interphase and then increased throughout mitosis until anaphase, when signals dropped to interphase levels. In anaphase telophase, WDR62 also appeared to be present in the division plane/cytoplasm. Furthermore, WDR62 was assigned to the midbody during anaphase as shown by co-localization with γ-tubulin (Figure 4A) for which midbody localization has been reported [33]. In *WDR62* mutant cells the co-localization of WDR62 and γ-tubulin at the midbody appeared to be abrogated to a large extent similar to the reduced levels at the centrosomes (Figure 4B). In *WDR62* mutant LCLs, WDR62 expression was not detectable when assessed by immunocytology using an antibody against a WDR62 epitope at aa 900 to 950 (Figure 2B, Figure 4B). Western blot using the same antibody revealed a single band of normal size but severely reduced quantity, suggesting that the allele with the frameshift deletion was not expressed (otherwise a second band would be visible) while the allele with the missense mutation had residual expression and/or enhanced degradation and possibly a more dispersed distribution making its immunocytological detection impossible (Figure 2A).

Since deficiency or dysfunction of WDR62 reduce human brain size and impact on cell proliferation, we examined the integrity of the centrosome and the mitotic spindle apparatus in cells of the index patient and of the controls. In control LCLs, WDR62 colocalized with the centrosomal protein γ-tubulin throughout the cell cycle (Figure 4A). In patient cells, WDR62 was below the detection limit. Here, we observed a more dispersed γ-tubulin staining around the centrosome rather than a complete loss of γ-tubulin from the centrosome (72.3% versus 9.8% of 100 counted metaphase lymphoblastoid cells of index patient versus controls; Student's t-test, $p < 0.001$) (Figure 4B, C). Similarly, the levels of centrosomally located CDK5RAP2 were strongly reduced in *WDR62* mutant LCLs (Figure 4D, Figure 5A,B).

We further examined the changes in mitotic spindle organization. In controls, the spindle apparatus had a regular bipolar form of appearance from prometaphase to telophase (Figure 5A). Spindle defects were observed in patient cells with an increase of abnormal misdirected spindles with broad and unfocused poles of microtubules (Figure 5B). Quantification of the metaphase cell population indicated that more than half of WDR62-depleted cells exhibited such abnormal bipolar spindles (87.6% versus 10.2% of 115 counted metaphase LCLs of index patient versus controls; Student's t-test, $p < 0.0001$) (Figure 5C). Mutant cells also showed displaced centrosomes detected by co-staining with both CDK5RAP2 and alpha-tubulin (Figure 4D). In addition, the spindle pole distance was significantly increased in mutant cells compared to controls (2.46 μm versus 2.1 μm of 115 counted metaphase lymphoblastoid cells of index patient versus controls; Student's t-test, $p < 0.0001$) (Figure 5C). Given the importance of assembly of bipolar mitotic spindles for accurate chromosome segregation, we investigated the alignment of chromosomes in patient cells. We noted the presence of lagging chromosomes in some lymphoblastoid cells from the patient compared to the controls (Figure 6).

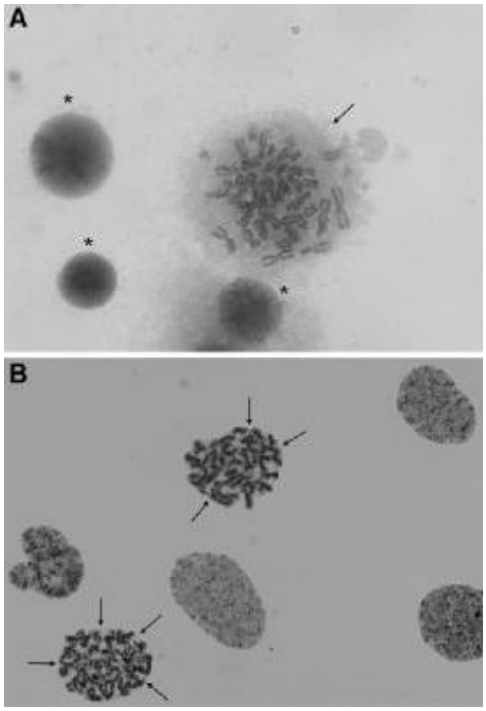

Figure 3 Absence of a prophase-like chromosome phenotype in MCPH2 deficiency. (A) Normal metaphase morphology (arrow) of a cultured lymphoblast in a cell line from the MCPH2 patient after induced mitosic arrest by colcemid. The chromosomes are condensed while the delimitation of the metaphase is irregularly shaped suggesting that there is no more nuclear membrane after its disintegration in prophase. Three other nuclei are stained rather homogeneously, typical of uncondensed chromatin in interphase nuclei (asterisks). **(B)** An MCPH1 lymphoblastoid cell line treated identically shows nuclei with typical prophase-like chromosome (PLC) morphology. Virtually all of the six nuclei reveal a meandering striped or banded chromatin structure characteristic of beginning chromosome condensation (best seen in the two marked nuclei). Despite prometaphase stage, they present with rounded delimitations (arrows) suggesting that they are bounded by a persisting nuclear membrane, a phenomenon that is designated as premature chromosome condensation (PCC). Giemsa stain.

Table 2 Rate of nuclei with prophase-like chromosome (PLC) morphology

Designation	Mean [%]	PLC Rate SD [%]	Range [%]	n
MCPH2 Patient	1.36	± 0.5	0.79-2.33	7
Normal Controls	1.17	± 0.85	0-2.09	8
MCPH1 Patients	9.07	± 4.02	5.96-13.77	3

N: number of independent experiments in the reported MCPH2 patient or number of individuals with single experiments in normal and MCPH1 controls.

Discussion

Phenotype and genotype

We report compound heterozygous *WDR62* mutations in a German girl with primary microcephaly: (i) a missense mutation with single nucleotide transition c.1313G>A in exon 10 resulting in the substitution of arginine by histidine (R438H) which has been reported previously in homozygous patients (4), and (ii) a novel frameshift deletion of four nucleotides c.2864-2867delACAG in exon 23 that resulted in a stop codon of the new reading frame 112 aa downstream of the deletion (p.D955Afs*112) (Figure 1). The index patient had congenital microcephaly, intellectual disability, speech deficit, and epilepsy. Apart from typical facial features of MCPH including a sloping forehead, she had only minor dysmorphic features (convex profile with small chin), and her height and weight were normal. There was no further neurological deficit and her sensorial functions were normal. The postnatal cranial ultrasound of the patient revealed small frontal lobes, simplified hippocampal gyration, and hypoplasia of both the corpus callosum and the cerebellum. Despite the classical definition of MCPH as a severe congenital microcephaly lacking morphological abnormalities of the brain, it is now acknowledged that particularly MCPH patients with *WDR62* mutations may have a wide spectrum of brain malformations in addition to microcephaly including pachygyria, thickened cortex, polymicrogyria, schizencephaly, corpus callosum, and hippocampal abnormalities as well as cerebellar hypoplasia [4,7,12], in line with the phenotype of the index patient (Table 1).

Although cancer has not been described so far in patients with MCPH2, individual patients with other MCPH subtypes and leukemia have been reported [2,34]. Moreover, mouse models of MCPH3 and MCPH5 displayed an increased tumor risk and/or blood abnormalities (anemia, leucopenia) [35,36]. It is likely that the deceased sister of the index patient who also had severe microcephaly at birth and intellectual disability, carried the p.R438H / p.D955Afs*112 mutations of the *WDR62* gene. (Unfortunately, her DNA was not available for genetic testing anymore.) The diagnosis of a Wilms tumor in association with a putative *WDR62* mutation raises concerns regarding a potentially increased cancer risk in MCPH2 patients also. In addition, especially in patients with MCPH1 and MCPH5, early puberty, renal agenesis, and multicystic kidneys have been described. As this point warrants further investigation in patients, we investigated the clinical phenotype of our patient in detail but found no evidence of blood abnormalities, organ involvement, or malignancy.

Effect of *WDR62* mutations

Most previously reported *WDR62* mutations have been proposed to lead to loss of WDR62 function

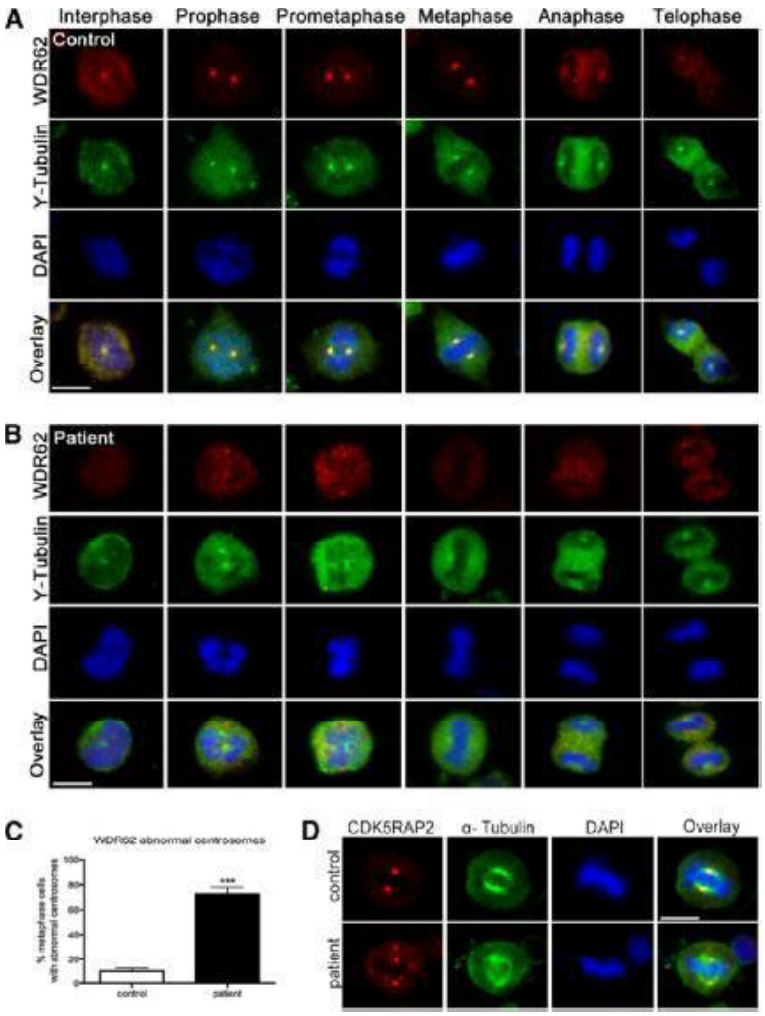

Figure 4 WDR62 in immortalized lymphocytes and dispersion of centrosomal proteins γ-tubulin and CDK5RAP2 in *WDR62* mutant patients cells. Subcellular localization of WDR62 (red) and γ-tubulin (green) throughout the cell cycle in immortalized lymphocytes of **(A)** controls and **(B)** the MCPH2 patient. In controls, WDR62 colocalized with γ-tubulin and was present on the centrosome with high levels throughout mitosis until anaphase and telophase, thereafter the signal intensity dropped to interphase levels. Gamma-tubulin immunostaining shows distinct centrosomes in controls whereas in patient cells the γ-tubulin-marked centrosomes appear broad and dispersed. **(C)** Quantification results of abnormal centrosomes with a dispersed γ-tubulin staining around the centrosome (n = 100 metaphase lymphoblastoid cells, p = 0.0006, Student's t-test). **(D)** Abnormal localization of centrosomal protein CDK5RAP2 (red) in *WDR62* mutant patient immortalized lymphocytes (see also Figure 5). Cells were stained for WDR62, for the centrosome marker CDK5RAP2, and for α-tubulin as a microtubuli marker. DNA was stained with DAPI (blue).

(Figure 1, Table 1). The mutation of the paternal allele (p.D955Afs*112) in the present patient leads to a stop codon in the novel reading frame. Since the Western blot revealed only a single band of normal size we assume that this allele's RNA is subject to nonsense-mediated decay and that its protein product is not expressed (Figure 2A). The previously reported missense mutation present also in our index patient (p.R438H) alters evolutionarily highly conserved amino acids of WDR62 [4].

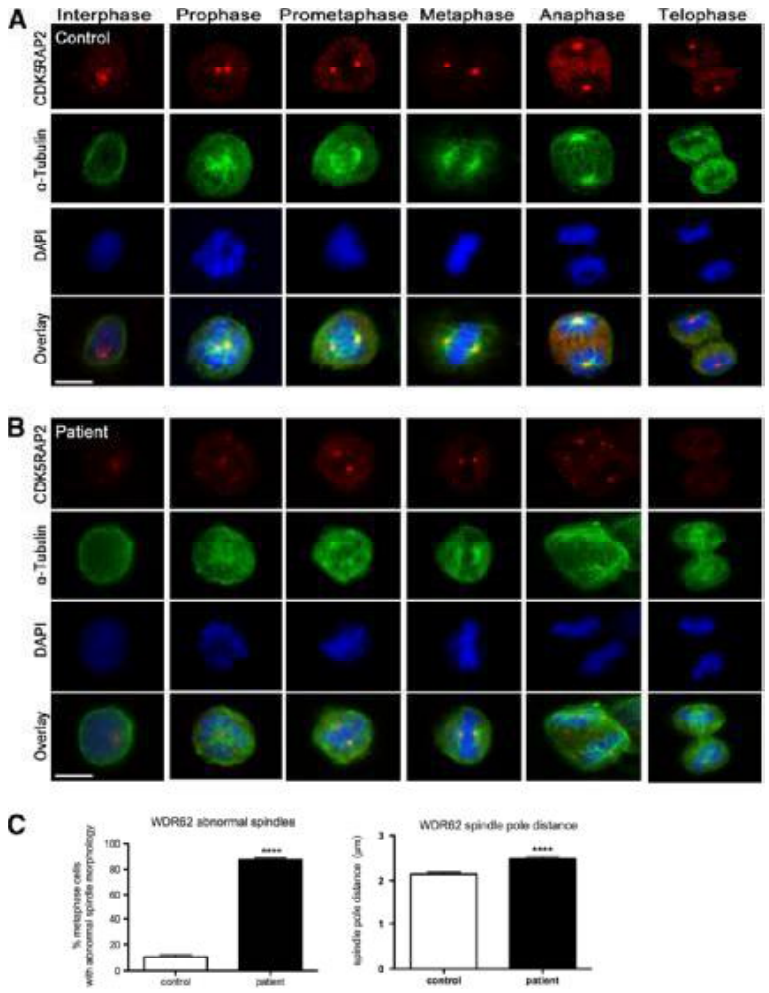

Figure 5 Spindle defects in *WDR62* mutant patient cells. Subcellular localization of CDK5RAP2 and α-tubulin throughout the cell cycle in immortalized lymphocytes of **(A)** control and **(B)** MCPH2 patient. While the spindle apparatus has a regular bipolar form of appearance from prometaphase to telophase in controls, patient cells show abnormal spindle formation with an increase of abnormal misdirected spindles and broad, unfocused microtubules poles. CDK5RAP2 signals are weaker in patient's cells than in controls. Cells were stained for CDK5RAP2 (red), for α-tubulin (green), and for DNA using DAPI (blue). **(C)** Quantification results of abnormal spindles and spindle pole distance (n = 115 metaphase lymphoblastoid cells, $p < 0.0001$, Student's t-test).

The human MCPH phenotype is considered, based on results from *in vivo* and *in vitro* studies, to result from a premature shift from symmetric to asymmetric neural progenitor-cell divisions (with a subsequent depletion of the progenitor pool) and from a reduction in cell survival [37,38]. A central molecular mechanism for microcephaly in MCPH2 may be a deficiency or dysfunction of WDR62 at the spindle pole of dividing cells due to processes such as non-expression, loss of essential spindle targeting domains, misfolding or rapid degradation of the mutant protein [39]. For WDR62 it has been recently demonstrated that siRNA downregulation in murine neural progenitors through *in utero* electroporation induces early cell cycle exit and a reduced proliferative capacity. Downregulation by siRNA of *WDR62* in murine neural progenitors causes early cell cycle exit and reduced

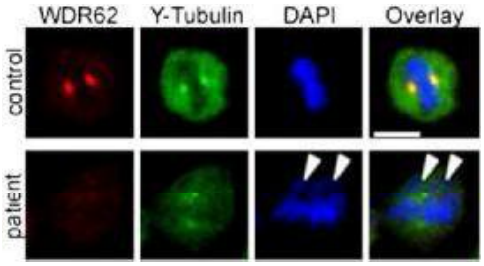

Figure 6 Lagging chromosomes in mutant *WDR62* lymphocytes. Some chromosomes in patient cells showed lagging defects in metaphase (indicated by arrows).

proliferative capacity [13]. Moreover, WDR62 downregulation in tumor cells (HeLa) was associated with spindle orientation defects, decreased centrosome integrity and displacement from the spindle pole as well as delayed mitotic progression [13].

Cellular phenotype

To study the effect of the reported compound heterozygous *WDR62* gene mutations on centrosome and spindle integrity in the present index patient, we analyzed the intracellular localization of WDR62 as well as centrosome and spindle morphology of EBV-transformed lymphocytes (LCLs) from the patient and from controls. WDR62 localized to the centrosomes of control LCLs at all phases of the cell cycle in a cycle-dependent manner, with low centrosomal WDR62 levels in anaphase and telophase. In interphase, WDR62 was also only weakly associated with the γ-tubulin-labeled centrosome; moreover, WDR62 expression appeared to be cytosolic (Figure 4). These findings are in line with previous reports of WDR62 localization in human tumor cells (HeLa, HEK293, A549, HepG2), human non-tumor cells including B-lymphocytes as well as mouse cerebral cortex neuroepithelial cells at E13. Here WDR62 was reported to assume both nuclear and cytosolic distribution in interphase by some authors [4,6,12,13], while accumulating strongly at the spindle poles during mitosis [4,6,12,13] with no obvious centrosomal association of WDR62 during anaphase and telophase [13]. We also detected WDR62 protein accumulation in the division plane (midbody) in lymphoblastoid cell lines, a region of bipolar microtubuli array that arranges between separating sister chromatids during anaphase [40]. Contrary to our results, no protein accumulation was detected at the midbody during cytokinesis in previous localization reports performed in other cell lines (HeLa, HEK293, A549, HepG2) [4,6,12]. Further studies are needed to address the association of WDR62 with the midbody. In one report, the mitotic WDR62 distribution was evaluated by its colocalization with CDK5RAP2, a key centrosomal protein known to cause MCPH3 when disrupted. WDR62 and CDK5RAP2 colocalized to the centrosome throughout the cell cycle. However, during prometaphase and metaphase, WDR62 surrounded rather than strictly colocalized with CDK5RAP2 at the centrosome [7].

WDR62 protein levels were low (western blot) or non-detectable (immunocytology) in MCPH2 patient cells. As indicated above, this finding may result from nonsense-mediated decay of the transcript with the frameshift deletion and dispersion and/or instability of the protein with the missense mutation (Figures 2 and 4). In contrast to siRNA studies on *WDR62* downregulation, we detected neither a disorder of cell cycle progression in peripheral lymphocytes of the patient nor increased chromosomal breakage rates of her LCLs when compared to controls. We could, however, detect a failure of the centrosomal proteins γ-tubulin and CDK5RAP2 to localize properly at the centrosome in patient cells indicating an abnormal centrosome integrity (Figures 4 and 5). In addition, spindles were disorganized in patient cells with displaced centrosomes, increased spindle pole distance, and lagging chromosomes (Figures 5 and 6). These results are in line with those of Bogoyevitch et al. 2012 [13] who observed abnormal metaphase spindles characterized by a displacement of centrosomes from the spindle pole and a significant increase of spindle length. Thus, the recent appreciation of a relationship between proper centrosome attachment to the spindle pole and spindle length determination [41,42] is reinforced. Since spindle function is important for correct chromosome alignment at the spindle equator and this again is necessary for accurate segregation of chromosomes during cell division into two daughter cells [43], we investigated these processes. Our observation of disturbed metaphase chromosome alignment and of lagging chromosomes in some lymphoblastoid cells from the patient is in line with previous reports demonstrating an increase in the proportion of unaligned chromosomal DNA during metaphase in HeLa cells following *WDR62* siRNA [13]. This is consistent with delayed mitotic progression and disrupted centrosome/bipolar spindle organization [13], emphasizing the importance of regulated assembly of the mitotic spindle apparatus that impact the forces acting on chromosomes.

Conclusion

Tight and timely control of cell division largely determines brain size during embryonic development [44]. Our results, although generated in human patient lymphocytes and not human neural progenitors, suggest that spindle defects and a disruption of centrosome integrity could play a role in the development of microcephaly in MCPH2. In fact, our results on lymphoblastoid cells from a MCPH2 patient are in line with those detected in two MCPH5

patients [29]. Future studies on neuronal stem cells derived from iPS cells of MCPH patients may provide further confirmation.

Additional file

Additional file 1: Figure S1. Picture of sibling. Picture of the patient's sister (II:1, see pedigree in Figure 1A) at the age of 1.5 years. She also had microcephaly and intellectual disability, and she died of a Wilms tumor at the age of 5 years.

Abbreviations

Array-CGH: Comparative genomic hybridization; BCA: Bicinchoninic acid; BrdU: 5-bromo-2-deoxyuridine; BSA: Bovine serum albumin; BWA: Burrows-wheeler aligner; $CaCl_2$: Calcium chloride; CDK5RAP2: CDK5 regulatory subunit associated protein 2; DAPI: 4′,6-diamidino-2-phenylindole; dbSNP: Single nucleotide polymorphism database; DNS: Donkey normal serum; EB: Ethidium bromide; EBV: Epstein–Barr virus; EDTA: Ethylene diamine tetraacetic acid; EEG: Electroencephalogram; FBS: Fetal bovine serum; GATK: Genome analysis toolkit; GERP++: Genomic evolutionary rate profiling; INDELs: Insertion-deletion polymorphisms; LCLs: Lymphoblastoid cell lines; LRT: Likelihood ratio test; MCPH: Autosomal recessive primary microcephaly; $MgCl_2$: Magnesium chloride; NaCl: Sodium chloride; NP40: Nonyl phenoxypolyethoxylethanol; PBS: Phosphate buffered saline; PCR: Polymerase chain reaction; PFA: Paraformaldehyde; PHA: Phytohaemagglutinin; PLCs: Prophase-like cells; PMSF: Phenylmethylsulfonyl fluoride; PolyPhen 2: Polymorphism phenotyping v2; RIPA: Radio-immunoprecipitation assay; SDS-PAGE: Sodium dodecyl sulphate polyacrylamide gel electrophoresis; SIFT: Sorting intolerant from tolerant; siRNA: Small interfering RNA; SNPs: Single nucleotide polymorphisms; TBS-T: Tris-buffered saline tween-20; WDR62: WD repeat-containing protein 62.

Competing interests

The authors declare no competing interest in the preparation or publication of the data in this manuscript.

Authors' contributions

AMK, KO, and WC were responsible for the project conception. AMK and HGF wrote the manuscript. KO and AMK attended the patients and provided clinical data. AH established the LCLs culture. HGF, ER, and NK performed the lymphocyte analysis, performed Sanger sequencing, and generated figures. SF and WC performed exome sequencing and data analysis. TS assessed PCL rates. DS and TS performed cell cycle and chromosome breakage analysis and revised the manuscript. All authors read and approved the final manuscript.

Acknowledgements

The authors thank Katrin Köhler, Lina Issa-Jahns, Jessica Fassbender, Mirjam Feldkamp, and Claudia Langnick for technical assistance and discussions.

Funding

This work was supported by the German Research Foundation (SFB665), the Sonnenfeld Stiftung, and the Berliner Krebsgesellschaft e.V. SF and WC are supported by the Helmholtz Association, the German Ministry of Education and Research (BMBF), and the Senate of Berlin by funds to the Berlin Institute for Medical Systems Biology (BIMSB).

Author details

[1]Institute of Cell Biology and Neurobiology, Charité University Medicine Berlin, Campus Virchow-Klinikum, Augustenburger Platz 1, Berlin 13353, Germany. [2]Department of Pediatric Neurology, Charité University Medicine Berlin, Berlin, Germany. [3]Berlin Institute for Medical Systems Biology, Max Delbrück Center for Molecular Medicine, Robert-Rössle-Str. 10, Berlin 13092, Germany. [4]Institute for Human Genetics, Technical University Munich, Munich, Germany. [5]Institute for Human Genetics, University of Würzburg, Würzburg, Germany. [6]Department of Pediatrics, University Hospital, Technische Universität Dresden, Dresden, Germany.

Received: 24 June 2013 Accepted: 10 October 2013
Published: 14 November 2013

References

1. Mochida GH, Walsh CA: **Molecular genetics of human microcephaly.** *Curr Opin Neurol* 2001, **14:**151–156.
2. Thornton GK, Woods CG: **Primary microcephaly: do all roads lead to Rome?** *TIG* 2009, **25:**501–510. DOI 10.1016/j.tig.2009.09.011.
3. Woods CG, Bond J, Enard W: **Autosomal recessive primary microcephaly (MCPH): a review of clinical, molecular, and evolutionary findings.** *Am J Hum Genet* 2005, **76:**717–728. DOI 10.1086/429930.
4. Nicholas AK, Khurshid M, Desir J, Carvalho OP, Cox JJ, Thornton G, Kausar R, Ansar M, Ahmad W, Verloes A, Passemard S, Misson JP, Lindsay S, Gergely F, Dobyns WB, Roberts E, Abramowicz M, Woods CG: **WDR62 is associated with the spindle pole and is mutated in human microcephaly.** *Nat Gen* 2010, **42:**1010–1014. DOI 10.1038/ng.682.
5. Bacino CA, Arriola LA, Wiszniewska J, Bonnen PE: **WDR62 missense mutation in a consanguineous family with primary microcephaly.** *Am J Med Gen Part A* 2012, **158A:**622–625. DOI 10.1002/ajmg.a.34417.
6. Bhat V, Girimaji SC, Mohan G, Arvinda HR, Singhmar P, Duvvari MR, Kumar A: **Mutations in WDR62, encoding a centrosomal and nuclear protein, in Indian primary microcephaly families with cortical malformations.** *Clin Gen* 2011, **80:**532–540. DOI 10.1111/j.1399-0004.2011.01686.x.
7. Bilguvar K, Ozturk AK, Louvi A, Kwan KY, Choi M, Tatli B, Yalnizoglu D, Tuysuz B, Caglayan AO, Gokben S, Kaymakcalan H, Barak T, Bakircioglu M, Yasuno K, Ho W, Sanders S, Zhu Y, Yilmaz S, Dincer A, Johnson MH, Bronen RA, Kocer N, Per H, Mane S, Pamir MN, Yalcinkaya C, Kumandas S, Topcu M, Ozmen M, Sestan N, Lifton RP, State MW, Gunel M: **Whole-exome sequencing identifies recessive WDR62 mutations in severe brain malformations.** *Nature* 2010, **467:**207–210. DOI 10.1038/nature09327.
8. Kousar R, Hassan MJ, Khan B, Basit S, Mahmood S, Mir A, Ahmad W, Ansar M: **Mutations in WDR62 gene in Pakistani families with autosomal recessive primary microcephaly.** *BMC Neurol* 2011, **11:**119. DOI 10.1186/1471-2377-11-119.
9. Memon MM, Raza SI, Basit S, Kousar R, Ahmad W, Ansar M: **A novel WDR62 mutation causes primary microcephaly in a Pakistani family.** *Mole Biol Rep* 2013, **40:**591–595. DOI 10.1007/s11033-012-2097-7.
10. Murdock DR, Clark GD, Bainbridge MN, Newsham I, Wu YQ, Muzny DM, Cheung SW, Gibbs RA, Ramocki MB: **Whole-exome sequencing identifies compound heterozygous mutations in WDR62 in siblings with recurrent polymicrogyria.** *Am J Med Gen Part A* 2011, **155A:**2071–2077. DOI 10.1002/ajmg.a.34165.
11. Sajid Hussain M, Marriam Bakhtiar S, Farooq M, Anjum I, Janzen E, Reza Toliat M, Eiberg H, Kjaer KW, Tommerup N, Noegel AA, Nurnberg P, Baig SM, Hansen L: **Genetic heterogeneity in Pakistani microcephaly families.** *Clin Gen* 2013, **83:**446–451. DOI 10.1111/j.1399-0004.2012.01932.x.
12. Yu TW, Mochida GH, Tischfield DJ, Sgaier SK, Flores-Sarnat L, Sergi CM, Topcu M, McDonald MT, Barry BJ, Felie JM, Sunu C, Dobyns WB, Folkerth RD, Barkovich AJ, Walsh CA: **Mutations in WDR62, encoding a centrosome-associated protein, cause microcephaly with simplified gyri and abnormal cortical architecture.** *Nat Gen* 2010, **42:**1015–1020. DOI 10.1038/ng.683.
13. Bogoyevitch MA, Yeap YY, Qu Z, Ngoei KR, Yip YY, Zhao TT, Heng JI, Ng DC: **WD40-repeat protein 62 is a JNK-phosphorylated spindle pole protein required for spindle maintenance and timely mitotic progression.** *J Cell Sci* 2012, **125:**5096–5109. DOI 10.1242/jcs.107326.
14. Lahiri DK, Schnabel B: **DNA isolation by a rapid method from human blood samples: effects of MgCl2, EDTA, storage time, and temperature on DNA yield and quality.** *Biochem Genet* 1993, **31:**321–328.
15. Dreszer TR, Karolchik D, Zweig AS, Hinrichs AS, Raney BJ, Kuhn RM, Meyer LR, Wong M, Sloan CA, Rosenbloom KR, Roe G, Rhead B, Pohl A, Malladi VS, Li CH, Learned K, Kirkup V, Hsu F, Harte RA, Guruvadoo L, Goldman M, Giardine BM, Fujita PA, Diekhans M, Cline MS, Clawson H, Barber GP, Haussler D, James Kent W: **The UCSC Genome Browser database: extensions and updates 2011.** *Nucleic Acids Res* 2012, **40:**D918–D923. DOI 10.1093/nar/gkr1055.
16. Li H, Durbin R: **Fast and accurate short read alignment with Burrows-Wheeler transform.** *Bioinformatics* 2009, **25:**1754–1760. DOI 10.1093/bioinformatics/btp324.
17. Li H, Handsaker B, Wysoker A, Fennell T, Ruan J, Homer N, Marth G, Abecasis G, Durbin R: **The sequence alignment/Map format and SAMtools.** *Bioinformatics* 2009, **25:**2078–2079. DOI 10.1093/bioinformatics/btp352.
18. DePristo MA, Banks E, Poplin R, Garimella KV, Maguire JR, Hartl C, Philippakis AA, del Angel G, Rivas MA, Hanna M, McKenna A, Fennell TJ, Kernytsky AM,

Sivachenko AY, Cibulskis K, Gabriel SB, Altshuler D, Daly MJ: **A framework for variation discovery and genotyping using next-generation DNA sequencing data.** *Nat Genet* 2011, **43:**491–498. DOI 10.1038/ng.806.
19. Sherry ST, Ward MH, Kholodov M, Baker J, Phan L, Smigielski EM, Sirotkin K: **dbSNP: the NCBI database of genetic variation.** *Nucleic Acids Res* 2001, **29:**308–311.
20. Cingolani P, Platts A, Wang Le L, Coon M, Nguyen T, Wang L, Land SJ, Lu X, Ruden DM: **A program for annotating and predicting the effects of single nucleotide polymorphisms, SnpEff: SNPs in the genome of Drosophila melanogaster strain w1118; iso-2; iso-3.** *Fly (Austin)* 2012, **6:**80–92. DOI 10.4161/fly.19695.
21. Flicek P, Amode MR, Barrell D, Beal K, Brent S, Carvalho-Silva D, Clapham P, Coates G, Fairley S, Fitzgerald S, Gil L, Gordon L, Hendrix M, Hourlier T, Johnson N, Kahari AK, Keefe D, Keenan S, Kinsella R, Komorowska M, Koscielny G, Kulesha E, Larsson P, Longden I, McLaren W, Muffato M, Overduin B, Pignatelli M, Pritchard B, Riat HS, *et al*: **Ensembl 2012.** *Nucleic Acids Res* 2012, **40:**D84–D90. DOI 10.1093/nar/gkr991.
22. Adzhubei IA, Schmidt S, Peshkin L, Ramensky VE, Gerasimova A, Bork P, Kondrashov AS, Sunyaev SR: **A method and server for predicting damaging missense mutations.** *Nat Methods* 2010, **7:**248–249. DOI 10.1038/nmeth0410-248.
23. Kumar P, Henikoff S, Ng PC: **Predicting the effects of coding non-synonymous variants on protein function using the SIFT algorithm.** *Nat Protoc* 2009, **4:**1073–1081. DOI 10.1038/nprot.2009.86.
24. Pollard KS, Hubisz MJ, Rosenbloom KR, Siepel A: **Detection of nonneutral substitution rates on mammalian phylogenies.** *Genome Res* 2010, **20:**110–121. DOI 10.1101/gr.097857.109.
25. Schwarz JM, Rodelsperger C, Schuelke M, Seelow D: **MutationTaster evaluates disease-causing potential of sequence alterations.** *Nat Methods* 2010, **7:**575–576. DOI 10.1038/nmeth0810-575.
26. Davydov EV, Goode DL, Sirota M, Cooper GM, Sidow A, Batzoglou S: **Identifying a high fraction of the human genome to be under selective constraint using GERP++.** *PLoS Comput Biol* 2010, **6:**e1001025. DOI 10.1371/journal.pcbi.1001025.
27. Chun S, Fay JC: **Identification of deleterious mutations within three human genomes.** *Genome Res* 2009, **19:**1553–1561. DOI 10.1101/gr.092619.109.
28. Neitzel H: **A routine method for the establishment of permanent growing lymphoblastoid cell lines.** *Hum Genet* 1986, **73:**320–326.
29. Issa L, Mueller K, Seufert K, Kraemer N, Rosenkotter H, Ninnemann O, Buob M, Kaindl AM, Morris-Rosendahl DJ: **Clinical and cellular features in patients with primary autosomal recessive microcephaly and a novel CDK5RAP2 mutation.** *Orphanet J Rare Dis* 2013, **8:**59.
30. Rabinovitch PS, Kubbies M, Chen YC, Schindler D, Hoehn H: **BrdU-Hoechst flow cytometry: a unique tool for quantitative cell cycle analysis.** *Exp Cell Res* 1988, **174:**309–318.
31. Schindler D, Hoehn H: **Flow cytometric testing for syndromes with chromosomal instability**. In *Diagnostic cytogenetics*. Edited by RD W. Berlin: Springer; 1999:269–281.
32. Swaiman K: *Swaiman's Pediatric Neurology. Part I. Clinical Examination. 3. Neurologic Examination after the Newborn Period until 2 Years of Age*.5th edition. New Barnet, Herts, UK: Elsevier Saunders; 2012:e33–e42.
33. Julian M, Tollon Y, Lajoie-Mazenc I, Moisand A, Mazarguil H, Puget A, Wright M: **Gamma-Tubulin participates in the formation of the midbody during cytokinesis in mammalian cells.** *J Cell Sci* 1993, **105**(Pt 1):145–156.
34. Moynihan L, Jackson AP, Roberts E, Karbani G, Lewis I, Corry P, Turner G, Mueller RF, Lench NJ, Woods CG: **A third novel locus for primary autosomal recessive microcephaly maps to chromosome 9q34.** *Am J Hum Gen* 2000, **66:**724–727. DOI 10.1086/302777.
35. Lizarraga SB, Margossian SP, Harris MH, Campagna DR, Han AP, Blevins S, Mudbhary R, Barker JE, Walsh CA, Fleming MD: **Cdk5rap2 regulates centrosome function and chromosome segregation in neuronal progenitors.** *Development* 2010, **137:**1907–1917. DOI 10.1242/dev.040410.
36. Bikeye SN, Colin C, Marie Y, Vampouille R, Ravassard P, Rousseau A, Boisselier B, Idbaih A, Calvo CF, Leuraud P, Lassalle M, El Hallani S, Delattre JY, Sanson M: **ASPM-associated stem cell proliferation is involved in malignant progression of gliomas and constitutes an attractive therapeutic target.** *Cancer Cell Int* 2010, **10:**1. DOI 10.1186/1475-2867-10-1.
37. Megraw TL, Sharkey JT, Nowakowski RS: **Cdk5rap2 exposes the centrosomal root of microcephaly syndromes.** *Trends Cell Biol* 2011, **21:**470–480. DOI 10.1016/j.tcb.2011.04.007.
38. Kraemer N, Issa L, Hauck SC, Mani S, Ninnemann O, Kaindl AM: **What's the hype about CDK5RAP2?** *Cell Mol Life Sci* 2011, **68:**1719–1736. DOI 10.1007/s00018-011-0635-4.
39. Caspi M, Coquelle FM, Koifman C, Levy T, Arai H, Aoki J, De Mey JR, Reiner O: **LIS1 missense mutations: variable phenotypes result from unpredictable alterations in biochemical and cellular properties.** *J Biol Chem* 2003, **278:**38740–38748. DOI 10.1074/jbc.M301147200.
40. Hu CK, Coughlin M, Mitchison TJ: **Midbody assembly and its regulation during cytokinesis.** *Mol Biol Cell* 2012, **23:**1024–1034. DOI 10.1091/mbc.E11-08-0721.
41. Dumont S, Mitchison TJ: **Compression regulates mitotic spindle length by a mechanochemical switch at the poles.** *Curr Biol* 2009, **19:**1086–1095. DOI 10.1016/j.cub.2009.05.05.
42. Silk AD, Holland AJ, Cleveland DW: **Requirements for NuMA in maintenance and establishment of mammalian spindle poles.** *J Cell Biol* 2009, **184:**677–690. DOI 10.1083/jcb.200810091.
43. Khodjakov A, Gabashvili IS, Rieder CL: **"Dumb" versus "smart" kinetochore models for chromosome congression during mitosis in vertebrate somatic cells.** *Cell Motil Cytoskeleton* 1999, **43:**179–185. DOI 10.1002/(SICI)1097-0169(1999)43:3<179::AID-CM1>3.0.CO;2–4.
44. Bond J, Woods CG: **Cytoskeletal genes regulating brain size.** *Curr Opin Cell Biol* 2006, **18:**95–101. DOI 10.1016/j.ceb.2005.11.004.

doi:10.1186/1750-1172-8-178
Cite this article as: Farag *et al.*: Abnormal centrosome and spindle morphology in a patient with autosomal recessive primary microcephaly type 2 due to compound heterozygous *WDR62* gene mutation. *Orphanet Journal of Rare Diseases* 2013 **8**:178.

von Bernuth *et al. Orphanet Journal of Rare Diseases* 2014, **9**:116
http://www.ojrd.com/content/9/1/116

ORPHANET JOURNAL OF RARE DISEASES

LETTER TO THE EDITOR Open Access

Combined immunodeficiency develops with age in Immunodeficiency-centromeric instability-facial anomalies syndrome 2 (ICF2)

Horst von Bernuth[1,2*], Ethiraj Ravindran[3,4†], Hang Du[5†], Sebastian Fröhler[5], Karoline Strehl[1], Nadine Krämer[3,4], Lina Issa-Jahns[3,4], Borko Amulic[6], Olaf Ninnemann[3], Mei-Sheng Xiao[5], Katharina Eirich[7], Uwe Kölsch[2], Kathrin Hauptmann[8], Rainer John[4], Detlev Schindler[7], Volker Wahn[1], Wei Chen[5*] and Angela M Kaindl[3,4*]

Abstract

The autosomal recessive immunodeficiency-centromeric instability-facial anomalies syndrome (ICF) is characterized by immunodeficiency, developmental delay, and facial anomalies. ICF2, caused by biallelic *ZBTB24* gene mutations, is acknowledged primarily as an isolated B-cell defect. Here, we extend the phenotype spectrum by describing, in particular, for the first time the development of a combined immune defect throughout the disease course as well as putative autoimmune phenomena such as granulomatous hepatitis and nephritis. We also demonstrate impaired cell-proliferation and increased cell death of immune and non-immune cells as well as data suggesting a chromosome separation defect in addition to the known chromosome condensation defect.

Keywords: ZBTB24, ICF2, Immunodeficiency, Microcephaly, Intellectual disability, Centromeric instability, Facial anomalies, Granulomas

Letter to the editor

The autosomal recessive immunodeficiency-centromeric instability-facial anomalies (ICF) syndrome is characterized by immunodeficiency, intellectual deficit, and facial dysmorphism [1]. ICF 1 and 2 are caused by biallelic mutations in the DNA methyltransferase 3B gene *DNMT3B* (MIM*602900, [2,3]) and in the zinc-finger-and BTB-domain containing 24 gene *ZBTB24* (MIM*614064, [4]), respectively. For ICF2, 16 patients from 13 families have been reported (Additional file 1: Table S1) [4-13]. ICF is considered primarily as a humoral immunodeficiency disease; however, this does not explain the high rate of opportunistic infections. Recently, an additional intrinsic T-cell deficiency in ICF has been discussed and a lymphocyte proliferation defect described in individual patients with ICF1 and ICF2 [5,8,9]. Mechanisms underlying the neurological phenotype of ICF remain to be elucidated. Here, we report the development of a combined immunodeficiency in a patient with ICF2 with age and demonstrate pathomechanisms that may contribute to the immunological and non-immunological phenotype.

The index patient was born hypotrophic at term without complications as the first child of non-consanguineous healthy, Caucasian parents of German descent after an uneventful pregnancy. She showed multiple facial anomalies, clubbing of fingers and toes, and fused teeth (Figure 1A). Language and motor development appeared initially normal, but intellectual disability became apparent by the second year of life. Her brain morphology was normal on MRI at 4 years-of-age, apart from a pineal cyst. Growth stagnated at 4.5 years-of-age with height, weight, and head circumference of 101 cm (-4.79 SD), 15 kg (-2.51 SD), and 50 cm (-1.2 SD) at 9 years-of-age (Figure 1A). Bone age was delayed by 4 years at 8 years-of-age, and growth hormone levels were undetectable but could be stimulated.

* Correspondence: horst.von-bernuth@charite.de; wei.chen@mdc-berlin.de; angela.kaindl@charite.de
†Equal contributors
[1]Pediatric Pneumology and Immunology, Charité - Universitätsmedizin Berlin, Augustenburger Platz 1, 13353 Berlin, Germany
[5]Berlin Institute for Medical Systems Biology, Max-Delbrueck-Center for Molecular Medicine, Robert-Rössle-Str. 10, 13092 Berlin, Germany
[3]Institute of Cell Biology and Neurobiology, Charité – Universitätsmedizin Berlin, Augustenburger Platz 1, 13353 Berlin, Germany
Full list of author information is available at the end of the article

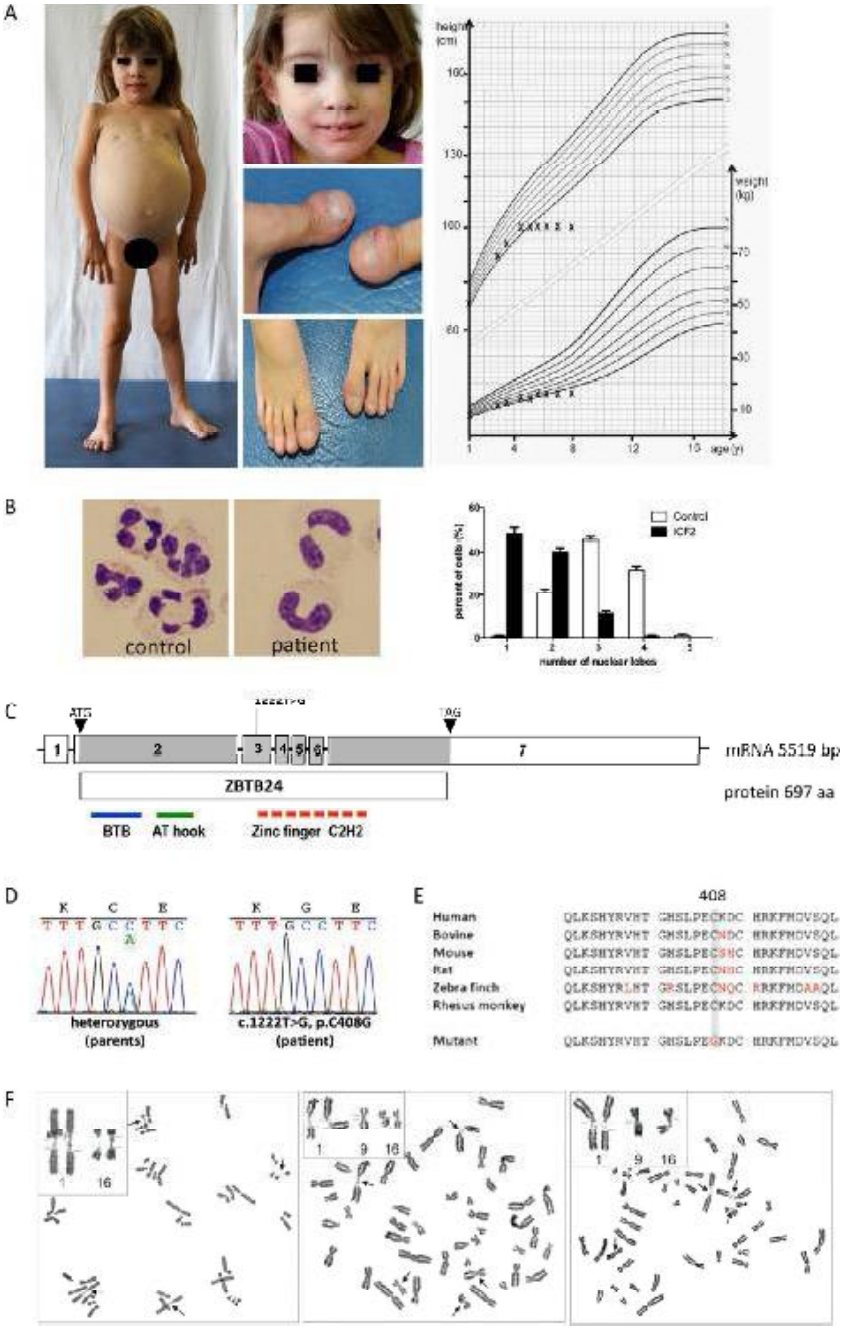

Figure 1 (See legend on next page.)

(See figure on previous page.)
Figure 1 Phenotype and genotype of index patient with *ZBTB24* mutation. (A) Clinical signs at 8 years-of-age: protruding abdomen due to organomegaly in the otherwise underweight girl of short statue, facial dysmorphism (hypertelorism, epicanthal folds, flat nasal bridge, hypertelorism, slight ptosis, prominent forehead). Large teeth result from a fusion of first molar with the incisors. Fingers and toes showed clubbing. Failure to thrive evident in a percentile height-weight-curve.**(B)** Pseudo-Pelger-Huët anomaly of neutrophils (Diff-Quick staining, 100x, n = 400 cells, Student's t-test, $p < 0.0001$). **(C)** Site of homozygous *ZBTB24* mutation c.1222 T > G (protein domains: BTB, bric-a-bric, tramtrack, broad complex domain; AT hook, DNA-binding domain with a preference for A/T rich regions, Zinc finger C2H2).**(D)** Electropherogram traces in patient and heterozygous parents (NM_014797) indicating mutation confirmed by Sanger sequencing. Unaltered*ZBTB24* mRNA levels and product size is depicted in Additional file 8: Figure S2. **(E)** Highly conserved amino acids affected by the inherited homozygous mutation (p.C408G).**(F)** Spontaneous undercondensation of constitutive heterochromatin of chromosomes 1q, 16q, and (to a lesser extent) 9q.

Signs suggestive of an immune defect were recurrent infections of the upper airways beginning at 9 months, a pneumonia at 2.5 years-of-age (*Enterobacter cloacae*), recurrent and protracted diarrhoea (enteropathogenic *E. coli*), and a prolonged skin infection (*Streptococcus pyogenes*). At 3 years-of-age, a 'common variable immunodeficiency (CVID)' was diagnosed based on the global reduction of immunoglobulins and the lack of antibodies against recall antigens despite regular vaccination (Additional file 2: Table S2), subcutaneous IgG substitution was started, and the patient subsequently remained free of invasive infections. Further analysis revealed microcytic hypochrome anemia with anisocytosis, normal global T-/B-cell counts, intermittent neutropenia, and Pseudo-Pelger-Huët anomaly of neutrophilic granulocytes suggestive of a terminal neutrophil differentiation defect (Additional file 3: Table S3, Figure 1B). The patient (blood group 0) lacked isohemagglutinins against blood group substances A and B. Starting at 3.5 years-of-age, CD8+ T-cells were elevated and CD4+ T-cells dropped, leading to a profoundly reduced CD4/CD8 ratio (Additional file 3: Table S3). In parallel to the CD8+ T-cell expansion, relative numbers of CD4 + CD45RA + naïve T-cells declined, resulting in a relative CD4 + CD45R0+ T-cell increase (Additional file 3: Table S3). The TCRVβ-repertoire was normal, and bone marrow analysis excluded myelodysplasia. Lymphocyte proliferation was strongly reduced upon stimulation with mitogens, CD3-directed antibody, and tetanus toxoid despite appropriate tetanus vaccination (Additional file 4: Table S4). Initially normal NK-cell numbers declined gradually, and diminished NK-cell mediated lysis could be restored only partly through IL-2 addition (Additional file 3: Table S3, Additional file 5: Table S5).

Massive hepatosplenomegaly developed by 3 years that progressed to liver cirrhosis by 9 years-of-age. Repeated liver biopsies at 4.5 and 8.5 years-of-age revealed chronically active interface hepatitis with periportal lymphoid infiltrates and fibrosis (Additional file 6: Figure S1); no infection with hepatotopic viridae (cytomegalovirus, Epstein Barr virus, herpes viridae (HSV1, HSV2, HHV6, HHV7), hepatitis viridae A-E, adenovirus, enterovirus, parvovirus B19, hantavirus, and human polyoma virus BK-virus) or mycobacteriae was detected (Additional file 7: Table S6). Compensated renal insufficiency at 4.5 years-of-age prompted a kidney biopsy that revealed interstitial granulomatous nephritis (Additional file 6: Figure S1), but no evidence of mycobacterial infection through PCR, staining procedure, and direct culture. A four-week course of immunosuppressive treatment with corticosteroids and azathioprine was not successful in normalizing liver enzymes or kidney function. The increase of CD8+ T-cells is likely an autoimmune phenomenon non-responsive to standard immunosuppressive treatment; however, an ongoing, non-identified chronic infection cannot be ruled out. The increase of IgA, IgM, and IgG later in life can be an effect secondary to progressive liver cirrhosis. The patient is still under IgG-substitution, and protein-electrophoresis revealed no indication of an increase of mono- or oligoclonal immunoglobulins (data not shown).

By whole exome sequencing, we identified the homozygous missense mutation c.1222 T > G of the *ZBTB24* gene (NM_014797) in the index patient inherited from the healthy parents (Figure 1C). This previously described mutation alters evolutionarily conserved amino acids in a highly conserved zinc finger domain (p.C408G; Figure 1D,E, Additional file 1: Table S1). Patients with the c.1222 T > G mutation show a variable phenotype, arguing against a clear genotype-phenotype correlation and for a residual activity of mutant ZBTB24. In line with this, *ZBTB24* mRNA levels did not differ significantly between patient and control (Additional file 8: Figure S2). Chromosome metaphase preparations revealed increased rates of undercondensated juxta-centromeric chromosomes 1q, 16q, and less frequent of 9q regions, characteristic for ICF2 (Figure 1F). This further increased upon exposure of cultures to 5-azacytidine (DNA methylation interfering agent), eventually resulting in chromosome instability (data not shown). Because ZBTB24 not only impacts on immune cells, we examined patient fibroblasts and detected significantly reduced proliferation, increased apoptosis and discrete spindle defects (broader and unfocused microtubule poles; Figure 2A-D, Additional file 9: Figure S3). In mutant cells, centrosomal CDK5RAP2 was strongly reduced, while centrosomal y-tubulin staining

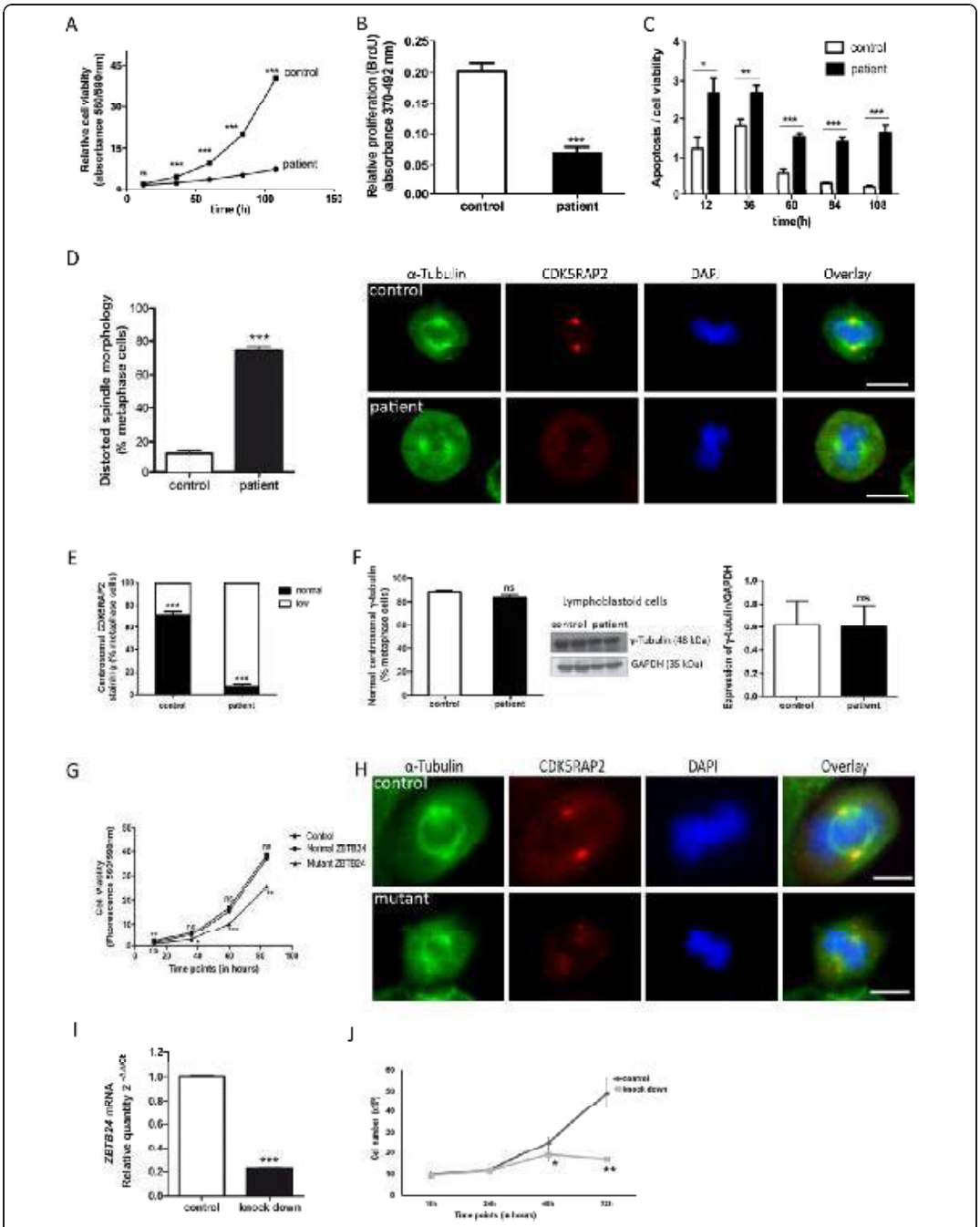

Figure 2 (See legend on next page.)

(See figure on previous page.)
Figure 2 Cellular defects in patient fibroblasts and lymphoblastoid cells, reproduced in HEK cells through siRNA and expression of mutant ZBTB24. (A) Reduced cell viability (n = 8 per time period, Student's t-test), **(B)** reduced proliferation (n = 8, 36 h after plating, Student's t-test), and **(C)** increased apoptosis of *ZBTB24* mutant fibroblasts (activated caspase 3/7 per cell viability; n = 8, Student's t-test). **(D)** Abnormal spindle (α-tubulin) formation with increase of slightly broader, unfocused microtubules poles (n = 100 metaphase LCLs, Student's t-test, view Additional file 9: Figures S3 for further images throughout the cell cycle and specifically in metaphase cells) and **(E, F)** strongly reduced fluorescence signals of centrosomal marker CDK5RAP2 (but not γ-tubulin) in patient lyphoblastoid cells (n = 105 metaphase cells, Student's t-test); total γ-tubulin levels were unaltered (n = 3, Student's t-test). Scale bar 5 μm. View Additional file 10: Figures S4 for further images throughout the cell cycle and specifically in metaphase cells. **(G)** Reduced cell viability (n = 8 per time period, One-way ANOVA) and **(H)** mitotic spindles defect in HEK cells expressing mutant (c.1222 T > G) *ZBTB24*. Abnormal spindle formation with slightly broader, unfocused microtubule poles in mutant cells. Scale bar 5 μm. View Additional file 11: Figure S5 for further images throughout the cell cycle, qPCR and Western blot results. **(I)** *ZBTB24* mRNA downregulation in HEK through siRNA (qPCR, Student's t-test) causes **(J)** reduced cell culture growth (n = 3 per group per time period; Student's t-test). ns = not significant, *p < 0.05, **p < 0.01, ***p < 0.001.

and total γ-tubulin levels were normal (Figure 2E,F, Additional file 10: Figure S4). The mechanisms underlying the reduction in CDK5RAP2, which is associated with stem cell proliferation and microcephaly with intellectual deficit [14], may be involved in the pathogenesis of the neurological phenotype of ICF.

We further mimicked the situation in the patient through *ZBTB24* siRNA knockdown experiments in HEK293 cells and over-expressed mutant and wild-type ZBTB24 in these cells (Figure 2G-J). Cell culture growth was significantly reduced when mutant, but not wild-type, ZBTB24 was expressed, and both discrete spindle defects and an abnormal centrosomal CDK5RAP2 staining were observed (Figure 2G,H, Additional file 11: Figure S5). Down-regulation of ZBTB24 through siRNA similarly reduced cell culture growth (Figure 2 I,J).

The novelty of our report lies in the description of the development of a combined immunodeficiency (CID) with age in ICF2, a feature that may be missed if immunological work-up is only performed once at a young age. We also highlight findings consistent with autoimmune phenomena (hepatitis, nephritis), which are commonly seen in CID but not acknowledged for ICF [15]. Finally, we report for the first time a defect in cell survival and proliferation in immune and non-immune cells. This may constitute a disease mechanism common for both the non-immunological and immunological features of ICF2, the latter presenting as CID. The clinical course of the index patient and of previously reported patients calls for consideration of early stem cell transplantation as an option in patients with ICF.

Please see Additional file 12: Materials and Methods for details on materials and methods.

Consent statement

Written informed consent was obtained from the patient's legal guardian for publication of this case report and any accompanying images. A copy of the written consent is available for review by the Editor-in-Chief of this journal.

Additional files

Additional file 1: Table S1. Genotype and phenotype of all published ICF2 patients.

Additional file 2: Table S2. Immunoglobulin levels and antibody titers.

Additional file 3: Table S3. Blood counts and lymphocyte subpopulations.

Additional file 4: Table S4. Lymphocyte proliferation assays.

Additional file 5: Table S5. NK-cell cytotoxicity assay. Percentages of lysed K562 cells at different effector:target ratios with and without supplementation with IL-2 at the age of 4 years are shown.

Additional file 6: Figure S1. Histological biopsy results. (A) Liver biopsy at the age of 4,5 years. Portal lymphocytic infiltrates and interface hepatitis. (B) Liver biopsy at the age of 8,5 years. Porto-portal bridging. (C) Kidney biopsy at the age of 4,5 years. Normal glomerula. (D) Kidney biopsy at the age of 4,5 years showed multifocal inflammatory infiltrates in cortex and medulla of the tubulo-interstitium and a multinuclear giant cell.

Additional file 7: Table S6. Pathogens excluded to cause hepatitis.

Additional file 8: Figure S2. ZBT24 mRNA levels in controls and fibroblasts. (A) RT-PCR of *ZBTB24* in fibroblasts of controls and the patient. (B) Quantitative RT-PCR of *ZBTB24* in fibroblasts of a control cell line and the patient.

Additional file 9: Figure S3. Mitotic spindles defect in *ZBTB24* mutant patient cells. Subcellular localization of the spindle marker α-tubulin (green) and the centrosome marker CDK5RAP2 (red) of immortalized lymphocytes of (A) control and (B) ICF2 patient throughout the cell cycle. DNA was stained with DAPI (blue). Patient cells have abnormal spindle formation with an increase of slightly broader, unfocused microtubules poles. The fluorescence signals of the centrosomal marker CDK5RAP2 are strongly reduced in patient cells when compared to control cells. Immunofluorescence, scale bar 5 μm.

Additional file 10: Figure S4. Abnormal CDK5RAP2 and normal γ-tubulin staining of centrosomes in *ZBTB24* mutant patient cells. (A) Subcellular localization of the centrosome marker CDK5RAP2 (red) in the metaphase of immortalized lymphocytes of control and ICF2 patient. DNA was stained with DAPI (blue). Centrosomal CDK5RAP2 is strongly reduced in *ZBTB24* mutant lymphocytes when compared to controls. (B) Subcellular localization of the centrosome marker γ-tubulin (green) in the metaphase of immortalized lymphocytes of control and ICF2 patient. DNA was stained with DAPI (blue). No strong difference between the γ-tubulin immunostaining of control and ICF2 patient Immunofluorescence, scale bar 5 μm.

Additional file 11: Figure S5. Mimicking ICF2 in HEK cells. (A) *ZBTB24* mRNA levels and in mock-transfected HEK cells ("control"), HEK cells transfected with HA-tagged normal *ZBTB24* or mutant c.1222 T > G *ZBTB24*, assessed by qPCR. (B) Western-Blot of ZBTB24 of protein extracts from similarly transfected HEK cells using antibodies directed against HA-tag and against ZBTB24 (reference proteins GAPDH and actin). (C) Subcellular localization of the centrosome marker γ-tubulin (green) and

the centrosome marker CDK5RAP2 (red) throughout the cell cycle in mock-transfected HEK cells ("control") and HEK cells transfected with mutant c.1222 T > G *ZBTB24*.

Additional file 12: Materials and Methods.

Abbreviations

CID: Combined immunodeficiency; *DNMT3B*: DNA methyltransferase 3B gene; ICF: Immunodeficiency-centromeric instability-facial anomalies syndrome; SD: Standard deviation; *ZBTB24*: Zinc-finger-and BTB-domain containing 24 gene.

Competing interests

The authors declare that they have no competing interests.

Authors' contributions

AMK, HvB, and WC were responsible for the project conception. AMK and HvB wrote the manuscript. HvB, VW, RJ, and AMK attended the patient and provided clinical data. ER, UK, CM, and LI performed the lymphocyte and fibroblast analyses. ER, KS, and NK performed Sanger sequencing and generated figures. HD and ER performed the HEK cell experiments. MX performed qPCR experiments. HD performed exome sequencing data analysis. BA and AZ performed analysis of the peripheral neutrophilic granulocytes KH performed histology of liver, kidney and bone marrow. DS and KE performed cell cycle and chromosome condensation and breakage analyses. All authors read, revised and approved the final manuscript.

Acknowledgements

The authors thank the patient and her family for participating in this study and D. Müller, W. Luck, S. Henning, M. Becker, A.H. Lebrun, M. Bauer, N. Unterwalder, M. Oberreit, P. Ellensohn, C. Seib, R. Zeller, J. Fassbender, M. Feldkamp, C. Langnick, C. Bassir, B. Spors, and C. Meisel for clinical care for the patient, providing radiological images, discussions, critical reading of the manuscript and technical assistance. This work was supported by the German Research Foundation (DFG, SFB665; BE3895/3-1), the Federal Ministry of Education and Research (BMBF, PID-NET-01GM1111D TP-A5), the Helmholtz Association by the Berlin Institute of Health (BIH), the Sonnenfeld-Stiftung, the German Academic Exchange Service (DAAD), the China Scholarship Council (CSC), the German Ministry of Education and Research (BMBF), and the Senate of Berlin by funds to the Berlin Institute for Medical Systems Biology (BIMSB).

Author details

[1]Pediatric Pneumology and Immunology, Charité - Universitätsmedizin Berlin, Augustenburger Platz 1, 13353 Berlin, Germany. [2]Labor Berlin Charité Vivantes GmbH, Department of Immunology, Berlin, Germany. [3]Institute of Cell Biology and Neurobiology, Charité – Universitätsmedizin Berlin, Augustenburger Platz 1, 13353 Berlin, Germany. [4]Pediatric Neurology, Charité - Universitätsmedizin Berlin, Augustenburger Platz 1, 13353 Berlin, Germany. [5]Berlin Institute for Medical Systems Biology, Max-Delbrueck-Center for Molecular Medicine, Robert-Rössle-Str. 10, 13092 Berlin, Germany. [6]Max Planck Institute for Infection Biology, Berlin, Germany. [7]Institute for Human Genetics, Biozentrum, Universität Würzburg, Würzburg, Germany. [8]Institute for Pathology, Charité – Universitätsmedizin Berlin, Berlin, Germany.

Received: 29 May 2014 Accepted: 8 July 2014
Published online: 21 October 2014

References

1. Maraschio P, Zuffardi O, Dalla Fior T, Tiepolo L: **Immunodeficiency, centromeric heterochromatin instability of chromosomes 1, 9, and 16, and facial anomalies: the ICF syndrome.** *J Med Genet* 1988, **25:**173–180.
2. Xu GL, Bestor TH, Bourc'his D, Hsieh CL, Tommerup N, Bugge M, Hulten M, Qu X, Russo JJ, Viegas-Pequignot E: **Chromosome instability and immunodeficiency syndrome caused by mutations in a DNA methyltransferase gene.** *Nature* 1999, **402:**187–191.
3. Hansen RS, Wijmenga C, Luo P, Stanek AM, Canfield TK, Weemaes CM, Gartler SM: **The DNMT3B DNA methyltransferase gene is mutated in the ICF immunodeficiency syndrome.** *Proc Natl Acad Sci U S A* 1999, **96:**14412–14417.
4. de Greef JC, Wang J, Balog J, den Dunnen JT, Frants RR, Straasheijm KR, Aytekin C, van der Burg M, Duprez L, Ferster A, Gennery AR, Gimelli G, Reisli I, Schuetz C, Schulz A, Smeets DF, Sznajer Y, Wijmenga C, van Eggermond MC, van Ostaijen Dam MM, Lankester AC, van Tol MJ, van den Elsen PJ, Weemaes CM, van der Maarel SM: **Mutations in ZBTB24 are associated with immunodeficiency, centromeric instability, and facial anomalies syndrome type 2.** *Am J Hum Genet* 2011, **88:**796–804.
5. Hagleitner MM, Lankester A, Maraschio P, Hulten M, Fryns JP, Schuetz C, Gimelli G, Davies EG, Gennery A, Belohradsky BH, de Groot R, Gerritsen EJ, Mattina T, Howard PJ, Fasth A, Reisli I, Furthner D, Slatter MA, Cant AJ, Cazzola G, van Dijken PJ, van Deuren M, de Greef JC, van der Maarel SM, Weemaes CM: **Clinical spectrum of immunodeficiency, centromeric instability and facial dysmorphism (ICF syndrome).** *J Med Genet* 2008, **45:**93–99.
6. Cerbone M, Wang J, Van der Maarel SM, D'Amico A, D'Agostino A, Romano A, Brunetti-Pierri N: **Immunodeficiency, centromeric instability, facial anomalies (ICF) syndrome, due to ZBTB24 mutations, presenting with large cerebral cyst.** *Am J Med Genet A* 2012, **158A:**2043–2046.
7. Chouery E, Abou-Ghoch J, Corbani S, El Ali N, Korban R, Salem N, Castro C, Klayme S, Azoury-Abou Rjeily M, Khoury-Matar R, Debo G, Germanos-Haddad M, Delague V, Lefranc G, Mégarbané A: **A novel deletion in ZBTB24 in a Lebanese family with immunodeficiency, centromeric instability, and facial anomalies syndrome type 2.** *Clin Genet* 2012, **82:**489–493.
8. Nitta H, Unoki M, Ichiyanagi K, Kosho T, Shigemura T, Takahashi H, Velasco G, Francastel C, Picard C, Kubota T, Sasaki H: **Three novel ZBTB24 mutations identified in Japanese and Cape Verdean type 2 ICF syndrome patients.** *J Hum Genet* 2013, **58:**455–460.
9. Weemaes CM, van Tol MJ, Wang J, van Ostaijen-Ten Dam MM, van Eggermond MC, Thijssen PE, Aytekin C, Brunetti-Pierri N, van der Burg M, Graham Davies E, Ferster A, Furthner D, Gimelli G, Gennery A, Kloeckener-Gruissem B, Meyn S, Powell C, Reisli I, Schuetz C, Schulz A, Shugar A, van den Elsen PJ, van der Maarel SM: **Heterogeneous clinical presentation in ICF syndrome: correlation with underlying gene defects.** *Eur J Hum Genet* 2013, **21:**1219–1225.
10. Brown DC, Grace E, Sumner AT, Edmunds AT, Ellis PM: **ICF syndrome (immunodeficiency, centromeric instability and facial anomalies): investigation of heterochromatin abnormalities and review of clinical outcome.** *Hum Genet* 1995, **96:**411–416.
11. Kloeckener-Gruissem B, Betts DR, Zankl A, Berger W, Gungor T: **A new and a reclassified ICF patient without mutations in DNMT3B and its interacting proteins SUMO-1 and UBC9.** *Am J Med Genet A* 2005, **136:**31–37.
12. Schuetz C, Barbi G, Barth TF, Hoenig M, Schulz A, Moeller P, Smeets D, de Greef JC, van der Maarel SM, Vogel W, Debatin KM, Friedrich W: **ICF syndrome: high variability of the chromosomal phenotype and association with classical Hodgkin lymphoma.** *Am J Med Genet A* 2007, **143A:**2052–2057.
13. Pezzolo A, Prigione I, Chiesa S, Castellano E, Gimelli G, Pistoia V: **A novel case of immunodeficiency, centromeric instability, and facial anomalies (the ICF syndrome): immunologic and cytogenetic studies.** *Haematologica* 2002, **87:**329–331.
14. Kraemer N, Issa L, Hauck SC, Mani S, Ninnemann O, Kaindl AM: **What's the hype about CDK5RAP2?** *Cell Mol Life Sci* 2011, **68:**1719–1736.
15. Schuetz C, Niehues T, Friedrich W, Schwarz K: **Autoimmunity, autoinflammation and lymphoma in combined immunodeficiency (CID).** *Autoimmun Rev* 2010, **9:**477–482.

doi:10.1186/s13023-014-0116-6
Cite this article as: von Bernuth *et al.*: Combined immunodeficiency develops with age in Immunodeficiency-centromeric instability-facial anomalies syndrome 2 (ICF2). *Orphanet Journal of Rare Diseases* 2014 **9**:116.

8.3 CDK5RAP2 loss affects mESC neural differentiation

Kraemer N, **Ravindran E**, Zaqout S, Neubert G, Schindler D, Ninnemann O, Graf R, Seiler AE, Kaindl AM. Loss of CDK5RAP2 affects neural but not non-neural mESC differentiation into cardiomyocytes. *Cell Cycle* 2015; 14:2044-57

Biallelic mutations in the gene encoding centrosomal CDK5RAP2 lead to autosomal recessive primary microcephaly (MCPH), a disorder characterized by pronounced reduction in volume of otherwise architectonical normal brains and intellectual deficit. The current model for the microcephaly phenotype in MCPH invokes a premature shift from symmetric to asymmetric neural progenitor-cell divisions with a subsequent depletion of the progenitor pool. The isolated neural phenotype, despite the ubiquitous expression of CDK5RAP2, and reports of progressive microcephaly in individual MCPH cases prompted us to investigate neural and non-neural differentiation of Cdk5rap2-depleted and control murine embryonic stem cells (mESC). We demonstrate an accumulating proliferation defect of neurally differentiating Cdk5rap2-depleted mESC and cell death of proliferative and early postmitotic cells. A similar effect does not occur in non-neural differentiation into beating cardiomyocytes, which is in line with the lack of non-central nervous system features in MCPH patients. Our data suggest that MCPH is not only caused by premature differentiation of progenitors, but also by reduced propagation and survival of neural progenitors.

http://dx.doi.org/10.1080/15384101.2015.1044169

PLOS ONE

RESEARCH ARTICLE

Novel Alternative Splice Variants of Mouse *Cdk5rap2*

Nadine Kraemer[1,2]*, Lina Issa-Jahns[1,2], Gerda Neubert[1,2], Ethiraj Ravindran[1,2], Shyamala Mani[3], Olaf Ninnemann[1], Angela M. Kaindl[1,2,4]*

1 Institute of Cell Biology and Neurobiology, Charité –Universitätsmedizin Berlin, Berlin, Germany, **2** Department of Pediatric Neurology, Charité –Universitätsmedizin Berlin, Berlin, Germany, **3** Centre for Neuroscience, Indian Institute of Science, Bangalore, India, **4** Sozialpädiatrisches Zentrum (SPZ), Charité – Universitätsmedizin Berlin, Berlin, Germany

* angela.kaindl@charite.de (AMK); nadine.kraemer@charite.de (NK)

OPEN ACCESS

Citation: Kraemer N, Issa-Jahns L, Neubert G, Ravindran E, Mani S, Ninnemann O, et al. (2015) Novel Alternative Splice Variants of Mouse *Cdk5rap2*. PLoS ONE 10(8): e0136684. doi:10.1371/journal.pone.0136684

Editor: Emanuele Buratti, International Centre for Genetic Engineering and Biotechnology, ITALY

Received: June 10, 2015

Accepted: August 10, 2015

Published: August 31, 2015

Data Availability Statement: All relevant data are within the paper and its Supporting Information files.

Funding: This work was supported by German Research Foundation (SFB665), http://www.sfb665.de/; Sonnenfeld Stiftung, http://www.sonnenfeld-stiftung.de/; Federal Ministry of Education and research (BMBF); Berlin Institute of Health (BIH), http://www.bmbf.de/en/; Academic Exchange Service (DAAD), https://www.daad.de/en/. The funders had no role in study design, data collection and analysis, decision to publish, or preparation of the manuscript.

Abstract

Autosomal recessive primary microcephaly (MCPH) is a rare neurodevelopmental disorder characterized by a pronounced reduction of brain volume and intellectual disability. A current model for the microcephaly phenotype invokes a stem cell proliferation and differentiation defect, which has moved the disease into the spotlight of stem cell biology and neurodevelopmental science. Homozygous mutations of the Cyclin-dependent kinase-5 regulatory subunit-associated protein 2 gene *CDK5RAP2* are one genetic cause of MCPH. To further characterize the pathomechanism underlying MCPH, we generated a conditional *Cdk5rap2 LoxP/hCMV Cre* mutant mouse. Further analysis, initiated on account of a lack of a microcephaly phenotype in these mutant mice, revealed the presence of previously unknown splice variants of the *Cdk5rap2* gene that are at least in part accountable for the lack of microcephaly in the mice.

Introduction

Cyclin-dependent kinase-5 regulatory subunit-associated protein 2 (CDK5RAP2) has moved into the spotlight of neuroscience because of its central function in neural stem cell proliferation and thus brain development as well as its proposed role in mammalian brain evolution. Homozygous mutations in the *CDK5RAP2* gene cause autosomal recessive primary microcephaly type 3 (MCPH3) [1,2], a rare developmental disorder of the brain characterized by a pronounced reduction of brain volume, particularly of the neocortex, as well as intellectual disability (reviewed in [3–5]). One current model for the microcephaly phenotype of *CDK5RAP2* mutations invokes a premature shift from symmetric to asymmetric neural progenitor-cell divisions with a subsequent depletion of the progenitor pool and a reduction of the final number of neurons. In addition, we and others have proposed a reduction in cell survival [6,7].

Currently, no animal model exists that perfectly mimics MCPH. In contrast to the reported human phenotype, the *Hertwig's anemia* mice (exon 4 inversion of the *Cdk5rap2* gene, deletion of a large part of the γ-tubulin ring complex (γTuRC) binding domain) not only have microcephaly, but also a hematopoietic phenotype (hypoproliferative anemia, leucopenia,

Competing Interests: The authors have declared that no competing interests exist.

predisposition to hematopoietic tumors) and defects in multiple organs [6]. Two further splice trap mutation mice (*Cdk5rap2*^{RRF465}, *Cdk5rap2*^{RRU031}) are not microcephalic [8]. A good animal model is crucial to linking cellular phenotypes of MCPH to physiological processes in the developing brain and understanding the mechanisms of neocortex development in this context.

In the present study, we report on novel splice variants of murine *Cdk5rap2*, which we identified in the course of the generation of a conditional mutant mouse (*Cdk5rap2 LoxP*/*hCMV Cre*). We were able to attribute the lack of an obvious microcephaly phenotype in these mice at least partially to previously unknown splice variants of the *Cdk5rap2* gene that are expressed in both mutant and wild-type mice.

Material and Methods

Construction of the *Cdk5rap2 LoxP* targeting vector

The conditional gene-targeting vector for the *Cdk5rap2 LoxP*$^{+/+}$ mice was produced from a mouse genomic library clone (*C57BL/6*). The targeting strategy was to conditionally delete exon 3 of *Cdk5rap2* and generate a subsequent stop codon at the beginning of exon 4 by using a Cre-LoxP strategy. The targeting vector was constructed by successive cloning of PCR products and contained 3.4 kb 5′ and 3.5 kb 3′ homology arms and a Neomycin selection cassette. Two LoxP sequences were introduced in similar orientation into intronic regions between exon 2 and 3 as well as between exon 3 and 4 to minimize disruption to the gene function, i.e., with positions about 320 bp before and about 2.2 kb at the end of exon 3. An FRT-Neo selection cassette with two flanking FRT sites for later removal by FLP recombinase [9] was inserted about 300 bp into intron 3 (first FRT site) and 16 bp (second FRT site) before the 3 ' LoxP site (**S1 Fig**).

Generation of *Cdk5rap2 LoxP*+/- *C57BL/6* embryonal stem cells

The linearized targeting construct was electroporated into *C57BL/6N* mouse embryonic stem cells (mESC) grown on feeders and selected using neomycin (6 positive in 372 screened clones). For the resultant clones, the correct insertion of the targeting construct into the genome was subsequently confirmed by PCR over the homologous recombination arm using external primers and further confirmed by Southern blot with Neo internal probe and with 5′ and 3′ external probes (**S1 Fig**, **S1**–**S3 Tables**).

Generation of *Cdk5rap2 LoxP*+/- mice

The *Cdk5rap2 LoxP*$^{+/-}$ mouse line was established at the Institut Clinique de la Souris (ICS, llkirch, France) in accordance with the French law. One verified stem cell clone was selected for *C57BL/6* blastocysts injection, and mESC-derived chimeras [10] gave germline transmission. The resulting chimeric line was verified by PCR using external primers, further confirmed by Southern blot with Neo internal probe (**S1 Fig**) and crossed with a Flip *C57BL/6* deleter mouse to excise the FRT site-flanked Neo cassette on F1 progenies. The F1 animals were crossed with *C57BL/6* mice to generate F2 animals.

Generation of conditional *Cdk5rap2 LoxP*+/+ *hCMV Cre*+ mice

Conditional *Cdk5rap2 LoxP*$^{+/+}$ *hCMV Cre*$^{+}$ mice (cKO) were generated to obtain complete excision of the *Cdk5rap2* exon 3 and introduce a stop codon in exon 4. Breeding of *Cdk5rap2 LoxP*$^{+/+}$ mice with *hCMV Cre*$^{+}$ mice resulted in heterozygous *Cdk5rap2 LoxP*$^{+/-}$ *hCMV Cre*$^{+}$ mice which were then crossed with *Cdk5rap2 LoxP*$^{+/+}$ mice. The latter mice were further breed

among each other. For experiments wildtype (WT), heterozygous knockout (het KO), and homozygous knockout (hom KO) mice were used. The corresponding genotypes are listed in S4 Table. Mice were kept and bred in an enriched environment in a SPF barrier at the animal facility FEM of the Charité - University Medicine Berlin, Germany and all experiments were carried out in accordance with the German ethic principles, approved by the State Office of Health and Social Affairs Berlin (Landesamt für Gesundheit und Soziales; LaGeSo; approval no. T0309/09 and G0113/08). The day of insemination was considered as embryonic day (E) 0 (E0), and the day of birth was designated as postnatal day (P) 0 (P0).

Genotyping

Genomic DNA was isolated from tail sections by proteinase K digestion using standard methods, and genotyping was performed by PCR and subsequent agarose gel electrophoresis using four primer pairs (**S1 Fig, S5 and S6 Tables**).

Mouse samples

Mice were sacrificed by decapitation (P0-P5) or cervical dislocation (adult). For conventional PCR, quantitative real-time PCR (qPCR) and Western blots, the cerebral cortex was quickly dissected from mice at P0 (n = 6 per group), snap-frozen and stored at -80°C for later RNA and protein extraction. For histological analysis, brains from mice at P0 and P5 (n = 6 per age) were dissected and immersed in 4% paraformaldehyde (PFA) in 0.12 M TPO4. Further brain fixation was performed in the same solution at 4°C for 1 –2 h (embryonic brains) or overnight (postnatal brains). Brains were cryoprotected through overnight incubation in 10% sucrose 0.12 M TPO4 solution at 4°C followed by an overnight incubation in 20% sucrose 0.12 M TPO4. The brains were then immersed in a solution of 7.5% gelatin, 20% sucrose in 0.24 M TPO4 for 1 h at 37°C and subsequently embedded in a block with the same solution for 1 h at 4°C. The block was frozen in 2-metylbutan at -60°C and stored at -80°C. Coronal and sagittal sections of 10 μm thickness were cut on a cryostat and collected on Superfrost plus slides (R. Langenbrinck, Emmendingen, Germany).

Human blood samples

mRNA derived from blood samples from controls were used in this study with approval from the local ethics committees of the Charité –University Medicine Berlin (approval no. EA1/212/08). An informed written consent was obtained from all control persons.

Antibodies

We generated two peptide antibodies directed against mouse Cdk5rap2 in collaboration with Pineda antibody service (Berlin, Germany) as previously described [11]: (i) one antibody (N1) directed against a sequence of the N-terminal protein region NH2-DSGMEEE-GALPGTLSGC-COOH; amino acids 2–18 of the Cdk5rap2 mouse sequence encoded by exon 1, accession no. NP_666102.2, and (ii) an antibody (A1) directed against a more centrally located protein region NH2-LKFEADVETPFQSDQHLEQSR-COOH; amino acids 705–725 of the full-length 1822 aa Cdk5rap2 mouse sequence encoded by exon 19, accession no. NP_666102.2. Both peptide sequences are unique for Cdk5rap2, and the specificity of the peptide antibody against Cdk5rap2 was previously tested by Western blot and on brain sections by peptide precompetition [11].

RNA extraction and qPCR

Total RNA was extracted from tissue using TRI-Reagent (Sigma-Aldrich, Taufkirchen, Germany) according to the manufacturer's recommendations. cDNA was prepared from 1 μg of RNA by reverse transcription using the ThermoScript RT-PCR System (Invitrogen, Karlsruhe, Germany) and a combination of oligo(dT)$_{20}$ and random hexamer primers. For qPCR, 1 μl of 1:10 diluted cDNA was used as template. To specifically amplify and detect *Cdk5rap2* (WT allele, KO allele and novel spliced variant) and *Hprt* (Hypoxanthine-guanine phosphoribosyltransferase, reference gene) cDNA, we designed the corresponding specific sets of sense and antisense primers and TaqMan probe using the GenScript real-time PCR (TaqMan) Primer Design online software (www.genscript.com) (**S7 Table**). Experiments (n = 6 per group, heterozygotes n = 5) were run in triplicate. PCR was performed in an Applied Biosystems 7500 Fast Real-time PCR System (Applied Biosystems Inc., Norwalk, CT, USA) in 96-well microtiter plates using a final volume of 13 μl. The reaction mixture consisted of 1x TaqMan Universal PCR Master Mix, No AmpErase UNG (Roche, Branchburg, NJ, USA), 385 nM primer F, 385 nM primer R, 230 nM probe, and 1 μl template cDNA. Amplification was performed with the thermal profile of 50°C for 2 min, initial denaturation at 95°C for 10 min, followed by 40 cycles of denaturation at 95°C for 15 sec and a combined primer annealing/extension step at 60°C for 1 min, during which the fluorescence signal was acquired. Ct values were calculated using the 7500 Fast System SDS Software (Applied Biosystems Inc.), and further statistical calculations were performed on Microsoft Excel (Microsoft Corporation, Bellevue, WA, USA) and GraphPad Prism 5 Software (GraphPad Software Inc., La Jolla, CA, USA). The $2^{-\Delta\Delta Ct}$ method was applied for the quantification of the relative expression of the *Cdk5rap2* mRNA using the reference gene *Hprt* as the endogenous control for normalization.

Sequencing of murine and human *CDK5RAP2* cDNA

cDNA samples were prepared from cortex of P0 mice and from human fibroblasts as described above. Primers used for PCR are given in **S8 Table.** The PCR products were separated on a 1.5% agarose gel, and bands were excised, purified, and cloned into a pCR2.1-TOPO TA vector using the TOPO TA cloning kit (Invitrogen) according to the protocol provided by the manufacturer. Samples were sequenced using M13 forward and reverse primers. The full length *Cdk5rap2* mRNA sequence, accession no. NM_145990.3, was used as reference sequence.

Rapid amplification of cDNA ends (RACE)

To identify putative N-terminally shorter *Cdk5rap2* variants, we applied the 5' RACE-PCR technique (Roche) according to the protocol provided by the manufacturer. Specific primers used for nested PCR are given in **S9 Table**. The PCR products were separated on a 1.5% agarose gel and further processed for sequencing as described above.

Protein extraction procedure and Western blot

Protein extracts for Western blots were isolated from tissues by homogenization in RIPA buffer containing 1 mM PMSF (Sigma-Aldrich) and 1 protease inhibitor cocktail tablet (Complete Mini; Roche Diagnostics, Mannheim, Germany), 20 min incubation on ice and centrifugation at 4°C for 10 min at 3,000 g and for 20 min at 16,000 g. Protein concentrations were determined using a bicinchoninic acid (BCA) based assay, according to the instructions of the manufacturer (BCA Protein Assay Kit; Pierce Biotechnology, Rockford, IL, USA). Protein extracts (30 μg per sample) were denaturated in Laemmli sample loading buffer at 95°C for 5 min, separated by sodium dodecyl sulphate polyacrylamide gel electrophoresis (SDS-PAGE) and

electrophoretically transferred in transfer buffer in a semi-dry fashion using Trans-Blot SD Semi-Dry transfer cell (Bio-Rad, Munich, Germany) onto nitrocellulose membrane (Bio-Rad). The membranes were incubated for 1 h at room temperature (RT) in blocking buffer (TBS-T 1x with 5% bovine serum albumin (BSA)), rinsed three times with TBS-T 1x for 8 min each at RT on a shaker and then incubated overnight at 4°C with rabbit anti-Cdk5rap2 (N1 or A1) (1:500) and mouse anti-beta actin (1:10,000; Sigma-Aldrich) antibodies. After incubation with the corresponding secondary antibodies donkey anti-rabbit (1:2000; Amersham Biosciences, Freiburg, Germany) and goat anti-mouse (1:10,000; Dako, Hamburg, Germany), the immunoreactive proteins were visualized using a technique based on a chemiluminescent reaction. The gel pictures were obtained on photographic films (Amersham Hyperfilm enhanced chemiluminescence (ECL); GE Healthcare, Freiburg, Germany). Western blot experiments were run in triplicate.

Immunohistology and imaging

Cryostat sections were air-dried briefly prior to rinsing in phosphate buffered saline (PBS 1x) for 10 min and in staining buffer (0.2% gelatin, 0.25% Triton X-100 in PBS 1x) for 20 min. In a 30 min blocking step, sections were incubated in 10% donkey normal serum (DNS) in staining buffer at RT. Sections were incubated overnight at RT with primary antibodies in the staining buffer containing 10% DNS followed by an incubation with the corresponding secondary antibodies for 2 h at RT. Nuclei were labeled with 4',6-diamidino-2-phenylindole (DAPI; 1:1000; Sigma-Aldrich). Fluorescently labeled sections were analyzed and imaged by a fluorescent Olympus BX51 microscope with the software Magnafire 2.1B (2001) (Olympus, Hamburg, Germany), and confocal microscopy images were taken by an lsm5exciter Zeiss confocal microscope with the software Zen (version 2009, Zeiss, Jena, Germany). All images were processed using Adobe Photoshop (Adobe Systems, San José, CA, USA).

Blood counts

Blood samples were obtained from mice following cervical dislocation through intracardial puncture and slow aspiration. Blood slides were prepared and blood cells were counted manually.

Cranial MRI analysis

Cranial magnetic resonance imaging (cMRI) was performed using a 7 Tesla rodent scanner (Pharmascan 70/16, Bruker BioSpin, Ettlingen, Germany). For imaging, a ^{1}H-RF quadrature-volume resonator with an inner diameter of 20 mm was used. Data acquisition and image processing were carried out with the Bruker software Paravision 4.0. During the examinations mice were placed on a heated circulating water blanket to ensure constant body temperature of 37°C. Anaesthesia was induced with 3% and maintained with 1.5–2.0% isoflurane (Forene, Abbot, Wiesbaden, Germany) delivered in a O_2 / N_2O mixture (0.3 / 0.7 l/min) via a facemask under constant ventilation monitoring (Small Animal Monitoring & Gating System, SA Instruments, Stony Brook, New York, USA). The animals were placed on a custom-built animal holder. For imaging the mouse brain in axial and sagittal orientation, a T2-weighted 2D turbo spin-echo sequence with a RARE factor of 8 and 4 averages was used. Imaging parameters: (i) axial TR / TE = 4059 / 36 ms, 35 axial slices with slice thickness of 0.5 mm, field of view of (FOV) 2.60 x 2.60 cm, matrix size 256 x 256, (ii) sagittal TR / TE = 4200 / 36 ms, 20 sagittal slices with slice thickness of 0.5 mm, FOV 2.60 x 2.60 cm, matrix size 256 x 256. cMRI data processing was performed with Image J software. Section areas and brain volumes were calculated (n = 4–6 per group).

Results

Generation and verification of conditional *Cdk5rap2 LoxP hCMV* Cre mutant mouse

We generated mutant *Cdk5rap2* mice on a *C57BL/6N* background by introducing a LoxP site flanking exon 3 of the *Cdk5rap2* gene and, following verification steps, breeding the resulting *Cdk5rap2 LoxP*$^{+/-}$ mice with *hCMV* Cre mice (Fig 1A, see Material and Methods and S1 Fig for details). The conditional *Cdk5rap2 LoxP*$^{+/+}$ *hCMV Cre*$^{+}$ mice (cKO) were generated to obtain complete excision of the Cdk5rap2 exon 3 and thereby introduce a frameshift and a subsequent stop codon in exon 4. Heterozygous *Cdk5rap2 LoxP*$^{+/-}$ *hCMV Cre*$^{+}$ mice were crossed with *Cdk5rap2 LoxP*$^{+/+}$ mice, followed by an inbreeding of the resulting mice. For experiments wildtype (WT), heterozygous knockout (het KO), and homozygous knockout (hom KO) mice were used (for corresponding genotypes, see S4 Table).

Lack of phenotype of *Cdk5rap2* mutant mouse

We did not detect a microcephaly phenotype when analyzing the animals through clinical examination, body and brain weight measurements, cMRI analysis, and histological assessment of their brains (S2 Fig). cMRI analysis of brains of hom KO and WT mice at P56 did not reveal a significant reduction of brain or neocortex volume.

Identification of a novel murine *Cdk5rap2* splice variant (*mCdk5rap2-V1*)

To further address this point despite the known background dependency of *Cdk5rap2* mutant mice [6] and thus to verify the correct generation of the planned mutant construct, we performed quantitative real-time PCR (qPCR) analysis using forward primers specific for the WT and the KO allele, respectively, in combination with a common reverse primer and probe. The WT specific primer binds to a sequence in exon 3, while the KO specific primer binds only when exon 3 is deleted completely as it recognizes a sequence composed of the 3 '-end of exon 2 and the 5'-end of exon 4 (Fig 1B, S7 Table). The qPCR confirmed the correct excision of exon 3 in the hom KO mice as *Cdk5rap2* mRNA could only be detected with the KO, but not with the WT specific primer pairs. In line with this, *Cdk5rap2* mRNA could only be detected with the WT but not the KO specific primer pair in the WT, and with both primer pairs in the het KO samples. *Cdk5rap2* mRNA levels were increased in het and hom KO compared to WT (Fig 1B). In addition, we Sanger sequenced cDNA from WT and hom KO mice. The sequencing results also confirmed the correct excision of exon 3 in the hom KO, leading to a frameshift and a premature stop codon in exon 4 (Fig 1C). In the course of the sequencing procedure we performed PCRs to enrich the sequence fragment of interest using forward and reverse primers that bind to exon 2 and 7, respectively. Separation of the respective PCR products revealed an additional band in hom KO and WT which was ~70 bp longer than the expected 586 bp for WT and 518 bp for hom KO, respectively (Fig 1D). This additional band was also detected using primers binding in exon 1 (F) and exon 11 (R) (data not shown). We therefore Sanger sequenced the additional PCR product bands following cloning into TOPO-TA plasmids. We identified a novel murine *Cdk5rap2* splice variant (*mCdk5rap2-V1*) which contains an additional exon (exon 3a) of 71 nucleotides. Exon 3a lies between exon 3 and 4, and its expression in the cKO mouse will abolish the frameshift and stop codon introduced through excision of exon 3 (Fig 1D). In WT mice, translation of *mCdk5rap2-V1* results in a truncated 85 aa protein. This additional exon 3a is not present in human *CDK5RAP2* mRNA (data not shown).

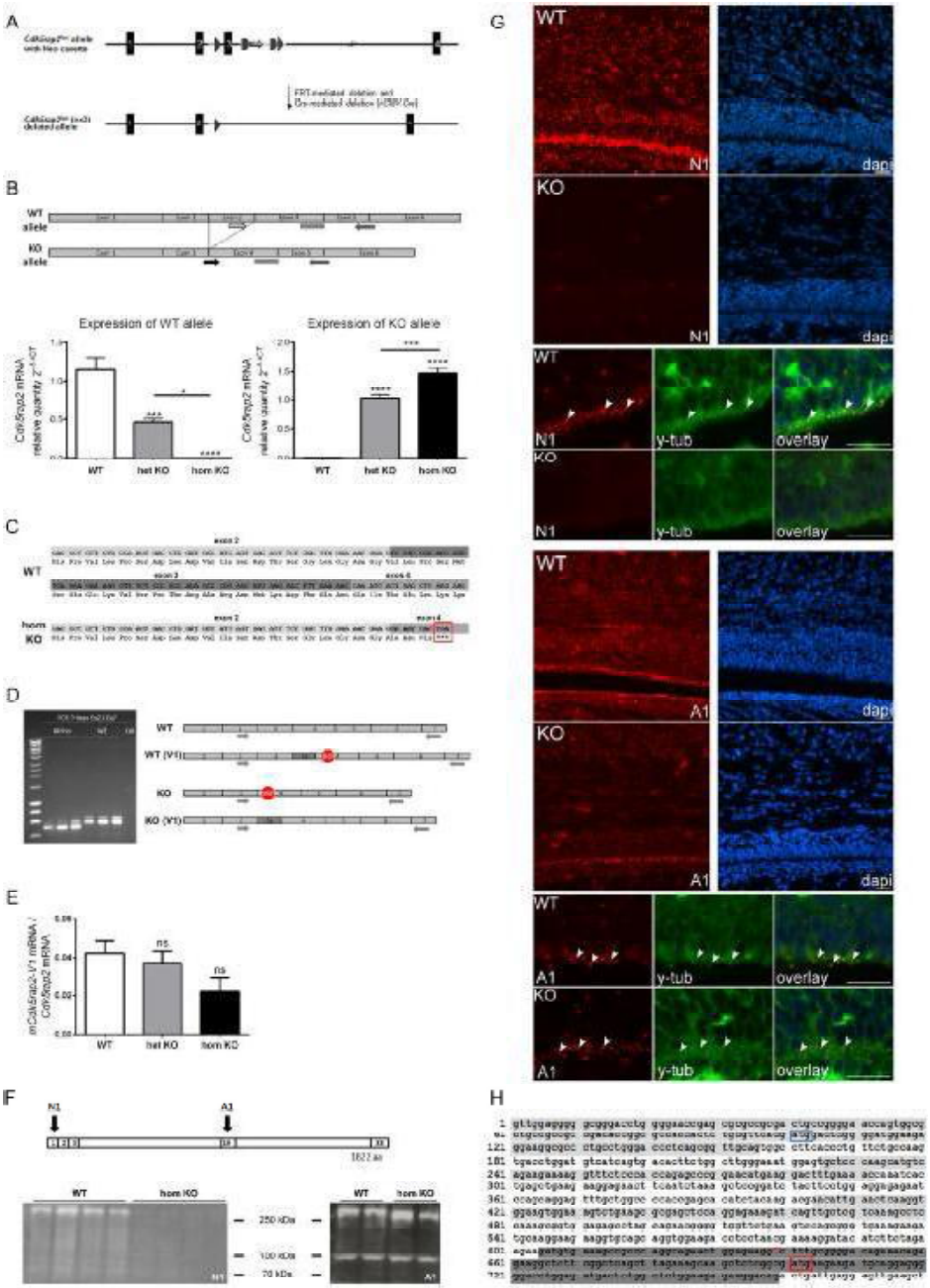

Fig 1. Conditional *Cdk5rap2* KO mouse and novel *mCdk5rap2* splice variants. (A) *Cdk5rap2*^{lox} construct before and after Cre-mediated deletion of exon 3. (B) *Cdk5rap2* WT and KO allele expression in the neocortex of WT, het KO, and hom KO mice at P0. The WT allele is not expressed in hom KO mice; the

KO allele is not expressed in WT mice (qPCR, n = 6 per group, one-way ANOVA, p <0.0001; Bonferroni's Multiple Comparison Test). Position of forward primers specific for the WT and the KO allele, respectively, and the common reverse primer and probe are depicted. (C) Sanger sequencing results of PCR products from exon 2 to exon 7 of WT and hom KO cDNA confirmed the correct excision of exon 3 in hom KO mice, resulting in a frame shift and a premature stop codon (red box). (D) Identification of a novel *mCdk5rap2* splice variant (*mCdk5rap2-V1*) through gel electrophoresis and sequencing of PCR products from exon 2 to exon 7 of WT and hom KO cDNA. In hom KO mice, the additional 71 nucleotides will abolish the frameshift and stop codon introduced through excision of exon 3. In WT mice the additional 71 nucleotides will lead to a frameshift and a premature stop codon resulting in a truncated 85 aa protein. (E) *mCdk5rap2-V1* mRNA expression in the neocortex of WT, het KO, and hom KO mice at P0 (qPCR, n = 6 per group, one-way ANOVA, p = 0.1314; Bonferroni's Multiple Comparison Test). (F) Western blot analysis using the N1 antibody revealed a strong reduction of protein levels below detection levels in hom KO in comparison to WT neocortex at P0, while multiple bands were identified with a reduction in the size of the largest (about 250 kDa) band by about 10 kDa when using the A1 antibody. Binding sites of anti-Cdk5rap2 antibodies N1 and A1 are depicted, numbers refer to exons encoding the corresponding protein regions. (G) Immunostaining using antibodies directed against Cdk5rap2 (red) and the centrosome marker y-tubulin (green) of coronal murine hom KO and WT brain sections at P0; nuclei are stained with DAPI (blue). Overview immunofluorescence pictures and higher magnification images of the subventricular (SVZ) and the ventricular (VZ) zone; arrowheads indicate examples for centrosomes which are co-stained with Cdk5rap2 and y-tubulin; scale bars 20 μm. When applying the N1 antibody, high Cdk5rap2 signal density is present within the neocortex and SVZ/VZ in WT mice, while this is lacking in hom KO mouse brains. The A1 antibody, however, produces Cdk5rap2 immunopositivity in both the hom KO and WT neocortex and SVZ/VZ with a high signal density in the in the WT mice and a similar pattern with only a slight decrease of staining density and intensity in hom KO mice. (H) Excerpt of *Cdk5rap2* mRNA sequence (NM_145990.3, exons 1, 3, and 5 are highlighted in light grey, exon 7 in dark grey) with known start codon in exon 1 (blue box) and alternative start codon in exon 7 (red box) as well as putative sequence start of shorter variant *Cdk5rap2-V2* (red upper case C). ns, not significant, *p<0.05, **p<0.01, ***p<0.001, ****p<0.0001.

doi:10.1371/journal.pone.0136684.g001

Quantification of *mCdk5rap2-V1* mRNA

To quantify the relative mRNA amount of the novel splice variant *mCdk5rap2-V1* in WT, het KO, and hom KO mice, we performed qPCR using the primer and probe set of WT and KO allele specific and common primers as described above. In addition, we applied a *mCdk5rap2-V1* specific forward primer which binds to a sequence in exon 3a. The fraction of *mCdk5rap2-V1* mRNA relative to the *Cdk5rap2* mRNA was very low (4.2% in WT, 3.7% in het KO, 2.2% in hom KO) and was not increased in the het or hom KO mice (Fig 1E).

Second novel murine *Cdk5rap2* splice variant (*mCdk5rap2-V2*)

Cdk5rap2 protein levels were below the detection level when assessed through immunohistological and Western blot analysis of hom KO mouse brains using the N-terminal antibody (N1) binding to amino acids 2–18 of the Cdk5rap2 mouse protein sequence (Fig 1F and 1G). While this is in line with a nonsense-mediated mRNA decay or rapid degradation of the putative truncated Cdk5rap2 protein, we did detect Cdk5rap2 with an antibody (A1) directed towards a more centrally located Cdk5rap2 site, both in immunohistological analysis and in Western blots (Fig 1F and 1G). Sequence analysis of the *Cdk5rap2* gene indicated an ATG site flanked by a Kozak consensus sequence in exon 7 of the *Cdk5rap2* gene to possibly serve as an additional start codon. The existence of a shorter *Cdk5rap2* variant with the translation starting in exon 7 would result in a 1622 aa Cdk5rap2 variant and might explain why low level of or no Cdk5rap2 protein is detected in the hom KO when using an antibody against the N-terminus, while a product can still be identified through a second antibody directed towards amino acids 705–725 of the full-length 1822 aa Cdk5rap2 mouse sequence. To further address this hypothesis of a shorter Cdk5rap2 variant lacking the N-terminus, we performed 5' RACE-PCR analysis using specific primers for the nested PCR directed subsequently against exons 14, 12, and 9. The PCR products yielded three dominant bands which were sequenced following cloning into a TOPO-TA plasmid. Sanger sequencing identified several of the clones starting at base pair position 639 of the *Cdk5rap2* mRNA reference sequence, which is close to the presumptive alternative start codon in exon 7 at position 701 (Fig 1H). The latter results thus indicate the existence of a second, shorter Cdk5rap2 variant lacking the N-terminus.

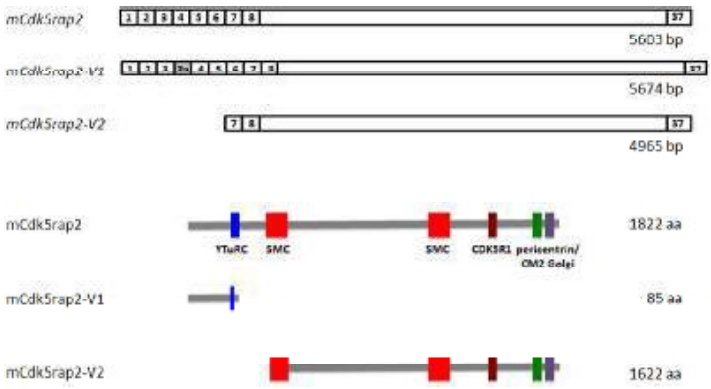

Fig 2. *mCdk5rap2* splice variants. Schematic representation of mCdk5rap2, mCdk5rap2-V1, and mCdk5rap2-V2 mRNA (top) and protein (bottom).

doi:10.1371/journal.pone.0136684.g002

Discussion

The lack of a phenotype of conditional *Cdk5rap2* knockout mice lead us to analyze *Cdk5rap2* mRNA in mutant (hom KO) and wild-type (WT) mice in detail. We thereby identified one mRNA variant (*mCdk5rap2-V1*) with an additional exon 3a, which is expressed both in the WT as well as in the hom KO mice. Given that *mCdk5rap2-V1* is expressed only at very low levels and is not upregulated in the mutant mice, it is unlikely that this variant is solely responsible for the rescue of the phenotype in the *Cdk5rap2* cKO mice. Moreover, we did not detect immunopositivity in hom KO cortical sections when applying the N-terminal antibody N1, which should recognize *mCdk5rap2-V1*. In addition to this, the detection of Cdk5rap2 in hom KO mice cortex with the more C-terminal antibody A1 indicates the existence of an additional variant. In this regard, our data further suggest a second *Cdk5rap2* mRNA variant (*mCdk5rap2-V2*) which lacks the N-terminal part of the full length *Cdk5rap2* mRNA sequence from bp 1 to 638 (exon 1 to 6) and uses an alternative start codon in exon 7. Since in WT mice translation of *mCdk5rap2-V1* results in a truncated 85 aa protein it is most likely that this variant is physiologically redundant (Fig 2). The suggested variant *mCdk5rap2-V2* lacks the γTuRC binding domain, which has been reported to be important for the γTuRC attachment to the centrosome and therefore for the microtubule organizing function of the centrosome [12]. However, *mCdk5rap2-V2* localizes to the centrosome in mouse neocortex, as shown in immunohistological stainings. This allows speculation that potentially targeting Cdk5rap2 to the centrosome is not exclusively dependent of the γTuRC site but rather on interaction with other proteins such as pericentrin. The functional significance of these variants as well as those predicted in genome datasets (S3 Fig) and the human variants (S4 Fig) will need to be addressed in further functional studies.

Supporting Information

S1 Fig. Generation and verification of *Cdk5rap2 LoxP*$^{+/-}$ allele. (A) Schematic representation of the targeting vector. Homologous recombination into the *Cdk5rap2* wildtype allele of mouse embryonic stem cells resulted into the displayed genotype. A correctly targeted ESC clone was injected into blastocyst stage embryos to generate chimeric mice. Chimeras were bred with FLIP (FLP) transgenic mice to generate *Cdk5rap2* LoxP mice lacking the Neo cassette.

Recombinase recognition sites: FRT—Flp recombinase; loxP—Cre recombinase. The correct insertion of the targeting construct into the genome was confirmed by (B) PCR screening of clones, (C) Neo Southern, and (D) external Southern. (E) Genotyping of mice (see **S1 Table** for primer sequences).
(JPG)

S2 Fig. Characterization of conditional *Cdk5rap2* knockout mouse. Conditional *Cdk5rap2* knockout (cKO) mice were generated by breeding *Cdk5rap2 LoxP*$^{+/+}$ mice with *hCMV Cre*$^{+/-}$ mice. P0 and adult (P56) hom KO mice had normal (A) body weight and (B) brain weight when compared to WT controls. (C) Magnetic resonance imaging (MRI) analysis of brains of hom KO and WT mice at P56 revealed no significant difference in brain volume (n = 3–7 per group). There was a slight reduction of neocortex volume (n = 3–4 per group). (D) Hom KO mice had normal blood counts at P56 when compared to WT control mice. Abbreviations: WBC, white blood count; RBC, red blood count; HGB, hemoglobin; HCT, hematocrit; MCV, mean corpuscular volume of erythrocytes; MCH, mean corpuscular hemoglobin of erythrocytes; MCHC, mean corpuscular hemoglobin concentration; PLT, platelet counts. Students t-test; values represent mean ± S.E.M.; $^{*}p<0.05$, $^{**}p<0.01$, $^{***}p<0.001$.
(JPG)

S3 Fig. Known and predicted *mCdk5rap2* transcript variants in genome datasets. In addition to the *mCdk5rap2* RefSeq NM_145990.3 (Ensembl transcript ID: ENSMUST00000144099) the available genome databases (NCBI, Ensembl, MGI) list several *mCdk5rap2* variants, which have not been confirmed so far. The NCBI dataset comprises 10 predicted transcript variants (X1 –X10), annotated using the gene prediction method Gnomon and thus supported by mRNA and EST evidence. In all cases, the support level by ESTs is very low as only one or maximal two ESTs are available for altered regions. Ensemble lists 5 additional transcript variants: two without an open reading frame, hence not protein-encoding, one predicted to undergo nonsense mediated decay, and two which are predicted to be protein coding. All of these variants have a low transcript support level according to the Ensembl definition. None of these predicted variants is similar to *mCdk5rap2-V1* or *mCdk5rap2-V2*. Given the large size of the *mCdk5rap2* gene, it is most likely that more transcript variants exist as already confirmed for the human *CDK5RAP2* (S4 Fig). Further investigation will be needed to compile the existing variants which might be helpful to understand the diverse physiological functions of Cdk5rap2 in different tissues.Schematic diagram of *mCdk5rap2* transcript variants. Exon numbering is according to the *mCdk5rap2* RefSeq NM_145990.3; schematic exons do not reflect the actual exon size. Changes in predicted variants compared to the RefSeq NM_145990.3 are marked with red for additional exons, blue for exons containing additional base pairs, and green for shortened exons missing some base pairs.
(JPG)

S4 Fig. Human *CDK5RAP2* transcript variants in genome datasets. Overview about all human *CDK5RAP2* transcript variants listed in genome databases (NCBI, Ensembl, MGI) so far. Schematic diagram of *CDK5RAP2* transcript variants. Exon numbering is according to the *CDK5RAP2*, transcript variant 1 RefSeq NM_018249.5; schematic exons do not reflect the actual exon size. Changes in variants compared to the RefSeq NM_018249.5 are marked with red for additional exons, blue for exons containing additional base pairs, green for shortened exons missing some base pairs, and with 'in' for retained introns.
(JPG)

S1 Table. Primer sequences used for PCR validation of positive ESC clones.
(DOCX)

S2 Table. Neo Southern: Digestions used to validate the 5' and 3' insertion.
(DOCX)

S3 Table. External Probe Southern: Digestions used to validate with 5' and 3' probes.
(DOCX)

S4 Table. Cdk5rap2 mutant mice used in experiments.
(DOCX)

S5 Table. Primer sequences for genotyping.
(DOCX)

S6 Table. PCR fragments expected size (bp).
(DOCX)

S7 Table. Primer and probe sequences for qPCR.
(DOCX)

S8 Table. Primer sequences for sequencing of human *CDK5RAP2*.
(DOCX)

S9 Table. Primer sequences for 5'-RACE.
(DOCX)

Acknowledgments

The authors thank Victor Tarabykin, Jessica Fassbender, Angelika Zwirner, Julia König, Pierre Gressens, Marta Rosario, Susanne Kosanke, Susanne Mueller, Pablo Hernaiz, Renate Wolf, and Horst von Bernuth for discussions and technical assistance.

Author Contributions

Conceived and designed the experiments: AMK ON NK SM. Performed the experiments: NK LIJ GN ER. Analyzed the data: NK LIJ GN ON AMK. Contributed reagents/materials/analysis tools: AMK ON. Wrote the paper: NK LIJ GN AMK ON.

References

1. Moynihan L, Jackson AP, Roberts E, Karbani G, Lewis I, Corry P, et al. (2000) A third novel locus for primary autosomal recessive microcephaly maps to chromosome 9q34. Am J Hum Genet 66: 724 –72710677332 PMID: 10677332
2. Bond J, Roberts E, Springell K, Lizarraga SB, Scott S, Higgins J, et al. (2005) A centrosomal mechanism involving CDK5RAP2 and CENPJ controls brain size. NatGenet 37: 353 –355
3. Mahmood S, Ahmad W, Hassan MJ (2011) Autosomal Recessive Primary Microcephaly (MCPH): clinical manifestations, genetic heterogeneity and mutation continuum. Orphanet J Rare Dis 6: 39. doi: 10.1186/1750-1172-6-39 PMID: 21668957
4. Kaindl AM, Passemard S, Kumar P, Kraemer N, Issa L, Zwirner A, et al. (2010) Many roads lead to primary autosomal recessive microcephaly. Prog Neurobiol 90: 363 –383. doi: 10.1016/j.pneurobio.2009.11.002 PMID: 19931588
5. Thornton GK, Woods CG (2009) Primary microcephaly: do all roads lead to Rome? Trends Genet 25: 501–510. doi: 10.1016/j.tig.2009.09.011 PMID: 19850369
6. Lizarraga SB, Margossian SP, Harris MH, Campagna DR, Han AP, Blevins S, et al. (2010) Cdk5rap2 regulates centrosome function and chromosome segregation in neuronal progenitors. Development 137: 1907–1917. doi: 10.1242/dev.040410 PMID: 20460369
7. Kraemer N, Ravindran E, Zaqout S, Neubert G, Schindler D, Ninnemann O, et al. (2015) Loss of CDK5RAP2 affects neural but not non-neural mESC differentiation into cardiomyocytes. Cell Cycle. doi: 10.1080/15384101.2015.1044169 PMID: 25942099

8. Barrera JA, Kao LR, Hammer RE, Seemann J, Fuchs JL, Megraw TL (2010) CDK5RAP2 regulates centriole engagement and cohesion in mice. Dev Cell 18: 913–926. doi: 10.1016/j.devcel.2010.05.017 PMID: 20627074
9. Farley FW, Soriano P, Steffen LS, Dymecki SM (2000) Widespread recombinase expression using FLPeR (flipper) mice. Genesis 28: 106–11011105051 PMID: 11105051
10. Nagy ZP (2003) Micromanipulation of the human oocyte. Reprod Biomed Online 7: 634–64014748960 PMID: 14748960
11. Issa L, Kraemer N, Rickert CH, Sifringer M, Ninnemann O, Stoltenburg-Didinger G, et al. (2013) CDK5RAP2 expression during murine and human brain development correlates with pathology in primary autosomal recessive microcephaly. Cereb Cortex 23: 2245–2260. doi: 10.1093/cercor/bhs212 PMID: 22806269
12. Fong KW, Choi YK, Rattner JB, Qi RZ (2008) CDK5RAP2 is a pericentriolar protein that functions in centrosomal attachment of the gamma-tubulin ring complex. Mol Biol Cell 19: 115–125. doi: 10.1091/mbc.E07-04-0371 PMID: 17959831

PLOS | GENETICS

RESEARCH ARTICLE

Homozygous *ARHGEF2* mutation causes intellectual disability and midbrain-hindbrain malformation

Ethiraj Ravindran[1,2,3☯], Hao Hu[4,5☯¤], Scott A. Yuzwa[6,7], Luis R. Hernandez-Miranda[8], Nadine Kraemer[1,2,3], Olaf Ninnemann[1], Luciana Musante[4], Eugen Boltshauser[9], Detlev Schindler[10], Angela Hübner[11], Hans-Christian Reinecker[12], Hans-Hilger Ropers[4], Carmen Birchmeier[8], Freda D. Miller[6,7], Thomas F. Wienker[4], Christoph Hübner[2], Angela M. Kaindl[1,2,3]*

1 Institute of Cell Biology and Neurobiology, Charité University Medicine Berlin, Berlin, Germany, **2** Department of Pediatric Neurology, Charité University Medicine Berlin, Berlin, Germany, **3** Sozialpädiatrisches Zentrum (SPZ), Center for Chronic Sick Children, Charité University, Berlin, Germany, **4** Max Planck Institute for Molecular Genetics, Berlin, Germany, **5** Guangzhou Women and Children's Medical Center, Guangzhou, China, **6** Department of Molecular Genetics, University of Toronto, Toronto, Canada, **7** Program in Neurosciences & Mental Health, Hospital for Sick Children, Toronto, Canada, **8** Max-Delbrück-Center for Molecular Medicine, Berlin, Germany, **9** Department of Pediatric Neurology, University Children's Hospital of Zurich, Zurich, Switzerland, **10** Department of Human Genetics, University of Würzburg, Würzburg, Germany, **11** Pediatrics, University Hospital, Technical University Dresden, Dresden, Germany, **12** Gastrointestinal Unit and Center for the Study of Inflammatory Bowel Disease, Massachusetts General Hospital, Harvard Medical School, Boston, Massachusetts, United States of America

☯ These authors contributed equally to this work.
¤ Current address: Guangzhou Women and Children's Medical Center, Guangzhou, China
* angela.kaindl@charite.de

OPEN ACCESS

Citation: Ravindran E, Hu H, Yuzwa SA, Hernandez-Miranda LR, Kraemer N, Ninnemann O, et al. (2017) Homozygous *ARHGEF2* mutation causes intellectual disability and midbrain-hindbrain malformation. PLoS Genet 13(4): e1006746. https://doi.org/10.1371/journal.pgen.1006746

Editor: Rudolf Korinthenberg, University Medical Center, GERMANY

Received: June 23, 2016

Accepted: April 5, 2017

Published: April 28, 2017

Data Availability Statement: All relevant data are within the paper and its Supporting Information files.

Funding: German Research Foundation (SFB665), the Sonnenfeld Stiftung, the German Academic Exchange Service (DAAD), the Berlin Institute of Health (BIH, CRG1), Charité, Max-Planck Society, EU FP7 project GENCODYS (241995), National Natural Science Foundation of China (No. 81671067), NIH AI113333, DK068181, and

Abstract

Mid-hindbrain malformations can occur during embryogenesis through a disturbance of transient and localized gene expression patterns within these distinct brain structures. Rho guanine nucleotide exchange factor (ARHGEF) family members are key for controlling the spatiotemporal activation of Rho GTPase, to modulate cytoskeleton dynamics, cell division, and cell migration. We identified, by means of whole exome sequencing, a homozygous frameshift mutation in the *ARHGEF2* as a cause of intellectual disability, a midbrain-hindbrain malformation, and mild microcephaly in a consanguineous pedigree of Kurdish-Turkish descent. We show that loss of *ARHGEF2* perturbs progenitor cell differentiation and that this is associated with a shift of mitotic spindle plane orientation, putatively favoring more symmetric divisions. The *ARHGEF2* mutation leads to reduction in the activation of the RhoA/ROCK/MLC pathway crucial for cell migration. We demonstrate that the human brain malformation is recapitulated in *Arhgef2* mutant mice and identify an aberrant migration of distinct components of the precerebellar system as a pathomechanism underlying the midbrain-hindbrain phenotype. Our results highlight the crucial function of ARHGEF2 in human brain development and identify a mutation in *ARHGEF2* as novel cause of a neurodevelopmental disorder.

DK043351 and Major Medical Collaboration and Innovation Program of Guangzhou Science Technology and Innovation Commission (No.201604020020). The funders had no role in study design, data collection and analysis, decision to publish, or preparation of the manuscript.

Competing interests: The authors have declared that no competing interests exist.

Author summary

During brain development, localized gene expression is crucial for the formation and function of specific brain regions. Various groups of proteins are known to regulate segmentation through controlled gene expression, among them, the Rho GTPase regulator family. In this study, we identified a frameshift mutation in the Rho guanine nucleotide exchange factor 2 gene (*ARHGEF2*) in two children presenting with intellectual disability, mild microcephaly, and a midbrain-hindbrain malformation. This phenotype is also observed in *Arhgef2* mutant mice, highlighting the importance of ARHGEF2 across development of distinct mammalian species. We show that loss of Arhgef2 affects neurogenesis and also cell migration. In addition, we extended the current knowledge of ARHGEF2 expression and its role in early central nervous system development, with special reference to the formation of the precerebellar system. In addition to extensive literature on ARHGEF2, we now provide evidence for its significant role in neuronal migration in brain development and link the gene to human neurodevelopmental disease.

Introduction

Brain development depends on spatiotemporally controlled gene expression.[1–3] Alterations in the expression pattern of such genes can result in neurodevelopmental disorders by impinging on key processes such as neural progenitor specification, cell division, and differentiation and the migration of newly born neurons from their site of origin to their final destination within the brain.[4–6] The latter is crucial for the formation of specific brain structures.[7–9] Factors that control localized gene function include Rho GTPase regulators. Here, we present evidence that the loss of function of Rho guanine nucleotide exchange factor 2 (ARHGEF2) causes a human neurodevelopmental disorder characterized by intellectual disability, mild microcephaly, and midbrain-hindbrain malformation.

ARHGEF2 (synonym GEF-H1, murine Lfc) catalyzes the replacement of GDP to GTP bound to Rho-related proteins and thereby controls timing and localization of the activation of Rho GTPases such as RhoA.[10–14] ARHGEF2 connects microtubule and actin cytoskeleton dynamics.[14] In this context ARHGEF2 activity is reduced through microtubule binding and further controlled by upstream regulators.[15–25] ARHGEF2 is key for actin and microtubule reorganization and is required for mitotic spindle formation and orientation.[11] Inhibition of ARHGEF2 results in spindle disorientation and dysfunction, mitotic delay, accumulation of prometaphase cells, and further mitotic aberrations.[11, 22] In mouse neocortex, *Arhgef2* is expressed in neural precursor and immature neurons and regulates neurogenesis from cortical precursor cells.[24] *Arhgef2* down-regulation by shRNA keeps radial precursors cycling, potentially by disrupted spindle plane orientation, and thereby inhibits neurogenesis. In contrast, *Arhgef2* overexpression causes an increase of neurons in the cortical plate.[24–26] Arhgef2 also plays a role in neural tube closure by regulating morphogenetic movements.[27] Furthermore, Arhgef2 participates in the migration of non-neuronal cells and in Wnt-induced planar cell polarity, via the activation of RhoA.[28, 29] Although evidence for a central function of Arhgef2 in cytoskeletal dynamics and critical signal transduction pathways exists and other ARHGEF genes have been linked with neurological disease,[30–32] little is known about ARHGEF2 function in humans and no disease phenotype associated with this gene has been reported.

Results and discussion

We report that patients with a homozygous mutation in *ARHGEF2* develop intellectual disability, mild microcephaly, and midbrain-hindbrain malformations. Two affected children of healthy, consanguineous parents of Kurdish-Turkish descent were born at term without complications after an uneventful pregnancy (II.1; II.2, Fig 1A). At birth, mild congenital microcephaly with occipitofrontal head circumferences (OFC) of -1.95 (II.1) and -2.33 (II.2) SDS (standard deviation score) but normal weight and height were apparent (S1 and S2 Tables). In addition, the two boys variously displayed wide intermamillary distance, broad fingers, low posterior hairline, and facial dysmorphism with long philtrum, thin upper lip, high palate, downslanted palpebral eye fissures, long eyelashes, bilateral ptosis, and horizontal pendular nystagmus (S1 Table). Ophthalmological examination revealed congenital strabismus, astigmatism, amblyopia (II.2), optic disc pallor (II.2), abnormalities of the retinal pigment epithelium (II.2), and abnormal visual-evoked potentials further underlining optic nerve affection. Motor milestones were not severely delayed despite generalized muscular hypotonia observed in patient II.1 and weak tendon reflexes in both children. Both children stumbled frequently and had a disturbance of fine motor movements (S3 Table). Moderate intellectual disability (IQ <50) and severe developmental speech delay despite normal hearing capacity were diagnosed in both patients (S1 and S3 Tables). Cranial magnetic resonance imaging (MRI) revealed mild microencephaly, elongated midbrain, hypoplasia of the pons, ventral and dorsal longitudinal clefts (grooves) in pons and medulla, and inferior vermis hypoplasia (Fig 1B). The finding of grooves and cerebellar hypoplasia (in absence of the 'dragonfly sign' with hypotrophy of the cerebellar hemispheres rather than of the vermis) argued against the differential diagnosis of pontocerebellar hypoplasia. Results of routine blood tests, extensive metabolic work-up, chromosome analysis, and cardiac function assessment were normal.

To identify the genetic cause of this disease, we performed whole exome sequencing and bioinformatic analysis followed by Sanger sequencing in both affected individuals. We thereby identified a homozygous deletion of a single guanine (G) at the exon12-intron12 boundary (Fig 2A and 2B), causing deletion of a G at the exon12-exon13 transition from normally spliced cDNA and ultimately a frameshift mutation in the affected children (c.1461delG, NM_004723.3, Fig 2C). The mutation lies within a highly conserved region, results in predicted truncation of the protein (p.D488T*fs**11, NP_004714.2, Fig 2D), and segregates with the disease phenotype, i.e., was heterozygous in both parents and not observed in healthy controls. We failed to detect the deletion in various whole exome databases and did not detect biallelic *ARHGEF2* mutations in six further patients, as detailed in the methods chapter. In lymphoblastoid cell lines (LCLs), generated from the patients, *ARHGEF2* mRNA levels were decreased as can be expected by partial nonsense-mediated decay (Fig 2E, n = 3, One-way ANOVA). Moreover, ARHGEF2 protein levels were virtually absent in patient cells and decreased to intermediate levels in cells from the heterozygous parents (Fig 2F, n = 3, One-way ANOVA). The predicted truncated form of ARHGEF2 protein was below detection levels in patient LCLs (S1 Fig), indicating the total loss of ARHGEF2 in patient cells.

To evaluate the biological effects of the identified *ARHGEF2* mutation on brain development, we utilized both *in vitro* and *in vivo* approaches. We used a well-characterized cell culture model of E13 mouse neocortical cells recapitulating the timing of cortical precursor differentiation observed *in vivo*.[24, 33, 34] The large majority of these cells are actively dividing radial glial precursors positive for the neural progenitor marker nestin immediately following plating. These cells then differentiate to generate excitatory neurons (DIV1-3) and subsequently astrocytes and oligodendrocytes (DIV5-7). We demonstrated previously, using

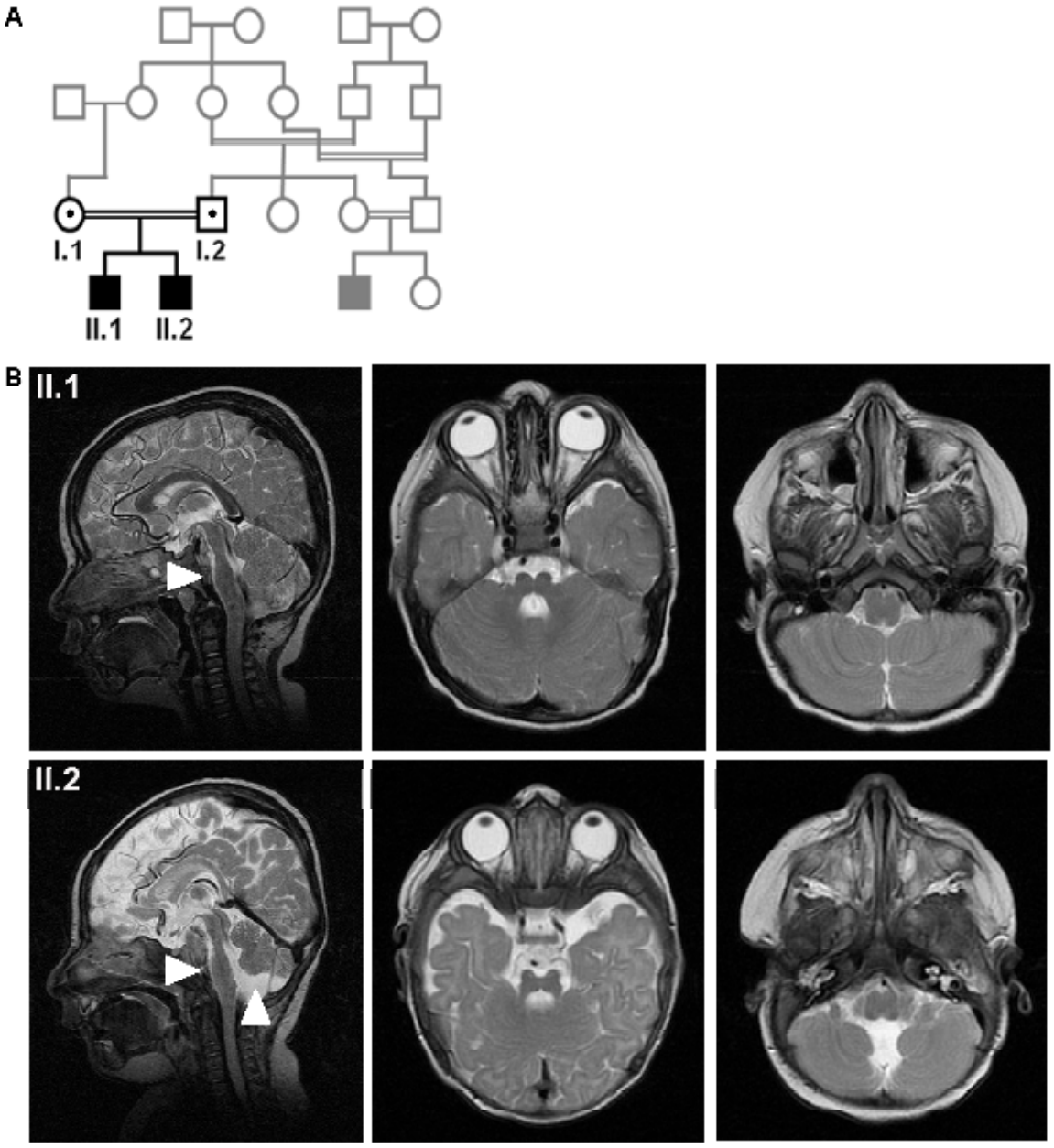

Fig 1. Phenotype of patients with midbrain-hindbrain malformation and intellectual disability. (**A**) The index patients are children (II.1, II.2) of healthy consanguineous Kurdish parents (first cousins) from Turkey. (**B**) Cranial MRI revealed microencephaly and hypoplasia of the pons and grooves (II.1, II.2) as well as hypoplasia of the cerebellum (II.2) or the caudal vermis (II.1). Arrow heads indicate hypoplastic pons (II.1, II.2) and cerebellum (II.2). Sagittal and axial T2 images.

https://doi.org/10.1371/journal.pgen.1006746.g001

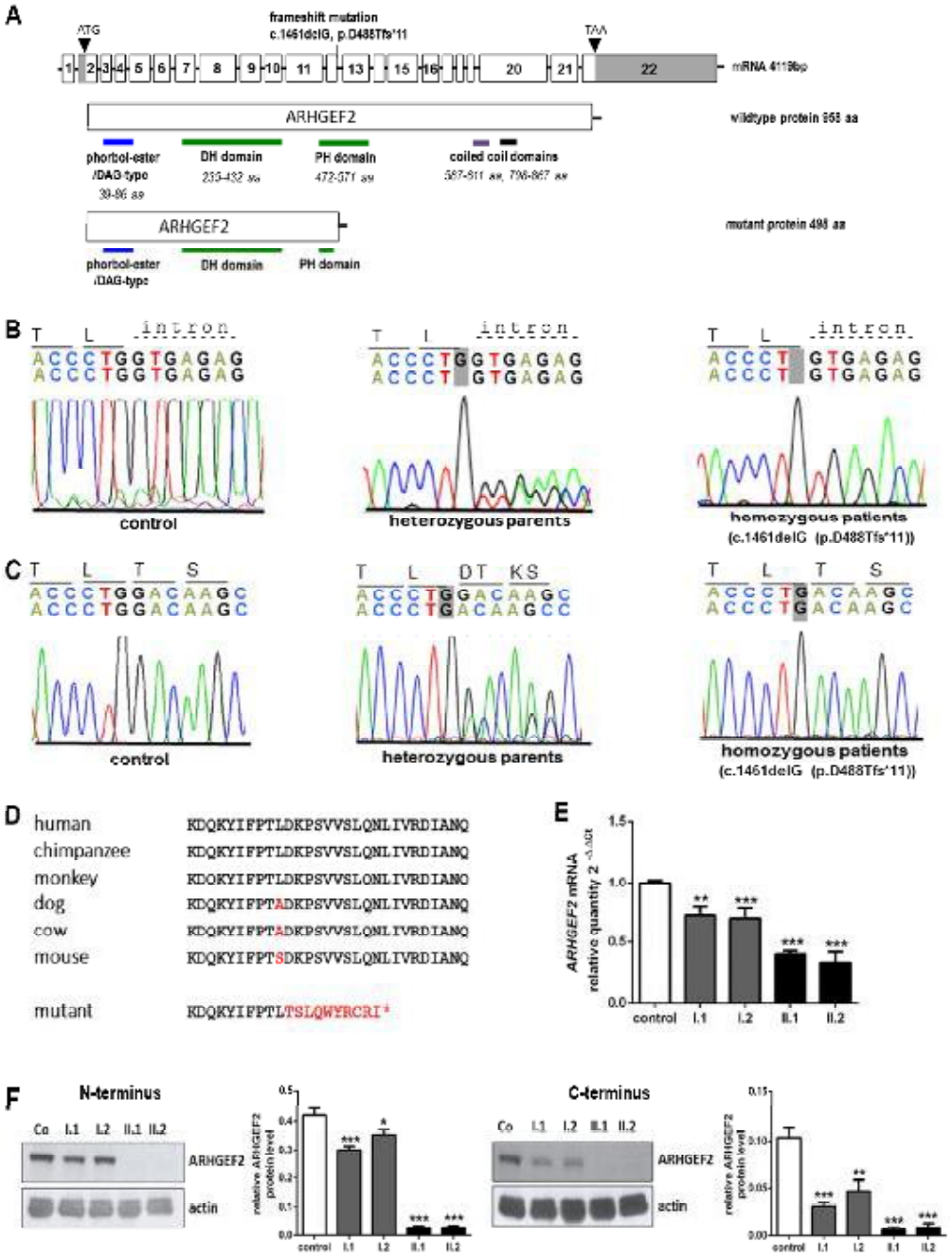

Fig 2. Homozygous *ARHGEF2* mutation in index patients. (**A**) By whole exome sequencing, the homozygous mutation c.1461delG (chr1:155,928,110delC, hg19) was identified in exon12-intron 12 boundary of the *ARHGEF2* (NM_004723.3). Pictogram representing ARHGEF2 protein domains (DH-DBL homology domain, PH-pleckstrin homology domain, phorbol-ester/Diacyl Glycerol-type zinc finger domain and coiled-coil domain) (**B**) Electropherogram depicting homozygous deletion of one base pair in the *ARHGEF2* in patient II.1, which is heterozygous in the healthy parents and normal in the healthy control.

(C) This mutation leads to a transfer of the neighboring C in the coding region into the splice donor site, as shown by cDNA sequencing. This is predicted to cause a frameshift mutation (p.D448T *fs**498, NP_004714.2) and a null allele. (**D**) The mutation lies within a highly conserved region of the protein. (**E**) Quantitative real-time PCR revealed strongly reduced *ARHGEF2* transcript levels in patients and intermediate levels in heterozygous parents, as would be expected from partial nonsense-mediated mRNA decay (n = 3, One-way ANOVA). (**F**) ARHGEF2 protein levels were below detection levels on a protein immunoblot of lymphoblastoid cells from the affected subjects compared to a control, with intermediate levels in heterozygous parents (ARHGEF2 120 kDa, actin 43 kDa; n = 3, One-way ANOVA). *p<0.05, **p<0.01, ***p<0.001, Error bars represent ± SD.

https://doi.org/10.1371/journal.pgen.1006746.g002

this model, that knockdown of *Arhgef2* causes a decrease in the proportion of βIII-tubulin positive neurons and a corresponding increase of cycling cortical precursors.[24] We thus expected the human *ARHGEF2* frameshift mutation to have a similar impact on neurogenesis, leading to an increase of cycling (and eventually apoptotic) precursors and a decrease of neurons generated during brain development. In a first series of experiments, we transfected murine cortical radial precursors with an *Arhgef2* shRNA plasmid and a nuclear EGFP reporter plasmid; the latter allows the visualization of transfected cells. As expected, *Arhgef2* knockdown significantly decreased the proportion of double positive cells for EGFP and early neuron marker βIII-tubulin, whereas it increased the proportion of EGFP and proliferation marker Ki67 double positive precursors (Fig 3A, n = 1378–1293 cells, One-way ANOVA). Next, we co-transfected cortical progenitors with the same combination of plasmids and an additional construct encoding for human wildtype *ARHGEF2*. In this condition, we observed no significant change in the proportion of EGFP and βIII-tubulin double positive cells or EGFP and Ki67 as compared to untransfected cells, demonstrating that wildtype ARHGEF2 rescues the phenotype produced by shRNA (Fig 3A). Last, we co-transfected cortical progenitors with *Arhgef2* shRNA, the EGFP reporter, and a construct encoding mutant *ARHGEF2* identified in the index patients. Here, the proportion of EGFP and βIII-tubulin double positive cells was reduced, whereas the number of EGFP and Ki67 remained increased (Fig 3A). We conclude that the phenotype produced by *Arhgef2* shRNA was rescued by coexpression of wildtype but not of mutant human *ARHGEF2*, consistent with the interpretation that the patient mutation is a loss-of-function mutation and that this *ARHGEF2* mutation impairs neurogenesis.

To further analyze whether the identified *ARHGEF2* loss-of function mutation affects brain development *in vivo* we *in utero* electroporated E13.5 mouse cortex with *Arhgef2* or *Con* (control) shRNA constructs along with wildtype or mutant human *ARHGEF2* plasmids as well as an EGFP vector. EGFP as a marker for electroporated cells and SatB2 as a marker for newborn neurons in murine cortices were quantified three days after electroporation. We identified a pronounced increase in the proportion of EGFP-positive cells in the ventricular, sub-ventricular, and intermediate zones (VZ/SVZ/IZ) and decreased proportions in the cortical plate (CP) of the *Arhgef2* shRNA electroporated mice, as compared to mice that were electroporated with the EGFP reporter only (Fig 3B and 3C). In line with our *in vitro* data, overexpression of wildtype, but not mutant, *ARHGEF2* was able to effectively rescue the cell distribution in the cortex induced by *Arhgef2* shRNA. Upon electroporation of *Arhgef2* shRNA, we additionally observed a dramatic reduction in the proportion of SatB2/EGFP double positive cells localized to the cortical plate. This is consistent with impaired neurogenesis described above in cultured cortical precursor cells. Overexpression of wildtype *ARHGEF2* was able to rescue this impairment of neurogenesis while mutant *ARHGEF2* was ineffective (Fig 3B and 3C, n = 3, One-way ANOVA). These data further confirm that the patient mutation in human *ARHGEF2* acts as a loss-of-function mutation also *in vivo*, results in dramatically decreased neurogenesis and is most probably disease-causative (Fig 3D).

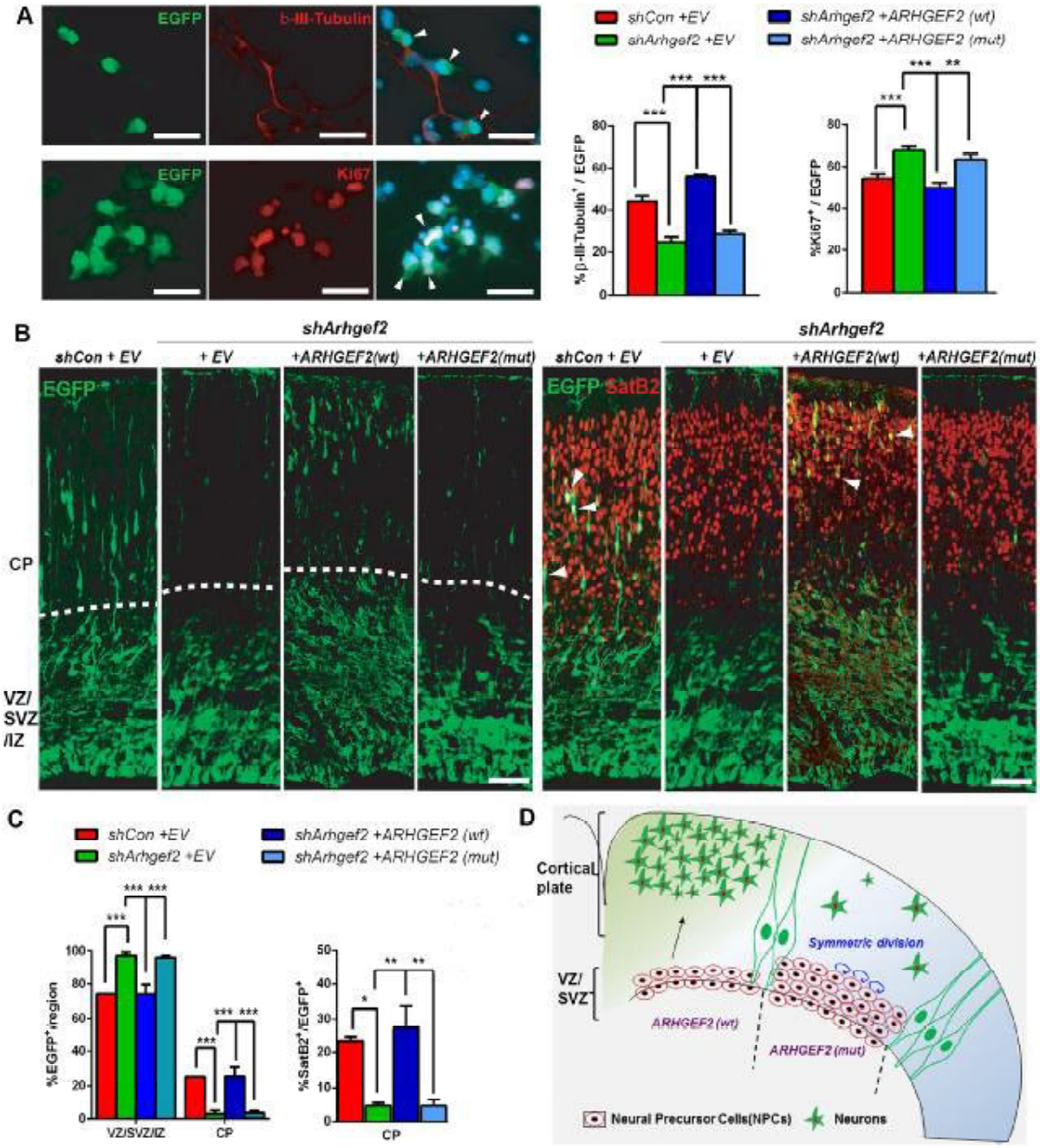

Fig 3. Loss of ARHGEF2 function inhibits neurogenesis and increases neural precursors *in vitro* and *in vivo*. (A) Cultured mouse cortical precursor cells were transfected with mouse *Arhgef2* shRNA (*shArhgef2*) or scramble shRNA (*shCon*), with a nuclear EGFP plasmid and with either an empty vector (EV), wildtype (wt) or mutant (mut) human *ARHGEF2*. Representative fluorescence micrographs of *shArhgef2* knockdown cultured precursors immunostained for EGFP (green), βIII-tubulin or Ki67 (red), and Hoechst 33258 nuclear staining (blue) 3 days after transfection; right panels show the merged images; arrowheads indicate double-positive cells. The *Arhgef2* shRNA-induced phenotype of decreased early neuronal marker βIII-

tubulin-positive cells and increased proliferation marker Ki67-positive precursors is rescued by *ARHGEF2* (wt) but not *ARHGEF2* (mut) (n = 1378–1293 cells in 4 independent experiments, One-way ANOVA, scale bar 25 μm). **(B, C)** Quantification of EGFP positive cells and SatB2/EGFP double-positive cells (arrowheads) in E13.5 mouse cortices co-electroporated with plasmids specified above and analyzed 3 days later. Representative fluorescence micrographs of sections co-stained for SatB2 (new-born neurons) and EGFP (dotted line indicates boundary between CP and VZ/SVZ/IZ) (n = 3, One-way ANOVA, scale bar 50 μm). **(D)** Pictorial representation: ARHGEF2 favors neurogenesis and its downregulation/dysfunction inhibits neurogenesis by maintaining murine NPCs in cycling phase. *p<0.05, **p<0.01, ***p<0.001. Error bars represent ± S.E.M.

https://doi.org/10.1371/journal.pgen.1006746.g003

ARHGEF2 has been associated previously with spindle plane orientation,[11, 24] and the latter has been shown to play a crucial role for the fate of neuronal precursors, 'deciding' between self-renewal and differentiation.[35] To evaluate whether human mutant *ARHGEF2* alters neurogenesis by impairing mitotic spindle orientation, we performed *in utero* electroporation with the experimental setup described above and determined spindle plane orientation. We determined the angle between the ventricular surface and a line connecting centrosomes in metaphase/anaphase cells in brain sections. *Arhgef2* shRNA led to a significant shift of the spindle orientation towards a more horizontal orientation, characterizing putatively more symmetrically, self-renewing cell divisions. Again, overexpression of human wildtype but not mutant *ARHGEF2* was able to rescue significantly this phenotype (Fig 4A, n = 68–70 cells from 3–4 mice, One-way ANOVA). In the developing brain, ARHGEF2 reportedly controls the arrangement for symmetric or asymmetric cell divisions of apical progenitors through plane orientation.[24] Given our results from overexpressing mutant *ARHGEF2* in the mouse brain, we concluded that loss of ARHGEF2 activity inhibits neurogenesis by favoring more symmetric divisions of neocortical progenitors (Fig 4B).

To further substantiate the effect of a loss of ARHGEF2 functions in human tissues and other cell types, we analyzed cell cycle apparatus in LCLs from our index patients and healthy controls. We detected an abnormal morphology of the mitotic spindle apparatus, decreased spindle pole distance, and decreased cell size in LCLs derived from the patients compared to controls, significantly (Fig 5A and 5B, n = 100–200 cells, One-way ANOVA). There was, however, no cell cycle defect, increased radiosensitivity, nor abnormal centrosome 'morphology' in the patient LCLs (S2 and S3 Figs). We concluded that regulation of the mitotic spindle apparatus is a primary function of ARHGEF2 in the cell cycle also in human tissues and other cell types.

ARHGEF2 regulates various cellular processes through activation of Rho family GTPases, specifically RhoA and its downstream effectors, such as RhoA/ROCK/MLC pathway members.[12, 22, 28, 36, 37] Specifically, RhoA has been implicated in the regulation of neurogenesis and planar cell divisions.[38, 39] We thus analyzed the activity of RhoA and its immediate downstream effectors in patient and control LCLs. We detected a significant reduction of active RhoA and, consistently, reduced levels of active phospho-myosin light chain (MLC) in the LCLs of affected individuals with an *ARHGEF2* mutation compared to healthy individuals (Fig 5C–5E, n = 3, One-way ANOVA). This indicates that the RhoA/ROCK/MLC pathway is most likely impaired in humans with the *ARHGEF2* mutation.

Previous studies showed that *Arhgef2* is expressed in the neural tube of mice from embryonic day 11 on and maintained at high levels during brain development.[24] Our *in situ* hybridization studies on embryonic mice showed strong expression of *Arhgef2* transcripts in the neuroepithelium of telencephalon, diencephalon, and rhombencephalon of E11 mice (S5 Fig). At the time of birth, *Arhgef2* is maintained in the germinal zones of both the neocortex and the cerebellum, as well as in the pontine gray nuclei (PGN) (S5 Fig). To further corroborate the pathogenicity of the identified *ARHGEF2* mutation in brain development, we analyzed the phenotype of *Arhgef2* deficient mice.[40] In adult *Arhgef2* mutant mice, we observed a significant reduction in volume of the total brain size (referred to as microencephaly), the

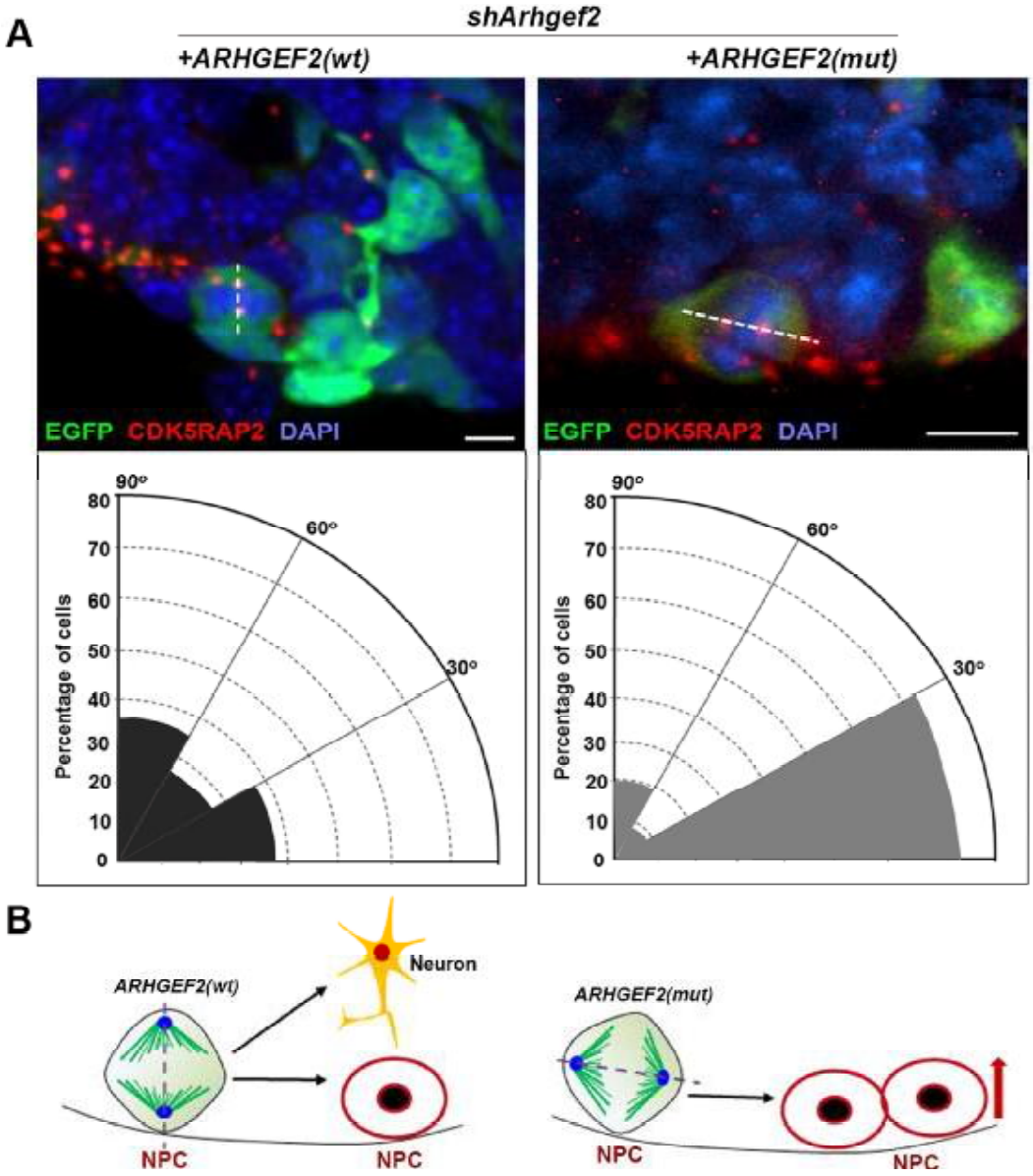

Fig 4. Mutant *ARHGEF2* favors self-renewing (symmetric) precursor proliferation. (A) Quantification of spindle plane orientation of dividing, metaphase and anaphase precursors transfected with EGFP (n = 68–70 cells, Student's *t-test*, scale bar 20 μm). *Arhgef2* shRNA is associated with a more horizontal orientation of the spindle pole. Overexpression of *ARHGEF2* (wt), not *ARHGEF2* (mut), rescues the spindle orientation phenotype in dividing precursors. Representative fluorescence micrographs of sections stained with CDK5RAP2 (centrosomes), DAPI, and EGFP, indicating the plane of division (dotted line) and respective radial diagram. **(B)** Model indicating the plane of symmetry and cell fate decision in the developing brain. *p<0.05. Error bars represent ± S. E.M.

https://doi.org/10.1371/journal.pgen.1006746.g004

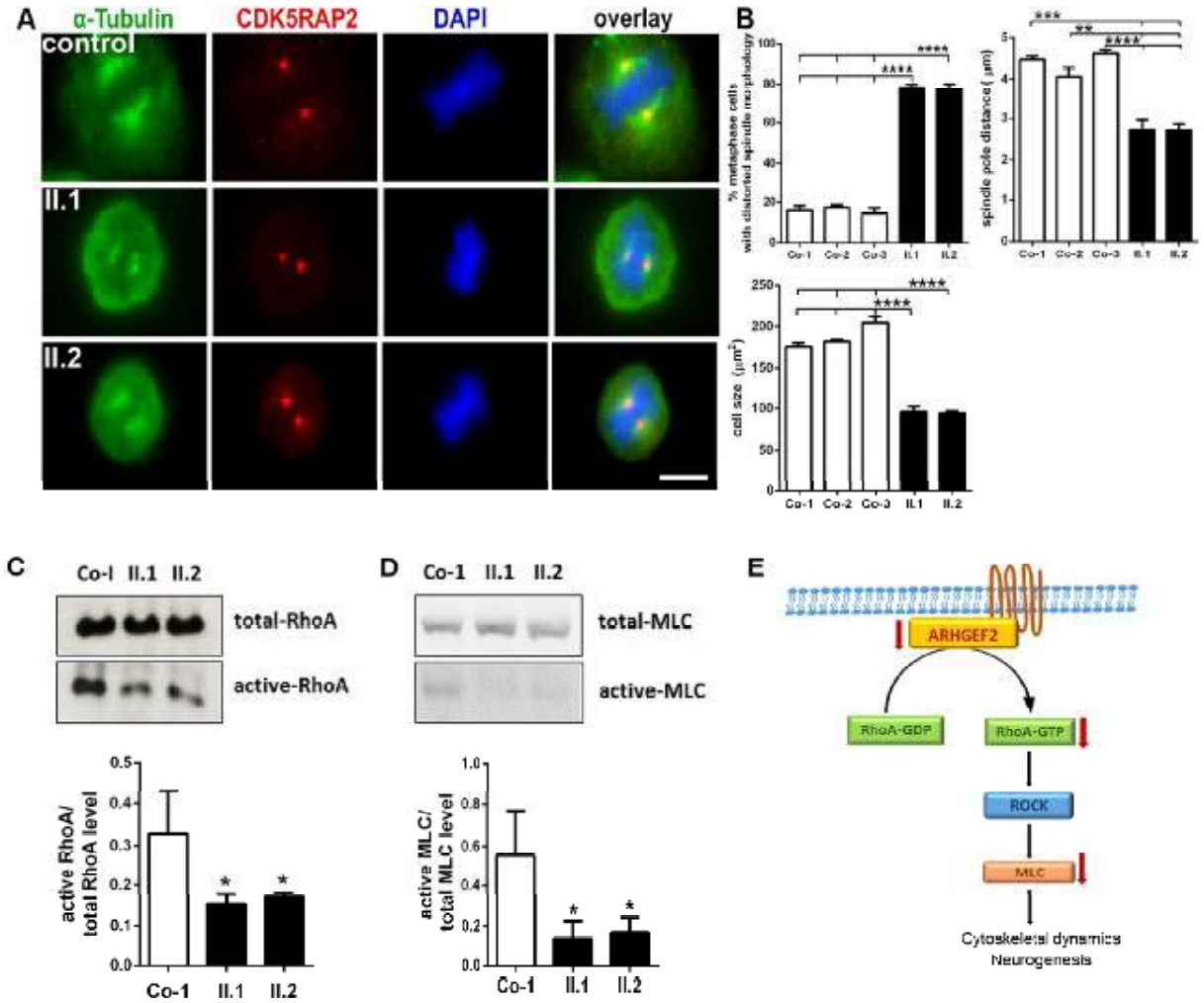

Fig 5. Mitotic spindle defects and reduced RhoA activation in LCLs of index patients with *ARHGEF2* mutation. (**A**) Abnormal spindle formation with an increase of abnormal misdirected spindles and broad, unfocused microtubules poles in immortalized patient II.1 and II.2 lymphocytes (LCLs, metaphase cells only of patient II.1 and II.2 are shown, centrosome marker CDK5RAP2 (red), spindle marker α-tubulin (green), DNA was stained with DAPI (blue)). CDK5RAP2 signals did not differ significantly between patient and control cells; this holds also true for the centrosome marker γ-tubulin (S3 Fig). (**B**) Quantification results underlining abnormal spindle morphology, decreased spindle pole distance, and reduced cell size of patient versus control LCLs (n = 100–200, One-way ANOVA, scale bar 5 μm): abnormal spindle morphology in patients (II.1 77%, II.2 78%) versus controls (Co-1 16%, Co-2 17%, Co-3 14%), decreased spindle pole distance in patients (II.1 2.70, II.2 2.72 μm) versus controls (Co-1 4.46, Co-2 4.05, Co-3 4.61 μm), and reduced cell size in patients (II.1 96.14, II.2 94.66 μm^2) versus controls (Co-1 175.52, Co-2 181.74, Co-3 204.51 μm^2). We observed no difference in size or proliferation of T-cells between *Arhgef2-/-* and *Arhgef2+/+* mice (S4 Fig). (**C, D**) Reduced levels of active RhoA and active MLC in patient LCLs in protein immunoblots (n = 3, One-way ANOVA). (**E**) Pictogram of RhoA/ROCK/MLC pathway downstream of ARHGEF2, important for processes such as cytoskeletal dynamics and neurogenesis. *p<0.05, **p<0.01, ***p<0.001, ****p<0.0001. Error bars represent ± SD.

https://doi.org/10.1371/journal.pgen.1006746.g005

cerebellum and the brainstem, as well as the striking absence of the pontine nuclei (Fig 6, n = 3–4, Student's *t-test*). We concluded that the phenotypes observed in the nervous system of *Arhgef2* deficient mice recapitulate largely those malformations observed in the index patients. Our results showed a clear correspondence between regions displaying high levels of

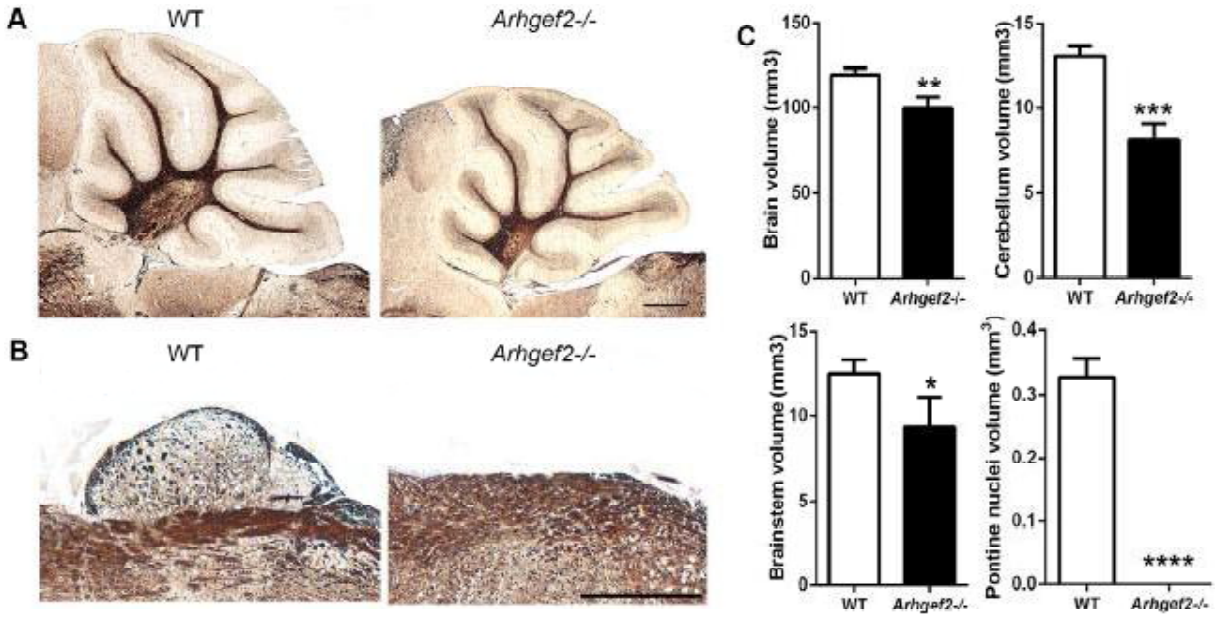

Fig 6. *Arhgef2-/-* mutant mice display microencephaly, cerebellar hypotrophy and lack pontine nuclei. (A, B) Reduced cerebellar size and lack of pontine nuclei in adult *Arhgef2* mutant mice compared to wild type littermates (Gallyas staining, DIC images, scale bar 500 μm). **(C)** Quantification underlines significant reduction of whole brain, cerebellum, brain stem, and pontine nuclei volume in mutant versus wild type brains (n = 3–4, Student's *t-test*; *p<0.05, **p<0.01, ***p<0.001, ****p<0.0001. Error bars represent ± SD).

https://doi.org/10.1371/journal.pgen.1006746.g006

Arhgef2 expression and those pathologically affected in the index patients with *ARHGEF2* mutation.

To gain further insight in the function of *ARHGEF2* in brain development, we set out to analyze the cerebral cortex, midbrain, cerebellum, and hindbrain of *Arhgef2* mutant mice. First, no drastic anatomical abnormality was found in the neocortex of *Arhgef2* mutant mice, as assessed by the measurement of its volume, thickness, and surface area (S6 Fig). Though it should be noted that there was a trend towards a reduction in the analyzed parameters in the mutant mice, which could contribute to the mild microcephaly phenotype observed in *Arhgef2* mutant mice. Similarly, no major alteration on the distribution of neurons in the cortical layers was found in *Arhgef2* mutant mice (S6 Fig). Next, we analyzed the integrity of midbrain structures by immunostaining the inferior and superior colliculus with antibodies against the transcription factor FoxP2. This revealed no significant alteration in development of midbrain structures in *Arhgef2* mutant mice (S7 Fig).

To address the cerebellar phenotype observed in *Arhgef2* mutant mice and patients, we measured the size of Purkinje cells and the thickness of the cerebellar molecular layer in *Arhgef2* mutant and control mice. Our analysis revealed no significant difference in these parameters between wildtype and mutants (S8 Fig). This led us to hypothesize that the input to the cerebellum, from precerebellar nuclei, could be affected, and thus contributing to the observed reduction of the cerebellar size. During hindbrain development, precerebellar neurons emerge from the proliferative neuroepithelium of the rhombic lip and migrate tangentially to reach their final destinations in the pons and medulla. These neurons form five distinct nuclei that are located at different positions within the hindbrain: pontine gray nuclei (PGN), reticulotegmental nuclei

(RTN), external cuneate nuclei (ECN), lateral reticular nuclei (LRN), and inferior olivary nuclei (IO) [41–44]. The PGN, RTN, ECN, LRN projects mossy fibers to the cerebellum, whereas IO projects climbing fibers, and thereby provide input to the cerebellum.[41–44] To tackle the hypothesis that deficits in development of precerebellar nuclei result in abnormalities in cerebellar size of *Arhgef2* mutant mice, we immunostained sagittal and coronal sections taken from *Arhgef2* homozygous and *Arhgef2* heterozygous (used as control) mice with antibodies against the transcription factor Mbh2 (which labels PGN, RTN, ECN, LRN) and FoxP2 (that marks IO). This analysis revealed that *Arhgef2* mutant mice completely lack, in addition to PGN, the RTN and have a severe reduction in LRN neurons (Figs 7A, 7B, 7D, 8A, 8B and 8D). Interestingly, the rostral part of the ECN was abnormally enlarged in *Arhgef2* mutant mice when compared to controls, suggesting that some PGN, RTN and LRN might fail to migrate to their ventral positions and aberrantly locate in the ECN (Figs 7C, 8C and 8D). The formation of the IO was not obviously disturbed in *Arhgef2* mutant mice (Fig 7D). Taken together, our anatomical analysis revealed that specific precerebellar nuclei are either absent or severely reduced in *Arhgef2* mutant mice.

These findings draw our attention to two possible interpretations on the role of Arhgef2 in development of precerebellar nuclei: (1) Arhgef2 modulates the generation of precerebellar neurons and/or (2) Arhgef2 regulates the migration of these cells from their progenitor niche towards their final localization. Precerebellar neurons arise from discrete progenitor domains located in the developing dorsal hindbrain, which are defined by the combinatorial expression of the transcription factor Olig3 with other bHLH (basic Helix-Loop-Helix) transcription factors, such as Atoh1 (Protein atonal homolog 1) or Ptf1a (Pancreas transcription factor 1 alpha).[45] Precerebellar neurons that form the PGN, RTN, LRN and ECN are generated from Olig3/Atoh1 positive (known as dA1) progenitors, whereas those that form the IO emerge from Olig3/Ptf1a positive (known as dA4) progenitors,[46, 47] reviewed in [45]. Arhgef2 is unlikely to modulate generation of precerebellar neurons as its transcript becomes expressed only by E11 in mice, a time point when these cells have already been specified and have started their migration. We thus speculated that Arhgef2 rather modulates precerebellar neuron migration. To test this possibility, we co-stained transverse hindbrain sections, taken from wildtype mice at E11, with an *Arhgef2 in situ* hybridization probe and antibodies against Olig3 and Mbh2 (BarH-like homeobox 1). This revealed that *Arhgef2* is co-expressed largely with Mbh2-positive cells emanating from dA1 progenitors and throughout the anterior and posterior extramural streams precerebellar neurons in the mantle zone of hindbrain (S9 Fig). *Arhgef2* does not follow the expression pattern of Olig3 in dorsal hindbrain (S9 Fig). It is interesting to note that mutation of *Arhgef2* appears to selectively affect the migration of dA1-derived neurons, as other hindbrain centers such as the nucleus of the solitary tract (a Olig3 +/Ascl1+ dA3 derivative) or the IO (dA4 derivative) were not affected (Figs 7E and 8E).

This report demonstrates that intellectual disability, mild microcephaly, and a midbrain-hindbrain defect can be caused by a homozygous mutation of the *ARHGEF2* in humans. We highlight the importance of *ARHGEF2* during brain development and, in particular, in neuronal progenitor cell division and differentiation, as well as in neuronal migration. We show that in both human and murine cells *ARHGEF2* deficiency interferes with the normal orientation of mitotic spindles and cell fate choices. As expected, the frameshift mutation of *ARHGEF2* deregulates the activity of its downstream effectors, i.e. the RhoA/ROCK/MLC pathway. ARHGEF2 thereby joins other members of the same protein family that have already been associated with neurologic disease such as non-syndromic intellectual disability (*ARHGEF6*),[30] epileptic encephalopathy (*ARHGEF9*),[31] and peripheral demyelinating neuropathy (*ARHGEF10*).[32] We show that *Arhgef2* deficiency in mice severely impairs the migration of dA1 progenitors, which results in the incorrect location of precerebellar neurons in the

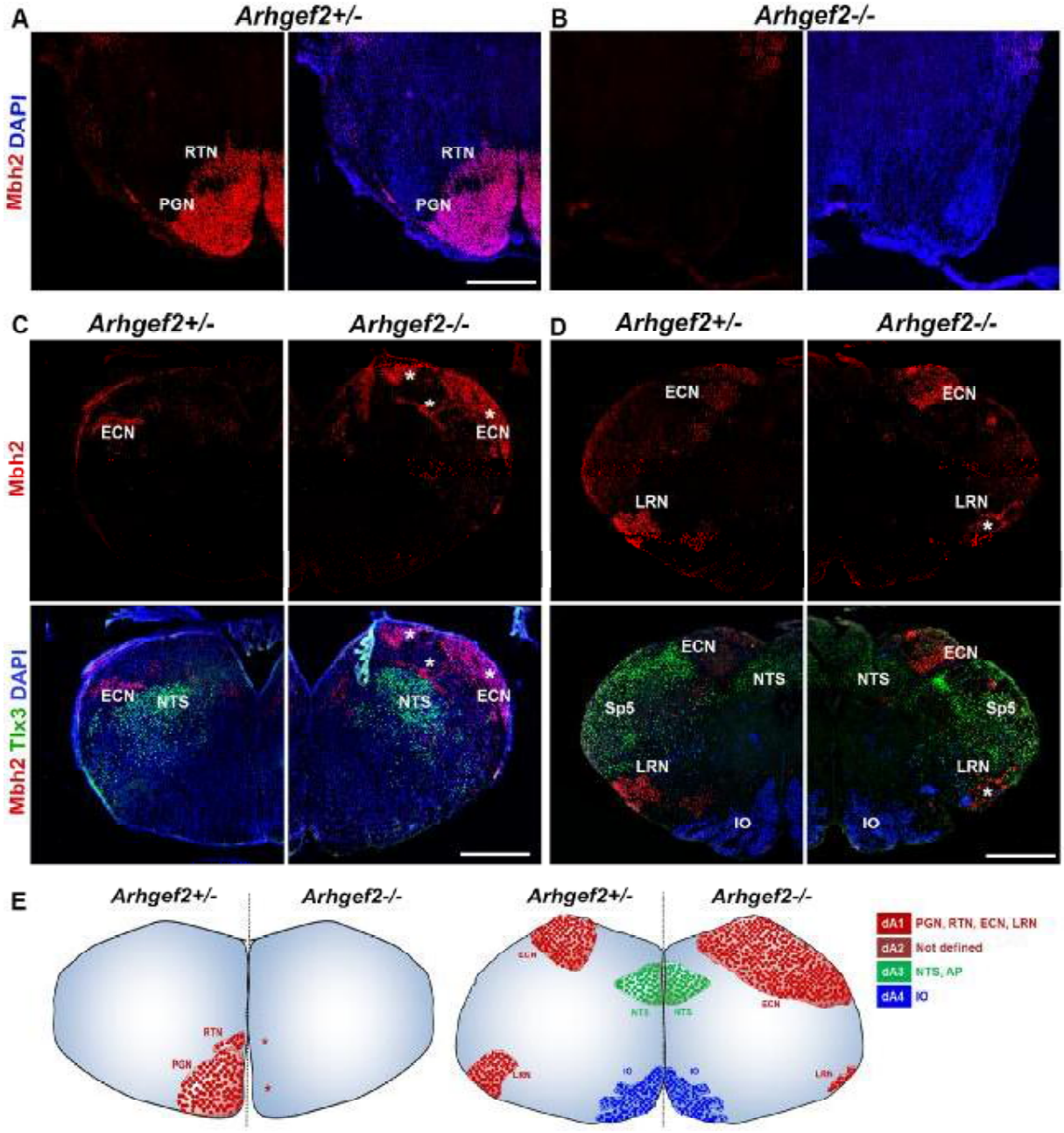

Fig 7. Loss of Arhgef2 affects the formation of precerebellar nuclei of dA1 derivatives. Representative fluorescence micrographs of coronal hindbrain sections of *Arhgef2-/-* and *Arhgef2+/-* (used as controls) mice, stained with precerebellar neuronal marker Mbh2 (red), Tlx3 (green), and DAPI (n = 3, scale bar 300 μm). **(A, B)** *Arhgef2-/-* mouse brains lack PGN and RTN present in *Arhgef2+/-* mouse brains. **(C)** In the rostral medulla of *Arhgef2-/-* mice, the ECN is abnormally enlarged and distributed (indicated by stars) when compared to *Arhgef2+/-* mice. **(D)** The LRN in the caudal medulla is significantly reduced in size (indicated by stars) in *Arhgef2-/-* mice compared to *Arhgef2+/-* mice, whereas the IO and NTS are unaffected. **(E)** Pictogram depicting the abnormal formation of dA1-derived precerebellar nuclei (red) and normal formation of dA3 (green) and dA4 (blue) nuclei in the *Arhgef2-/-* mice brain in comparison to the *Arhgef2+/-* control condition. Abbreviations: PGN-pontine gray nuclei, RTN-reticulotegmental nuclei, ECN-external cuneate nuclei, LRN-lateral reticular nuclei, IO-inferior olivary nuclei, NTS-nucleus of the solitary tract, Sp5-spinal trigeminal nuclei, AP-area postrema, dA-class A neurons.

https://doi.org/10.1371/journal.pgen.1006746.g007

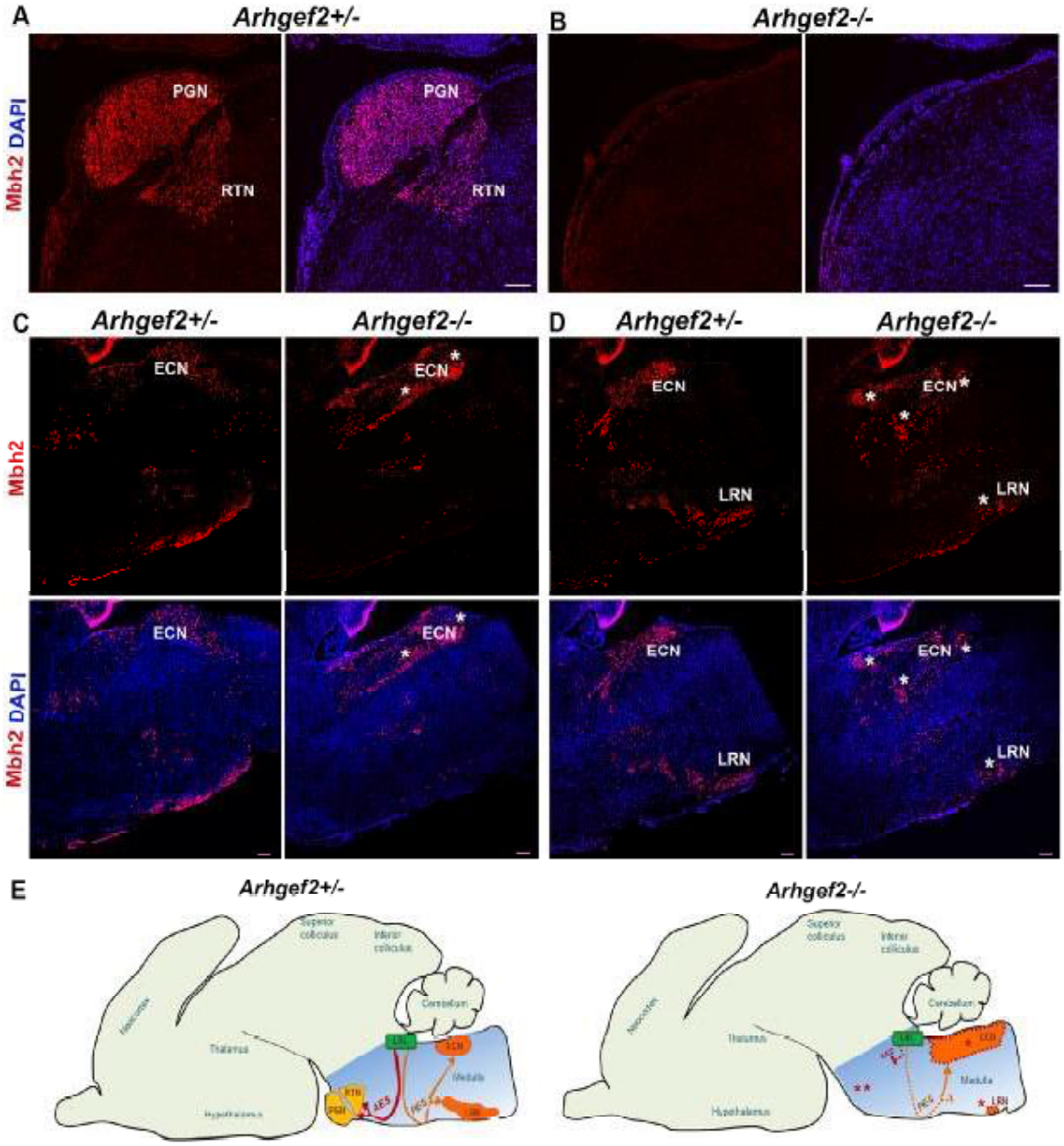

Fig 8. *Arhgef2-/-* mutant mice exhibit perturbed migration of precerebellar neurons. Sagittal hindbrain sections of *Arhgef2-/-* and *Arhgef2+/-* mice stained for precerebellar neurons with Mbh2 in red (n = 3, scale bar 100 μm, nuclei stained with DAPI (blue)). **(A, B)** PGN and RTN formed through AES migratory stream is absent in *Arhgef2-/-* and present in *Arhgef2+/-* mouse brains. **(C, D)** The disturbed PES migratory stream in the *Arhgef2-/-* mice is associated with the formation of enlarged ECN and smaller LRN compared to those in *Arhgef2+/-* mice. **(E)** Pictogram illustrating the normal formation of PGN and RTN via the AES migratory stream (red) and LRN and ECN via the PES migratory stream (orange) from the lower rhombic lip (LRL) in the mouse brain. In the *Arhgef2-/-* brain, AES and PES streams are disturbed (represented by dotted lines), culminating in abnormal migration and accumulation of precerebellar neurons. Abbreviations: PGN-pontine gray nuclei, RTN-reticulotegmental nuclei, ECN-external cuneate nuclei, LRN-lateral reticular nuclei, LRL-lower rhombic lip.

https://doi.org/10.1371/journal.pgen.1006746.g008

hindbrain of *Arhgef2* mutant mice. In keeping with our data, previous studies have shown that deficits in the RhoA/ROCK pathway affect migration of precerebellar neurons.[48] Thus, increasing evidence support the notion that the ARHGEF2-RhoA/ROCK pathway is essential for the migration and specification of precerebellar neurons. ARHGEF2 has been shown to be involved in Wnt-mediated planar cell polarity pathway through its interaction with the Daam and Dishevelled proteins, which are known to control migratory events. *Wnt1* mutant mice have been reported to have a midbrain-hindbrain malformation,[49] and humans with biallelic *WNT1* mutations displayed cerebellum and brainstem phenotype.[50] It is interesting to note that the major effects in the hindbrain of *Arhgef2* mutant mice occur in the migration of dA1-derived neurons, but not other neuronal cell types that emerge from neighboring progenitor domains. Our data demonstrate thus a marked specificity in the molecular control of neuronal migration in the hindbrain. The combined midbrain-hindbrain malformation phenotype observed in humans was not fully recapitulated in *Arhgef2* deficient mice, which lacked an obvious midbrain phenotype. This suggests that during evolutionary divergence of these species, additional molecular mechanisms coordinate the function of ARHGEF2. Identifying additional families with *ARHGEF2* mutations will help to consolidate the disease-causative role of ARHGEF2 in humans.

Materials and methods

Ethics statement

The human study was approved by the local ethics committees of the Charité (approval no. EA1/212/08), and the written consent form was received from the investigated individuals. All animal experiments were carried out in accordance to the guidelines of national ethic principles, and approved by Charité (registration no. T0344/12).

Genetic analyses

DNA samples of the two affected individuals were subjected to whole exome sequencing. Five μg genomic DNA were enriched with the Agilent Human All Exon V3 kit (Agilent, Santa Clara, CA, USA) following the manufacturer's protocol. The libraries were sequenced using Illumina HiSeq 2000 sequencer for single-end 101 bp. Coverage of coding regions was >92.6–93.4% with a minimal depth of 20-fold; the raw data were processed as described previously.[51] In brief, the raw sequences were aligned to human reference genome (hg19), and the alignment results were used to call variants of SNVs, indels, and CNVs. We defined from the exome data the regions of homozygosity by at least four high-quality (genotype quality $\geq$ 20, allele counts $\geq$ 10, and allele percentage $\geq$ 0.9) consecutive homozygous SNVs uninterrupted by heterozygous SNVs. The overlapping regions of homozygosity (>1 Mb) between the two patients were listed in S4 Table. Subsequently, the variants were screened by known causal mutation databases (OMIM and HGMD), and polymorphism databases (1000Genome, ESP6500, dbSNP138, and an in-house exome database with 721 individuals of whom >90% are of the Middle East origin) with matching variants not exceeding the prevalence cutoff of 0.5%, and the pathogenicity of variants was further evaluated (analysis pipeline: https://sourceforge.net/projects/merap/). Sanger sequencing of the *ARHGEF2* (NM_004723.3) in our cases was performed to confirm the mutation in the patients, establish the genotype in the other family members, and evaluate the presence of potential mutations in additional six consanguineous pedigrees of Sri Lankan, Italian and Turkish descent with developmental delay and a similar radiological phenotype of pontine and cerebellar hypoplasia. Some of these patients also had facial dysmorphism, ataxia, autism, epilepsy, and further MRI findings including a migration or myelination defect. The healthy status of heterozygous parents argues

against a haploinsufficiency mechanism underlying this disease phenotype. Two patients with heterozygous deletions encompassing the *ARHGEF2* are listed in the Decipher database: (i) patient 276515 (https://decipher.sanger.ac.uk/patient/276515; 2.76 Mb deletion covering 59 genes; arr 1q22;q23(155,296,964–158,056,876)) with abnormal facial features, intellectual disability, and speech delay and (ii) patient 255240 (https://decipher.sanger.ac.uk/patient/255240; 0.92 Mb deletion spanning 24 genes; arr 1q22(155,192,986–156,108,069)) with facial dysmorphism, brachydactyly, intellectual disability, severe speech delay, muscular hypotonia, but normal cMRI findings.

Apart from the *ARHGEF2* candidate variant, there were three further homozygous variants shared by the two patients that we ranked as unlikely disease-causing: (i) *EXTL1* (NM_004455, exostosin-like glycosyltransferase 1), g.1:26356156G>A, c.939G>A, p.W313X. However, there were 16 heterozygotes in the ESP6500 database and one healthy individual in our in-house database with a homozygous variant. (ii) *HMCN1* (NM_031935, hemicentin 1), g.1:186010193G>A, c.6229G>A, p.D2077N. However, this gene has been reported to be associated with macular degeneration, a phenotype that does not fit the clinical features of our index patients. (iii) *IGFN1* (NM_001164586, immunoglobulin-like and fibronectin type III domain containing 1), g.1:201193885G>A, c.10369G>A, p.G3457S. However, there were 7 heterozygotes in the ESP6500 database, and this variant has a prediction score from SIFT (tolerated) and PolyPhen2 (possibly damaging) that makes it unlikely as well as a GERP conservation score of merely 1.101.

Because both patients were male, we checked on the X chromosome for hemizygous variant, but detected no rare deleterious variant shared by the two individuals.

Epstein-Barr virus-transformed LCLs

LCLs were established and cultured according to the protocol published by Neitzel et al. 1986. [52]

Quantitative real-time PCR (qPCR)

RNA extraction and cDNA synthesis were performed with established methods reported previously.[53] To specifically amplify and detect *ARHGEF2* and *RPII* (RNA polymerase II, reference gene) cDNA, we designed sets of primers using the Primer3 online software (www.primer3.ut.ee). qPCR experiments were run in triplicate using Maxima SYBR Green/ROX qPCR Master Mix (Thermo Scientific, Braunschweig, Germany) according to the manufacturer's protocol with primers specified in S5 Table. Quantification was performed as described previously,[53] and statistical calculations were performed on GraphPad Prism 5 Software (GraphPad Software Inc., La Jolla, CA, USA).

Western blot

Protein extraction and Western blots (run in triplicates) were performed with established methods reported previously;[54] antibodies are listed in S6 Table.

Immunocytology

LCLs briefly plated on poly-L-lysine (Sigma-Aldrich, Taufkirchen, Germany) -coated coverslips were fixed in 4% PFA. Coverslips were further incubated in staining buffer (0.2% gelatin, 0.25% Triton X-100, 10% donkey normal serum) for 30 min for permeabilization and blocking, followed by overnight incubation with primary antibodies and an 2 h incubation with the corresponding secondary antibodies (antibodies listed in S6 Table). Nuclei were labeled with

4',6-Diamidino-2-phenylindole (DAPI, 1:1000, Sigma-Aldrich). Fluorescently labeled cells were analyzed and imaged using a fluorescent Olympus BX51 microscope with the software Magnafire 2.1B (2001) (Olympus, Hamburg, Germany), and images were processed using Adobe Photoshop and ImageJ.

Cell cycle analysis

Peripheral blood lymphocytes (PBL) were isolated from heparinized blood samples by Ficoll density gradient centrifugation. DNA damage was introduced by exposure of PBLs to 6 MV X-ray photons. Matched cultures were set up from untreated and irradiated cells in RPMI 1640 medium, supplemented with 15% fetal bovine serum (FBS, PAN Biotech, Aidenbach, Germany). Lymphocyte growth activation was achieved by phytohemagglutinin (PHA HA16, Thermo Scientific, Dartford, UK). The cell cycle assay was performed using 5-bromo-2′-deoxyuridine (BrdU)–Hoechst 33258 flow cytometry. Cells with replication fork-stalling types of DNA damage become delayed in the G2 phase of the cell cycle.

Phospho-histone H3 analysis

LCLs were washed in PBS, fixed in 2% paraformaldehyde (PFA), and permeabilized with 90% methanol for 30 min on ice. Phospho-histone H3-Ser10 (pH3) was detected with anti-pH3 antibody and corresponding secondary antibody (S6 Table). DAPI at 2 μg/ml final concentration was used as a counterstain for DNA content and cell cycle distribution. Fluorescence was recorded using the same LSRII flow cytometer (Becton Dickinson, Franklin Lakes, NJ, USA) as for cell cycle studies. Data analysis was done with WinMDI 2.9 software (MicroSoft, Redmond, WA, USA).

Cortical precursor cultures

Cortices of *CD1* mouse E13 embryos (Charles River, Sherbrooke, Quebec, Canada; E, embryonic days) were dissected in ice-cold Hank's balanced salt solution (HBSS, Gibco, Carlsbad, CA, USA) and immediately placed in cortical precursor culture media (CPCM), Neurobasal (Gibco) supplemented by 40 ng/ml bFGF (BD Biosciences, San Jose, CA, USA), 2% B27 (Gibco), 1% Penicillin/Streptomycin (Lonza, Basel, Switzerland), and 500 μM L-Glutamine (Gibco). Following mechanical tissue dissociation, cells were plated on Poly-D-Lysine (Sigma, St.Louis, MO, USA) and mouse laminin (Corning, Corning, NY, USA) -coated coverslips (150,000 viable cells per well of a 24-well plate) and allowed to adhere for four hours in CPCM. Subsequently, cells were transfected with the appropriate plasmids overnight using Lipofectamine LTX (Invitrogen, Carlsbad, CA, USA) in Opti-MEM (Gibco). Because, *Lfc* overexpression is known to cause cell death, following transfection, 50 μM of the caspase inhibitor ZVAD-FMK (R&D Systems, Minneapolis, MN, USA) was added to the culture media.[24] Two days later, on DIV3, cells were fixed with 4% PFA and permeabilized with 0.2% NP-40 (USB Corporation, Cleveland, OH, USA) in PBS. Cultures were then stained with antibodies listed in S6 Table. EGFP-positive cells (n = 75–100 per cover slip, prepared in four independent experiments) were evaluated for co-staining with βIII-tubulin or Ki67 using a Zeiss Axiovert A.1 fluorescence microscope.

Plasmids

The nuclear EGFP (*pEF-EGFP*) expression plasmid and the *Arhgef2 (Lfc)* shRNA constructs in *pG-SHIN2* vector were generated as reported previously.[24] Wildtype *ARHGEF2* (NM_001162383.1) and mutant *ARHGEF2* (c.1462delG, position according to NM_004723.3)

were cloned into a *pcDNA3.1(Zeo)(+)* plasmid (Invitrogen). Mutant *ARHGEF2* was generated using the QuikChange II XL Site-Directed Mutagenesis kit (Agilent, 200521) with primers given in S5 Table following the manufacturer's protocol. Sanger sequencing confirmed the correct insertion of the mutation.

In utero electroporation

In utero electroporation was performed as described previously[55] using a CUY21 EDIT electroporator (TR Tech, Japan) to deliver five 50 ms pulses of 40–50 V with 950 ms intervals per embryo. Per embryonic brain, 4 μg total of plasmid DNA was suspended in the tracer 0.5% trypan blue in a ratio of 37.5% *shArhgef2 (Lfc)* (or shCon), 37.5% human *ARHGEF2* (wt)/human *ARHGEF2* (mut)/empty vector, and 25% *pEF-EGFP* plasmid. Embryos were collected 3 days following electroporation. Following an over-night fixation in 4% PFA, brains were cryopreserved and mounted. Coronal cryosections of 18 μm were incubated with antibodies listed in S6 Table. Images were collected from three brain sections per condition using a Quorom spinning disk confocal microscope system or the Zeiss Axio Imager M2 system. EGFP-positive cells were counted in either the combined ventricular zone/sub-ventricular zone/intermediate zone (VZ/SVZ/IZ) or the cortical plate (CP) and reported as proportion of EGFP-positive cells in each of these regions. SatB2/EGFP-double positive cells in the CP were also counted for each condition.

For mitotic spindle plane analysis, the electroporated brain sections were stained with antibodies directed against Cdk5rap2 and corresponding secondary antibodies (S6 Table). Nuclei were labeled with DAPI. Images of transfected cells in 10–15 μm z-stacks at an interval of 0.1 μm thickness were collected using a Zeiss Spinning Disc microscopy system CXU-S1 with ZEN 2012 software. The mitotic spindle plane was evaluated through measurement of the angle between the ventricular surface and a line connecting the centrosomes, using the ImageJ software.

RhoA Pull-down assay

Activated RhoA was assessed using the Rho Activation Assay Biochem kit (Cytoskeleton, Denver, USA) according to the manufacturer's protocol. Experiments were run in triplicate.

Analysis of *Arhgef2* deficient mice

Arhgef2 deficient mice were genotyped as previously reported.[40] P0 and adult brains were dissected and embedded in paraffin/OCT medium as reported previously. [54] Sagittal/coronal brain sections of 10 μm were collected on histologic slides and stained with Hematoxylin and Eosin (H&E) or Gallyas or 3, 3'-Diaminobenzidine (DAB) staining following standard protocols. Whole brain, brain stem, cerebellum, and pontine nuclei volume were evaluated by measuring respective areas in every tenth section using ImageJ and multiplying by the thickness between sections. Immunohistology was performed on brain sections by blocking in staining buffer (0.2% gelatin, 0.25% Triton X-100, 3% BSA) for 30 min for permeabilization, followed by overnight incubation with primary antibodies and an 2 h incubation with the corresponding secondary antibodies (antibodies listed in S6 Table). Nuclei were labeled with 4',6-Diamidino-2-phenylindole (DAPI, 1:1000, Sigma-Aldrich). Images were obtained using a Zeiss Spinning Disc microscopy system CXU-S1 with ZEN 2012 software.

In situ hybridization of *Arhgef2*

A 516 bp *Arhgef2* PCR product was generated with primers listed in S5 Table and subsequently cloned into a p-AL2-T vector. The RNA probe was generated by *in vitro* transcription. Chromogenic/fluorescence *in situ* hybridization was performed on 16 μm thick brain sections from E11/P0 mice post-fixed in 4% PFA for 15 min and permeabilized with Proteinase K for 2.5 min at RT. The reaction was stopped by applying 0.2% glycine in PBS 1x, followed by 20 min post fixation with 20% glutaraldehyde in 4% PFA. The sections were treated with the pre-hybridization buffer (50% formamide, 5x SSC pH 7.0, 2.5 M EDTA, 0.1% Tween-20, 0.15% CHAPS, 0.1 mg/ml Heparin, 100 μg/ml yeast tRNA, 50 μg/ml salmon sperm DNA, 1x Denhardt's solution) at 65˚C for 2 hours followed by overnight incubation with *Arhgef2* RNA probes at 65˚C. Sections were then treated with RNase A for 30 min at 37˚C, subsequently washed with SSC pH 4.5 in 50% formamide at 65˚C and then with KTBT (100 mM NaCl, 50 mM Tris–HCl pH 7.5, 10 mM KCl, 1% Triton X-100) at RT. Following blocking in 20% sheep serum and incubation with sheep anti-DIG antibody (1:1,000, Roche, Mannheim, Germany) at 4˚C overnight, the sections were washed in KTBT and NTMT (50 mM NaCl, 100 mMTris–HCl pH 9.5, 50 mM $MgCl_2$, 0.5% Tween-20) for 1 hour at RT. Development was achieved through addition of the chromogenic NBT/BCIP substrate (1:50, Roche).

Proliferation and cell size assay of WT and *Arhgef2*-/- mice

$CD4^+$ naive T cells were isolated from spleen of *C57BL*/6 (WT) and *Arhgef2*-/- mice by using $CD4^+CD62L^+$ T Cell Isolation Kit (Miltenyi Biotec, San Diego, CA, USA) and subsequently stained with CellTracer Violet Cell Proliferation Kit (Thermo Fisher Scientific) according to the instructions provided. Cells were then incubated with 2 μg/ml of anti-CD28 antibody (BD, New Jersey, USA) in anti-CD3e antibody (BD, New Jersey, USA) pre-coated wells for 4 days at the cell concentration of 1×10^6 cell/ml. 4 days later, cells were collected and stained with APC-conjugated anti-CD3e (Biolegend, San Diego, CA, USA) and BV786-conjugated anti-CD4 (BD, New Jersey, USA). Cells were analyzed by FACS Aria II (BD Bioscience, New Jersey, USA) followed by using FlowJo software (Tree Star). All cells were pre-gated on singlet cells (area & width) and on living cells ($7AAD^-$).

Supporting information

S1 Table. Phenotype of patients with homozygous *ARHGEF2* mutation.
(PDF)

S2 Table. Clinical growth chart from both affected brothers.
(PDF)

S3 Table. Development of affected patients from two months through two years.
(PDF)

S4 Table. Regions of homozygosity (> 1 Mb) between patients II.1 and II.2.
(PDF)

S5 Table. Primer sequences for qPCR, *in situ* hybridization, and site-directed mutagenesis.
(PDF)

S6 Table. List of primary antibodies.
(PDF)

S1 Fig. Full-length Western blot of ARHGEF2. ARHGEF2 can be detected at the expected height of 120 kDa in control LCLs and LCLs of heterozygous parents. Both full length (120

kDa) and the predicted truncated (57 kDa) ARHGEF2 could not be detected in patient LCLs using N-terminus antibody in Western blot analysis. Actin (43 kDa) is used as loading control.
(TIF)

S2 Fig. Normal mitotic transit and minimal sensitivity of P1 (II.1) and P2 (II.2) patient cells towards ionizing radiation. (**A**) Normal proportions of H3P (Ser10)-positive cells (y-axis, boxed) and uni-parametric cell cycle distributions (x-axis) in LCL culture of patients (II.1, II.2), their parents and a normal control. **(B) (i)** Cell cycle allocation in a 72-h lymphocyte culture from patient P2 without prior irradiation. Bivariate BrdU–Hoechst 33258 and PI flow cytometry shows the distribution of cells within up to four cell cycles, I (G0/G1 to G2), II (G1′ to G2′), III (G1″ to G2″), and IV (G1‴). (**ii**) Exposure of lymphocytes to 1.5 Gy irradiation at culture setup results in a more pronounced track of debris from the G0/G1 phase, slight growth reduction and minimal accumulation of cells in G2, similar to what is observed in normal controls. (**iii**) A standard dosage level of 1.5 Gy discriminates normal control (CON, gray circles; n = 75; mean ± 1 SD, 0.09±0.03) from AT lymphocyte cultures (gray diamonds; n = 77; mean ± 1 SD, 0.41 ± 0.13). P1 (black upright triangle; G2 ÷ GF, 0.14) and P2 (black inverted triangle; G2 ÷ GF, 0.10) lymphocytes fall within the range of normal control G2 ÷ GF ratios. Other radiosensitive controls include LIG4 (gray squares; mean ± 1 SD, 0.44 ± 0.09) and NHEJ1 (gray hexagons; mean ± 1 SD, 0.63 ± 0.05) lymphocytes. (**iv**) The G2 ÷ GF rates of 72-hr lymphocyte cultures from P1 (black upright triangle) and P2 (black inverted triangle) resemble the dose–response curve seen in normal controls (CON, gray circles; n = 75; means ± 1 SD) rather than that of AT (gray diamonds; n = 11–77; means ± 1 SD), LIG4 (gray squares; n = 1–2; single values or range) or NHEJ1 (gray hexagons; n = 1–3; single values or means ± 1 SD) radiosensitive controls for a broader range of irradiation (0–8 Gy).
(TIF)

S3 Fig. Normal centrosomal morphology in the index patients. Representative fluorescence micrographs of control and patient (II.1, II.2) LCLs stained for centrosomal γ-tubulin (green) and DAPI (blue), indicating normal centrosomal integrity. Scale bar 10 μm.
(TIF)

S4 Fig. Proliferation rate and T-cell size is not altered in the *Arhgef2*-/- mice. CellTracer Violet stained splenic $CD4^+$ naive T cells were incubated under the anti-CD3e / CD28 antibody stimulation for 4 days. Cells were collected and analyzed by flow cytometer. (**A**) Each generation (G0 to G6) were gated as shown, following gated for $CD3e^+$ and $CD4^+$. (**B**) Bar graph shows proliferation index (PI), using following formula; $PI = (N_{G0} + N_{G1} + N_{G2} + N_{Gn}) / (N_{G0}/2^0 + N_{G1}/2^1 + N_{G2}/2^2 + N_{Gn}/2^n)$, n = 6, Error bars indicate mean ± S.E.M, ns = not significant. (**C**) Histograms show FSC and SSC of total $CD3e^+$ $CD4^+$ T cells (upper) or 4th generation (G4) in $CD3e^+$ $CD4^+$ T cells (lower).
(TIF)

S5 Fig. Expression of *Arhgef2* in E11 and P0 mouse brain. (A) *Arhgef2* is strongly expressed in the neuroepithelium of the brain at E11. **(B)** At P0, *Arhgef2* is expressed predominantly in the VZ/SVZ and upper layer of the neocortex, in the external granule layer (EGL) of the cerebellum and in the pontine nuclei (DIC images of *in situ* hybridization with anti-sense and sense *Arhgef2* RNA probes, n = 4, scale bar 1 mm (A), scale bar 100 μm (B)).
(TIF)

S6 Fig. *Arhgef2*-/- mice shows normal distribution of neurons in the cortical layers. (A) Representative fluorescence micrographs of WT and *Arhgef2*-/- mice cortex stained for layers II-IV (Cux1, green), layers V-VI (Ctip2, red) and DAPI. **(B)**. Quantification of cortical volume,

surface area, thickness, total number of DAPI cells, Cux1 and Ctip2 positive cells per view field revealed no significant difference between control and mutant mice. (n = 3–4, Student's *t-test*, ns- not significant, error bars represent ± SD, scale bar 100 μm).
(TIF)

S7 Fig. *Arhgef2*-/- mice shows no abnormalities in the midbrain structures. Representative DAB (3, 3'-Diaminobenzidine) stained micrographs of WT and *Arhgef2*-/- mice showing normal structures of FoxP2-positive inferior colliculus and superior colliculus. Scale bar 200 μm.
(TIF)

S8 Fig. Normal Purkinje cell size and molecular layer thickness in the *Arhgef2*-/- mice. (A) Representative H&E stained micrographs of WT and mutant cerebellum (scale bar 500 μm), and **(B)** magnified cerebellar folia. **(C)** No significant change in Purkinje cell size and thickness of the molecular layer was observed in the mutant mice upon quantification. (n = 3–4, Student's *t-test*, ns- not significant, error bars represent ± SD, scale bar 20 μm).
(TIF)

S9 Fig. Co-expression of *Arhgef2* and Mbh2 in the mantle zone of developing hindbrain. Photomicrographs representing transverse E11 section of dorsal hindbrain stained for *Arhgef2* (green), Mbh2 (red), Olig3 (cyan), and DAPI, indicates a clear colocalisation in the mantle zone along migratory pathway. Scale bar 100 μm.
(TIF)

Acknowledgments

The authors thank the family members who participated in this study. We acknowledge K. Handschug, J. Fassbender, S. Buchert, B. Spors, N. DiDonato, G. Neri, R. Friedl, G. Stoltenburg-Didinger, Paraskevi Bessa, I. Bormuth, M. Rosário, R. Wunderlich, Guadalupe Camarero, V. Tarabykin, S. Burns, T. Omatsu and Y. Zhao for their contribution of clinical data, technical help and discussions. We thank specially P. Shah and S. Srivatsa for helping in providing the *Arhgef2* mutant brain samples. We further thank E.M. Valente for sending DNA samples and clinical data of patients with similar phenotypes.

Author Contributions

Conceptualization: AMK ER CB LRHM FDM.

Data curation: HH.

Formal analysis: ER SAY HH.

Funding acquisition: AMK HCR HHR FDM CB TFW.

Investigation: ER SAY LRHM NK ON EB CB FDM HH LM DS HCR.

Methodology: CH AMK AH.

Resources: HCR CH AH.

Supervision: AMK EB HCR HHR FDM CB TFW.

Visualization: ER SAY LRHM.

Writing – original draft: AMK ER LRHM.

Writing – review & editing: HH SAY NK ON LM EB DS AH HCR CB HHR FDM TFW CH.

References

1. Thompson CL, Ng L, Menon V, Martinez S, Lee CK, Glattfelder K, et al. A high-resolution spatiotemporal atlas of gene expression of the developing mouse brain. Neuron. 2014; 83(2):309–23. https://doi.org/10.1016/j.neuron.2014.05.033 PMID: 24952961
2. Kang HJ, Kawasawa YI, Cheng F, Zhu Y, Xu X, Li M, et al. Spatio-temporal transcriptome of the human brain. Nature. 2011; 478(7370):483–9. https://doi.org/10.1038/nature10523 PMID: 22031440
3. Miller JA, Ding SL, Sunkin SM, Smith KA, Ng L, Szafer A, et al. Transcriptional landscape of the prenatal human brain. Nature. 2014; 508(7495):199–206. https://doi.org/10.1038/nature13185 PMID: 24695229
4. Hu WF, Chahrour MH, Walsh CA. The diverse genetic landscape of neurodevelopmental disorders. Annu Rev Genomics Hum Genet. 2014; 15:195–213. https://doi.org/10.1146/annurev-genom-090413-025600 PMID: 25184530
5. Ernst C. Proliferation and Differentiation Deficits are a Major Convergence Point for Neurodevelopmental Disorders. Trends Neurosci. 2016; 39(5):290–9. https://doi.org/10.1016/j.tins.2016.03.001 PMID: 27032601
6. Nasrallah IM, Golden JA. Brain malformations associated with cell migration. Pediatr Dev Pathol. 2006; 9(2):89–97. https://doi.org/10.2350/06-04-0077.1 PMID: 16808640
7. Marin O, Rubenstein JL. A long, remarkable journey: tangential migration in the telencephalon. Nat Rev Neurosci. 2001; 2(11):780–90. https://doi.org/10.1038/35097509 PMID: 11715055
8. Bloch-Gallego E, Causeret F, Ezan F, Backer S, Hidalgo-Sanchez M. Development of precerebellar nuclei: instructive factors and intracellular mediators in neuronal migration, survival and axon pathfinding. Brain Res Brain Res Rev. 2005; 49(2):253–66. https://doi.org/10.1016/j.brainresrev.2005.01.003 PMID: 16111554
9. Evsyukova I, Plestant C, Anton ES. Integrative mechanisms of oriented neuronal migration in the developing brain. Annu Rev Cell Dev Biol. 2013; 29:299–353. https://doi.org/10.1146/annurev-cellbio-101512-122400 PMID: 23937349
10. Birkenfeld J, Nalbant P, Yoon SH, Bokoch GM. Cellular functions of GEF-H1, a microtubule-regulated Rho-GEF: is altered GEF-H1 activity a crucial determinant of disease pathogenesis? Trends Cell Biol. 2008; 18(5):210–9. https://doi.org/10.1016/j.tcb.2008.02.006 PMID: 18394899
11. Bakal CJ, Finan D, LaRose J, Wells CD, Gish G, Kulkarni S, et al. The Rho GTP exchange factor Lfc promotes spindle assembly in early mitosis. Proc Natl Acad Sci U S A. 2005; 102(27):9529–34. https://doi.org/10.1073/pnas.0504190102 PMID: 15976019
12. Chang YC, Lee HH, Chen YJ, Bokoch GM, Chang ZF. Contribution of guanine exchange factor H1 in phorbol ester-induced apoptosis. Cell Death Differ. 2006; 13(12):2023–32. Epub 2006/04/08. https://doi.org/10.1038/sj.cdd.4401901 PMID: 16601754
13. Ren Y, Li R, Zheng Y, Busch H. Cloning and characterization of GEF-H1, a microtubule-associated guanine nucleotide exchange factor for Rac and Rho GTPases. J Biol Chem. 1998; 273(52):34954–60. PMID: 9857026
14. Krendel M, Zenke FT, Bokoch GM. Nucleotide exchange factor GEF-H1 mediates cross-talk between microtubules and the actin cytoskeleton. Nat Cell Biol. 2002; 4(4):294–301. https://doi.org/10.1038/ncb773 PMID: 11912491
15. Tonami K, Kurihara Y, Arima S, Nishiyama K, Uchijima Y, Asano T, et al. Calpain-6, a microtubule-stabilizing protein, regulates Rac1 activity and cell motility through interaction with GEF-H1. Journal of cell science. 2011; 124(Pt 8):1214–23. Epub 2011/03/17. https://doi.org/10.1242/jcs.072561 PMID: 21406564
16. Meiri D, Marshall CB, Greeve MA, Kim B, Balan M, Suarez F, et al. Mechanistic insight into the microtubule and actin cytoskeleton coupling through dynein-dependent RhoGEF inhibition. Mol Cell. 2012; 45(5):642–55. Epub 2012/03/13. https://doi.org/10.1016/j.molcel.2012.01.027 PMID: 22405273
17. Yoshimura Y, Miki H. Dynamic regulation of GEF-H1 localization at microtubules by Par1b/MARK2. Biochem Biophys Res Commun. 2011; 408(2):322–8. Epub 2011/04/26. https://doi.org/10.1016/j.bbrc.2011.04.032 PMID: 21513698
18. Callow MG, Zozulya S, Gishizky ML, Jallal B, Smeal T. PAK4 mediates morphological changes through the regulation of GEF-H1. Journal of cell science. 2005; 118(Pt 9):1861–72. Epub 2005/04/14. https://doi.org/10.1242/jcs.02313 PMID: 15827085
19. Zenke FT, Krendel M, DerMardirossian C, King CC, Bohl BP, Bokoch GM. p21-activated kinase 1 phosphorylates and regulates 14-3-3 binding to GEF-H1, a microtubule-localized Rho exchange factor. The Journal of biological chemistry. 2004; 279(18):18392–400. Epub 2004/02/19. https://doi.org/10.1074/jbc.M400084200 PMID: 14970201
20. Meiri D, Greeve MA, Brunet A, Finan D, Wells CD, LaRose J, et al. Modulation of Rho guanine exchange factor Lfc activity by protein kinase A-mediated phosphorylation. Molecular and cellular biology. 2009; 29(21):5963–73. Epub 2009/08/12. https://doi.org/10.1128/MCB.01268-08 PMID: 19667072

21. Fujishiro SH, Tanimura S, Mure S, Kashimoto Y, Watanabe K, Kohno M. ERK1/2 phosphorylate GEF-H1 to enhance its guanine nucleotide exchange activity toward RhoA. Biochem Biophys Res Commun. 2008; 368(1):162–7. Epub 2008/01/24. https://doi.org/10.1016/j.bbrc.2008.01.066 PMID: 18211802

22. Birkenfeld J, Nalbant P, Bohl BP, Pertz O, Hahn KM, Bokoch GM. GEF-H1 modulates localized RhoA activation during cytokinesis under the control of mitotic kinases. Dev Cell. 2007; 12(5):699–712. Epub 2007/05/10. https://doi.org/10.1016/j.devcel.2007.03.014 PMID: 17488622

23. Mizuarai S, Yamanaka K, Kotani H. Mutant p53 induces the GEF-H1 oncogene, a guanine nucleotide exchange factor-H1 for RhoA, resulting in accelerated cell proliferation in tumor cells. Cancer Res. 2006; 66(12):6319–26. https://doi.org/10.1158/0008-5472.CAN-05-4629 PMID: 16778209

24. Gauthier-Fisher A, Lin DC, Greeve M, Kaplan DR, Rottapel R, Miller FD. Lfc and Tctex-1 regulate the genesis of neurons from cortical precursor cells. Nat Neurosci. 2009; 12(6):735–44. https://doi.org/10.1038/nn.2339 PMID: 19448628

25. Morgan R, Hooiveld MH, Durston AJ. A novel guanine exchange factor increases the competence of early ectoderm to respond to neural induction. Mechanisms of development. 1999; 88(1):67–72. Epub 1999/10/19. PMID: 10525189

26. Streit A, Stern CD. Neural induction. A bird's eye view. Trends Genet. 1999; 15(1):20–4. Epub 1999/03/24. PMID: 10087929

27. Itoh K, Ossipova O, Sokol SY. GEF-H1 functions in apical constriction and cell intercalations and is essential for vertebrate neural tube closure. J Cell Sci. 2014; 127(Pt 11):2542–53. https://doi.org/10.1242/jcs.146811 PMID: 24681784

28. Nalbant P, Chang YC, Birkenfeld J, Chang ZF, Bokoch GM. Guanine nucleotide exchange factor-H1 regulates cell migration via localized activation of RhoA at the leading edge. Molecular biology of the cell. 2009; 20(18):4070–82. Epub 2009/07/25. https://doi.org/10.1091/mbc.E09-01-0041 PMID: 19625450

29. Tsuji T, Ohta Y, Kanno Y, Hirose K, Ohashi K, Mizuno K. Involvement of p114-RhoGEF and Lfc in Wnt-3a- and dishevelled-induced RhoA activation and neurite retraction in N1E-115 mouse neuroblastoma cells. Molecular biology of the cell. 2010; 21(20):3590–600. Epub 2010/09/03. https://doi.org/10.1091/mbc.E10-02-0095 PMID: 20810787

30. Kutsche K, Yntema H, Brandt A, Jantke I, Nothwang HG, Orth U, et al. Mutations in ARHGEF6, encoding a guanine nucleotide exchange factor for Rho GTPases, in patients with X-linked mental retardation. Nat Genet. 2000; 26(2):247–50. https://doi.org/10.1038/80002 PMID: 11017088

31. Harvey K, Duguid IC, Alldred MJ, Beatty SE, Ward H, Keep NH, et al. The GDP-GTP exchange factor collybistin: an essential determinant of neuronal gephyrin clustering. J Neurosci. 2004; 24(25):5816–26. Epub 2004/06/25. https://doi.org/10.1523/JNEUROSCI.1184-04.2004 PMID: 15215304

32. Verhoeven K, De Jonghe P, Coen K, Verpoorten N, Auer-Grumbach M, Kwon JM, et al. Mutations in the small GTP-ase late endosomal protein RAB7 cause Charcot-Marie-Tooth type 2B neuropathy. Am J Hum Genet. 2003; 72(3):722–7. Epub 2003/01/25. https://doi.org/10.1086/367847 PMID: 12545426

33. Barnabe-Heider F, Wasylnka JA, Fernandes KJ, Porsche C, Sendtner M, Kaplan DR, et al. Evidence that embryonic neurons regulate the onset of cortical gliogenesis via cardiotrophin-1. Neuron. 2005; 48(2):253–65. https://doi.org/10.1016/j.neuron.2005.08.037 PMID: 16242406

34. Menard C, Hein P, Paquin A, Savelson A, Yang XM, Lederfein D, et al. An essential role for a MEK-C/EBP pathway during growth factor-regulated cortical neurogenesis. Neuron. 2002; 36(4):597–610. PMID: 12441050

35. Zhong W, Chia W. Neurogenesis and asymmetric cell division. Curr Opin Neurobiol. 2008; 18(1):4–11. https://doi.org/10.1016/j.conb.2008.05.002 PMID: 18513950

36. Chang YC, Nalbant P, Birkenfeld J, Chang ZF, Bokoch GM. GEF-H1 couples nocodazole-induced microtubule disassembly to cell contractility via RhoA. Molecular biology of the cell. 2008; 19(5):2147–53. https://doi.org/10.1091/mbc.E07-12-1269 PMID: 18287519

37. Artamonov MV, Jin L, Franke AS, Momotani K, Ho R, Dong XR, et al. Signaling pathways that control rho kinase activity maintain the embryonic epicardial progenitor state. The Journal of biological chemistry. 2015; 290(16):10353–67. https://doi.org/10.1074/jbc.M114.613190 PMID: 25733666

38. Katayama K, Melendez J, Baumann JM, Leslie JR, Chauhan BK, Nemkul N, et al. Loss of RhoA in neural progenitor cells causes the disruption of adherens junctions and hyperproliferation. Proceedings of the National Academy of Sciences of the United States of America. 2011; 108(18):7607–12. https://doi.org/10.1073/pnas.1101347108 PMID: 21502507

39. Roszko I, Afonso C, Henrique D, Mathis L. Key role played by RhoA in the balance between planar and apico-basal cell divisions in the chick neuroepithelium. Developmental biology. 2006; 298(1):212–24. https://doi.org/10.1016/j.ydbio.2006.06.031 PMID: 16860308

40. Chiang HS, Zhao Y, Song JH, Liu S, Wang N, Terhorst C, et al. GEF-H1 controls microtubule-dependent sensing of nucleic acids for antiviral host defenses. Nat Immunol. 2014; 15(1):63–71. https://doi.org/10.1038/ni.2766 PMID: 24270516

41. Altman J, Bayer SA. Development of the precerebellar nuclei in the rat: IV. The anterior precerebellar extramural migratory stream and the nucleus reticularis tegmenti pontis and the basal pontine gray. J Comp Neurol. 1987; 257(4):529–52. https://doi.org/10.1002/cne.902570405 PMID: 3693597

42. Altman J, Bayer SA. Development of the precerebellar nuclei in the rat: III. The posterior precerebellar extramural migratory stream and the lateral reticular and external cuneate nuclei. J Comp Neurol. 1987; 257(4):513–28. https://doi.org/10.1002/cne.902570404 PMID: 3693596

43. Altman J, Bayer SA. Development of the precerebellar nuclei in the rat: II. The intramural olivary migratory stream and the neurogenetic organization of the inferior olive. J Comp Neurol. 1987; 257(4):490–512. https://doi.org/10.1002/cne.902570403 PMID: 3693595

44. Altman J, Bayer SA. Development of the precerebellar nuclei in the rat: I. The precerebellar neuroepithelium of the rhombencephalon. J Comp Neurol. 1987; 257(4):477–89. https://doi.org/10.1002/cne.902570402 PMID: 3693594

45. Hernandez-Miranda LR, Muller T, Birchmeier C. The dorsal spinal cord and hindbrain: From developmental mechanisms to functional circuits. Developmental biology. 2016.

46. Landsberg RL, Awatramani RB, Hunter NL, Farago AF, DiPietrantonio HJ, Rodriguez CI, et al. Hindbrain rhombic lip is comprised of discrete progenitor cell populations allocated by Pax6. Neuron. 2005; 48(6):933–47. https://doi.org/10.1016/j.neuron.2005.11.031 PMID: 16364898

47. Wang VY, Rose MF, Zoghbi HY. Math1 expression redefines the rhombic lip derivatives and reveals novel lineages within the brainstem and cerebellum. Neuron. 2005; 48(1):31–43. https://doi.org/10.1016/j.neuron.2005.08.024 PMID: 16202707

48. Causeret F, Hidalgo-Sanchez M, Fort P, Backer S, Popoff MR, Gauthier-Rouviere C, et al. Distinct roles of Rac1/Cdc42 and Rho/Rock for axon outgrowth and nucleokinesis of precerebellar neurons toward netrin 1. Development. 2004; 131(12):2841–52. https://doi.org/10.1242/dev.01162 PMID: 15151987

49. McMahon AP, Joyner AL, Bradley A, McMahon JA. The midbrain-hindbrain phenotype of Wnt-1-/Wnt-1- mice results from stepwise deletion of engrailed-expressing cells by 9.5 days postcoitum. Cell. 1992; 69(4):581–95. PMID: 1534034

50. Aldinger KA, Mendelsohn NJ, Chung BH, Zhang W, Cohn DH, Fernandez B, et al. Variable brain phenotype primarily affects the brainstem and cerebellum in patients with osteogenesis imperfecta caused by recessive WNT1 mutations. J Med Genet. 2016; 53(6):427–30. https://doi.org/10.1136/jmedgenet-2015-103476 PMID: 26671912

51. Najmabadi H, Hu H, Garshasbi M, Zemojtel T, Abedini SS, Chen W, et al. Deep sequencing reveals 50 novel genes for recessive cognitive disorders. Nature. 2011; 478(7367):57–63. Epub 2011/09/23. https://doi.org/10.1038/nature10423 PMID: 21937992

52. Neitzel H. A routine method for the establishment of permanent growing lymphoblastoid cell lines. Hum Genet. 1986; 73(4):320–6. Epub 1986/08/01. PMID: 3017841

53. Kraemer N, Neubert G, Issa L, Ninnemann O, Seiler AE, Kaindl AM. Reference genes in the developing murine brain and in differentiating embryonic stem cells. Neurol Res. 2012; 34(7):664–8. Epub 2012/06/28. https://doi.org/10.1179/1743132812Y.0000000060 PMID: 22735032

54. Issa L, Kraemer N, Rickert CH, Sifringer M, Ninnemann O, Stoltenburg-Didinger G, et al. CDK5RAP2 expression during murine and human brain development correlates with pathology in primary autosomal recessive microcephaly. Cereb Cortex. 2013; 23(9):2245–60. https://doi.org/10.1093/cercor/bhs212 PMID: 22806269

55. Gauthier AS, Furstoss O, Araki T, Chan R, Neel BG, Kaplan DR, et al. Control of CNS cell-fate decisions by SHP-2 and its dysregulation in Noonan syndrome. Neuron. 2007; 54(2):245–62. https://doi.org/10.1016/j.neuron.2007.03.027 PMID: 17442246

Mein Lebenslauf wird aus datenschutzrechtlichen Gründen in der elektronischen Version meiner Arbeit nicht veröffentlicht.

My curriculum vitae is not published for privacy reasons in the electronic version of my thesis.

9 Complete list of publications

1. Varsha Jain, **Ethiraj Ravindran**, Narender K. Dhingra. Differential Expression of Brn3 Transcription Factors in Intrinsically-Photosensitive Retinal Ganglion Cells. Journal of Comparative Neurology 2012; 520: 742–755. (Impact factor = 3.331)
2. Heba Gamal Farag, Sebastian Froehler, Konrad Oexle, **Ethiraj Ravindran**, Detlev Schindler, Timo Staab, Angela Huebner, Nadine Kraemer, Wei Chen, Angela M Kaindl. Abnormal centrosome and spindle morphology in a patient with autosomal recessive primary microcephaly type 2 due to compound heterozygous WDR62 gene mutation. Orphanet Journal of Rare Diseases 2013; 8: 178. (Impact factor = 3.290)
3. Horst von Bernuth, **Ethiraj Ravindran**, Hang Du, Sebastian Fröhler, Karoline Strehl, Nadine Krämer, Lina Issa-Jahns, Borko Amulic, Olaf Ninnemann, Mei-Sheng Xiao, Katharina Eirich, Uwe Kölsch, Kathrin Hauptmann, Rainer John, Detlev Schindler, Volker Wahn, Wei Chen, Angela M. Kaindl. Combined immunodeficiency develops with age in Immunodeficiency centromeric instability-facial anomalies syndrome 2 (ICF2). Orphanet Journal of Rare Diseases 2014; 9:116. (Impact factor = 3.290)
4. Nadine Kraemer, **Ethiraj Ravindran**, Sami Zaqout, Gerda Neubert, Detlev Schindler, Olaf Ninnemann, Ralph Gräf, Andrea EM Seiler & Angela M Kaindl. Loss of CDK5RAP2 affects neural but not non-neural mESC differentiation into cardiomyocytes. Cell Cycle 2015; 14:2044-57. (Impact factor = 3.952)
5. Nadine Kraemer, Lina Issa-Jahns, Gerda Neubert, **Ethiraj Ravindran**, Shyamala Mani, Olaf Ninnemann, Angela M. Kaindl. Novel Alternative Splice Variants of Mouse Cdk5rap2. PlosOne 2015; 10.1371. (Impact factor = 4.411)
6. **Ethiraj Ravindran**, Hao Hu, Scott A. Yuzwa, Luis R. Hernandez-Miranda, Nadine Kraemer, Olaf Ninnemann, Luciana Musante, Eugen Boltshauser, Detlev Schindler, Angela Hübner, Hans-Christian Reinecker, Hans-Hilger Ropers, Carmen Birchmeier, Freda D. Miller, Thomas F. Wienker, Christoph Hübner, Angela M. Kaindl. Homozygous *ARHGEF2* mutation causes intellectual disability and

midbrain-hindbrain malformation. PLos Genetics 2017; 10.1371. (Impact factor = 6.661)

Conference presentation

1. **Ethiraj Ravindran**, Karoline Strehl, Nadine Krämer, Lina Issa-Jahns, Sebastian Fröhler, Katharina Eirich, Detlev Schindler, Wei Chen, Horst von Bernuth, Angela M. Kaindl. Immunodeficiency centromeric instability-facial anomalies syndrome 2 (ICF2): Extending the phenotype caused by homozygous *ZBZB24* gene mutation. 10th Göttingen meeting of the German Neuroscience Society, Göttingen, Germany, 13-16 March, 2013 (poster).
2. **Ethiraj Ravindran**, Horst von Bernuth, Hang Du, Sebastian Fröhler, Karoline Strehl, Nadine Krämer, Lina Issa-Jahns, Borko Amulic, Detlev Schindler, Wei Chen, Angela M. Kaindl. Immunodeficiency centromeric instability-facial anomalies syndrome 2 (ICF2): Reduced cell viability and survival caused by homozygous *ZBZB24* gene mutation. Berlin Brain Days, Berlin, Germany, 20-22 November, 2013 (poster).
3. **Ethiraj Ravindran**. Immunodeficiency, centromeric instability, facial anomalies syndrome type 2 (ICF2): combined immunodeficiency, autoimmune phenomena, and intellectual disability. Neurowoche, München, Germany, 15-19 September, 2014 (talk).
4. **Ethiraj Ravindran**, Hao Hu, Nadine Kraemer, Olaf Ninnemann, Luciana Musante, Eugen Boltshauser, Detlev Schindler, Hans-Hilger Ropers, Thomas Wienker, Christoph Hubner, Angela M. Kaindl. A novel phenotype - microcephaly, intellectual disability and mid-hindbrain defect**.** Neurowoche, München, Germany, 15-19 September, 2014 (poster).
5. **Ethiraj Ravindran**, Hao Hu, Scott A. Yuzwa, Nadine Kraemer, Olaf Ninnemann, Luciana Musante, Eugen Boltshauser, Detlev Schindler, Hans-Hilger Ropers, Freda D. Miller, Thomas F. Wienker, Christoph Hübner, Angela M. Kaindl. Novel midbrain-hindbrain malformation, microcephaly, and intellectual disability caused by homozygous mutation in *ARHGEF2*. SFB665: Developmental Disturbances in the Nervous System, 18-20 September, 2014 (poster).

6. **Ethiraj Ravindran**, Hao Hu, Scott A. Yuzwa, Nadine Kraemer, Olaf Ninnemann, Luciana Musante, Eugen Boltshauser, Detlev Schindler, Hans-Hilger Ropers, Freda D. Miller, Thomas F. Wienker, Christoph Hübner, Angela M. Kaindl. Novel mid-hindbrain malformation, microcephaly, and intellectual disability. 11th Göttingen meeting of the German Neuroscience Society, Göttingen, Germany, 18-21 March, 2015 (poster).

7. **Ethiraj Ravindran**, Hao Hu, Scott A. Yuzwa, Nadine Kraemer, Olaf Ninnemann, Luciana Musante, Eugen Boltshauser, Detlev Schindler, Angela Hübner, Hans-Christian Reinecker, Hans-Hilger Ropers, Freda D. Miller, Thomas F. Wienker, Christoph Hübner, Angela M. Kaindl. Novel mid-hindbrain malformation associated with Microcephaly and intellectual disability caused by homozygous *ARHGEF2* gene mutation. EMBO: Nuclear Function and Cell Fate Choice, Kyllini, Greece, 18-22 September, 2016 (poster).

8. **Ethiraj Ravindran**, Hao Hu, Scott A. Yuzwa, Luis R. Hernandez-Miranda, Nadine Kraemer, Olaf Ninnemann, Luciana Musante, Eugen Boltshauser, Detlev Schindler, Angela Hübner, Hans-Christian Reinecker, Hans-Hilger Ropers, Carmen Birchmeier, Freda D. Miller, Thomas F. Wienker, Christoph Hübner, Angela M. Kaindl. Homozygous *ARHGEF2* gene mutation causes intellectual disability and midbrain-hindbrain malformation. 12th Göttingen meeting of the German Neuroscience Society, Göttingen, Germany, 12-25 March, 2017 (poster).

10 Acknowledgements

First and foremost, I whole-heartedly thank my supervisor Professor Dr. Angela M. Kaindl, for giving me a great opportunity to do PhD in the lab at Institute of Cell Biology and Neurobiology, Charitè - Universitätsmedizin, Berlin. I remember those early days in lab where I was extremely unorganized and chaotic at work, but its Angela's trust, support, and guidance, changed me to a better organized person and perform better in the assigned interesting projects in the lab. I thank Angela for always being considerate and concerned about her students and giving us the freedom to work in the lab. Thank you very much Angela for your immense support, care, and guidance.

I would like to take this opportunity to thank my lab members for their support all the time, both professionally and personally. I thank Lina, Nadine, and Bianca for introducing me to the lab and helping me in settling down. I thank Sami for making the work place more fun-filled and memorable. My special thanks to Sylvie and Kathrin, for bringing a wonderful change to the lab environment more friendly with nice scientific discussions and chats, which I cherish a lot. I also thank Jessica and Susanne for their technical help. Thankful to my lab members/friends, who made my time inside- and outside-lab, more enjoyable and being always a well-wisher.

I also would like to thank members at the Institute of Cell Biology and Neurobiology, who helped me during the course of my PhD at various circumstances. I thank Jutta for her help with microscopy and Marni for administrative help. I thank Olaf, Ingo, Gisela, and Marta for their interests and suggestions related to the projects.

I am grateful to German Academic Exchange Service (DAAD), for providing me the financial support during my PhD. I specially thank DAAD for offering German language course, without which I would have not explored Germany much better.

Many thanks to my friends who made my life more interesting and stood beside me at most of the times. My special thanks to Andrew, Eva, Slim, Paul, Magda, Diana, Pina, Sayali for everything. I also thank my few other best friends who mean a lot to me forever.

My heartfelt thanks to my parents for their unconditional love, care, concern, and always being my great support, thinking about my well-being, and that has always made me feel so blessed. Many thanks to my sisters for their love, care and support at all times in

my life. I thank my little nephew, who always surprises us with his growth, intellectual conversation, smart replies, and the limitless love we have for him. I also thank my relatives for their selfless care.

Last but not least, I thank Almighty God for His blessings.